KU LEUVEN

ARENBERG DOCTORAL SCHOOL
Faculty of Engineering Science

Optimal control of energy extraction in large-eddy simulation of wind farms

Jay Prakash Goit

Supervisor:
Prof. dr. ir. Johan Meyers

Dissertation presented in partial fulfillment of the requirements for the degree of Doctor in Engineering

March 2015

Optimal control of energy extraction in large-eddy simulation of wind farms

Jay Prakash GOIT

Examination committee:
Prof. dr. Adhemar Bultheel, chair
Prof. dr. ir. Johan Meyers, supervisor
Prof. dr. Nicole Van Lipzig
Prof. dr. ir. Moritz Diehl
Prof. dr. Jeroen van Beeck
(von Karman Institute for Fluid Dynamics)
Prof. dr. ir. Fernando Porté-Agel
(EPFL, Switzerland)
Prof. dr. ir. Jan-Willem van Wingerden
(TU Delft, The Netherlands)

Dissertation presented in partial fulfillment of the requirements for the degree of Doctor in Engineering

March 2015

Preface

First and foremost, I would like to express my deepest gratitude to my supervisor, Prof. Johan Meyers, for giving me the opportunity to work on this PhD project. I am grateful to him for his continuous support and guidance throughout the PhD program, the time he devoted to our countless discussions and painstaking effort he put into correcting our papers, abstracts, as well as this dissertation. I do not think that I would have accomplished the degree of success that I have achieved without his creative research ideas and insightful analysis of the complex problem of turbulent boundary-layer control. I also learned a lot from Prof. Meyers regarding skills in scientific writing presenting results.

I would like to thank all the members of my examination committee for their thorough reading and evaluation of the dissertation, and for the many useful comments and suggestions they provided.

I enjoyed the working environment in the Mechanical Engineering Department and I am grateful to all the former and current colleagues at the TME for their friendship and support. I would like to express special thanks to the former TFSO members, Sara Delport, Vladimir Jovanovich, Shi-jie Cao, Asim Önder and Hassan Badreddine for their advice and direct contribution to my PhD research. The reading club of 'Turbulent Flows' organized by Asim, Peng and Shi-jie was extremely beneficial during the later half of my PhD. I am equally grateful to my current TFSO colleagues for their encouragement and assistance. Special thanks to Wim for translating the abstract of this dissertation into Dutch. I was fortunate to have two very nice officemates, Jan Timmermans and Ali Emre Yilmaz. I must acknowledge my colleagues and friends, including Stefan Antonov, Geert Buckinx, Ruben Gielen, Joris Gillis, Shivanand Wasan (including Bhabhi-ji and Ganesh), Max Bögli and Amar Behera for their help on multiple occasions during my stay at the department. I really enjoyed hanging out with Peng Zhong and Dejian Wu, and walking back home almost every day with Ercan Atam. I would like to thank Kathleen Coenen, Frieda

Decoster, Valérie Karlshausen and Regine Vanswijgenhoven for their assistance with many administrative matters and Jan Thielemans and Ronny Moreas for their computer-related support. I am truly grateful to Geert Jan Bex, Martijn Oldenhof, Jan Ooghe and Ingrid B. Roig from the HPC team for their regular support with the supercomputing facility. They were always quick to respond to my problems.

My life in Belgium would not have been equally delightful had it not been for the company of a small circle of Nepalese friends that I made in this country. I am thankful to Prabesh Luitel, Gokarna Pandey, Niraj Shrestha and Sapana Shrestha for all the good times we had together. Equally important are my long-time friends back home: Suraj, Ajay and Pramodh, with whom I share everything and who were always there when I needed them.

I would like to take this opportunity to thank my former supervisor, Prof. Yu Fukunishi, for introducing me to this interesting field of fluid mechanics and sparking my interest in boundary layer transition and turbulent flow. I also extend my sincere thanks to Prof. Seiichiro Izawa, Prof. Masaya Shigeta and former colleagues and seniors from the Fluid Mechanics Laboratory at Tohoku University, from whom I learned many things about the science of Flow Dynamics as well as several experimental and computational techniques.

I would like to express my special appreciation to my parents, my brother Om and sisters Punita and Anita. Their unconditional love, support and encouragement have been a primary source of strength for me. I am also grateful to my parents-in-law for strengthening my morale with their continuous encouragement.

Finally, I would like to thank my wife Midori for her love and care over the years. She decided to join me in Belgium right after completing her Master's degree, instead of pursuing her own professional career. I am deeply indebted to her for her sacrifice and patience. I am also thankful to her for painstakingly reading every chapter of this dissertation, and correcting many grammar mistakes and typos. She was always there to celebrate all my successes and support me through difficult times.

Jay Prakash Goit
Leuven, March 2015

Abstract

In large wind farms, the vertical interaction of the farm with the atmospheric boundary layer plays an important role, i.e. the total energy extraction is governed by the vertical transport of kinetic energy from higher regions in the boundary layer towards the turbine level. The current dissertation investigates the use of optimal control techniques in large-eddy simulations of wind-farm boundary-layer interaction with the aim of increasing the total energy extraction in wind farms. The individual wind turbines are considered as flow actuators and their energy extraction is dynamically regulated in time so as to optimally influence the flow field and the vertical turbulent energy transport. The turbines are modelled using the actuator disk model, with disk-based thrust coefficients that are controlled as a function of time and per wind turbine. Such dynamic control of the thrust coefficient represents the effect of the possible blade pitch and generator torque-based control employed in an actual wind turbine.

In the first phase of this dissertation, the wind-farm-ABL interaction in the absence of coordinated control of the turbines is investigated. The response of the wind-farm boundary layer is simulated for different disk-based thrust coefficient values, where thrust coefficient is kept constant in time and the same for all turbines in a simulation. In order to define a correct reference for the dynamic optimal control, the total wind-farm power output from these simulations is normalized by three different references, based on the friction velocity, geostrophic wind and the driving power of the pressure-driven boundary layer. For the wind-farm layout considered in this dissertation, the optimal thrust coefficient value is different from the value for the optimal operating condition of a lone-standing turbine. However, even at the optimal point, only 40% of the total power input is extracted by the wind farm, while 60% is lost to turbulent dissipation.

The second phase of the dissertation focuses on the development of a framework for a gradient- and adjoint-based scheme for wind-farm power optimization.

A receding-horizon approach is employed in which the optimization problem is divided into a number of control windows, and the thrust coefficients are optimized over each window. The non-linear Polak-Ribière conjugate-gradient method and the Brent line search algorithm are chosen for the solution of the optimization problem. The gradient of the cost functional required by the conjugate-gradient method is determined using a continuous adjoint-based approach. The adjoint equations for the standard Navier-Stokes equations are extended to include the adjoints for the subgrid-scale model and wall-stress model, and the adjoint of the actuator disk model.

In the third phase of the dissertation, the optimal control of an infinite wind farm is investigated. The first control case focuses on the direct maximization of the energy extraction. It is found that the energy extraction increases by 16 % compared to the uncontrolled reference. This is directly related to an increase in the vertical fluxes of energy towards the wind turbines, and vertical shear stresses increase considerably. A further analysis, decomposing the total stresses into dispersive and Reynolds stresses, shows that the dispersive stresses increase drastically, and that the Reynolds stresses decrease on average, but increase in the wake region, leading to better wake recovery. It is further observed that turbulent dissipation levels in the boundary layer increase, and overall, the outer layer of the boundary layer enters into a transient decelerating regime, while the inner layer and the turbine region attain a new statistically steady equilibrium within approximately one wind-farm through-flow time. Two additional optimal control cases study the penalization of turbulent dissipation. For the current wind-farm geometry, it is found that the ratio between the wind-farm energy extraction and turbulent boundary-layer dissipation remains roughly around 70 %, but can be slightly increased by a few percent by penalizing the dissipation in the optimization objective. For a pressure-driven boundary layer in equilibrium, it is estimated that such a shift can lead to an increase in wind-farm energy extraction of 6 %.

The last phase of the dissertation investigates the application of the optimal control to a finite-sized wind farm. A fringe region is employed to impose non-periodicity to the domain and the adjoint for the fringe forcing term is added to the original adjoint LES equations. It is found that the energy extraction increases by 7.3% compared to the uncontrolled case. The value is significantly lower when compared to the optimization of the infinite wind farm. One possible reason for this could be that the turbines in the front row – which contribute 16.5% of the whole farm power in the current case – are already operating close to the optimal condition, and hence, their performance cannot be improved much further by coordinated control. However, even the 7.3% gain achieved in this dissertation can be beneficial, especially for large wind farms.

Beknopte samenvatting

In grote windturbineparken speelt de verticale interactie tussen het park en de atmosferische grenslaag een belangrijke rol, met name de totale energiewinning wordt bepaald door het verticaal transport van kinetische energie vanop grote hoogtes in de grenslaag naar de wind turbines. Dit proefschrift bestudeert de toepassing van optimale controletechnieken in large-eddy simulations (*NL: simulaties van grote wervelingen*) van windturbinepark-atmosferische grenslaag interacties met oog op een verhoogde totale vermogenproductie in windturbineparken. De individuele wind turbines worden beschouwd als stromingsactuatoren wiens energiewinning dynamisch gereguleerd wordt met als doel het stromingsveld en het verticaal transport van turbulente energie optimaal te beïnvloeden. De turbines worden gemodelleerd door actuator disk model (*NL: actuator schijf modellen*) waarvan de rotorschijf-gebaseerde stoot coëfficiënt voor elke turbine tijdsafhankelijk gecontroleerd worden. Zulk een dynamische controle van de stootcoëfficiënten vertegenwoordigt het effect van mogelijke reële controle van het generatorkoppel of de hellingshoek van de wieken, toegepast in een echte windturbine.

In het eerste deel van dit proefschrift wordt de windturbinepark-grenslaag interactie bestudeerd in afwezigheid van gecoördineerde controle van de turbines. De respons van de grenslaag wordt gesimuleerd voor verschillende waarden van de rotorschijf-gebaseerde stootcoëfficiënt, waar de stootcoëfficiënt constant gehouden wordt in de tijd en gelijk is voor alle turbines in het park. Om een correcte referentie voor de dynamische optimale controle te definiëren, wordt het totaal geproduceerd vermogen van het windturbinepark genormaliseerd met drie verschillende referenties, zijnde de wrijvingssnelheid, de geostrofe wind en het aandrijfvermogen van de drukgedreven grenslaag. Voor de schikking van de windturbines beschouwd in dit proefschrift, verschilt de optimale stootcoëfficiënt van de waarde voor optimale werkingscondities van een vrijstaande turbine. Echter, zelfs voor dit optimaal punt, wordt slechts 40% van het totale aandrijfvermogen ontgonnen door het windturbinepark, terwijl 60% hiervan verloren gaat aan turbulente dissipatie.

Het tweede deel van dit proefschrift richt zich op de ontwikkeling van een platform voor gradiënt- en adjoint-gebaseerde algoritmen voor optimalisatie van vermogenproductie van een windturbinepark. Een receding-horizon (*NL: terugwijkende horizon*) aanpak wordt toegepast, waardoor het optimalisatieprobleem wordt opgedeeld in een aantal controlevensters. Binnen ieder van deze controlevensters worden de stootcoëfficiënten dynamisch geoptimaliseerd. De niet-lineaire Polak-Ribière conjugate-gradient (*NL: geconjugeerde gradiënt*) methode en het Brent line search (*NL: lijnzoek*) algoritme worden toegepast om het optimalisatieprobleem op te lossen. De gradiënt van de kostfunctionaal, vereist door de conjugate-gradient methode, wordt berekend met behulp van de continue adjoint methode. De standaard Navier-Stokes adjoint vergelijkingen worden uitgebreid met de adjoint formuleringen van het subgrid-schaal model, het wandmodel en het actuator disk model.

In het derde deel van dit proefschrift wordt de optimale controle van een oneindig groot windturbinepark bestudeerd. De eerste studie richt zich op de directe maximalisatie van de energiewinning. Hieruit blijkt dat de energiewinning toeneemt met 16% in vergelijking met de niet-gecontroleerde referentie. Dit is direct gerelateerd aan een toename in de verticale energiefluxen naar de wind turbines. De verticale afschuifspanningen nemen significant toe. Een verdere analyse ontbindt deze totale spanning in dispersieve en Reynolds spanningen. Hieruit blijkt dat de dispersieve spanningen sterk toenemen. De Reynolds spanningen vertonen een algemene daling, maar nemen echter toe in het zog van de turbines, hetgeen resulteert in een beter herstel van de stroming. Verder toont de analyse dat de turbulente dissipatie in de grenslaag toeneemt. De buitenlaag van de grenslaag bevindt zich in een transiënt afremmend regime, de binnenlaag en de laag op turbinehoogte daarentegen bekomen een nieuw statistisch stationair evenwicht na ongeveer één doorstroomtijd door het windturbinepark. Voor de huidige windparkgeometrie blijkt dat de verhouding tussen ontgonnen energie door de turbines en turbulente dissipatie in de grenslaag ruwweg rond de 70% blijft. Deze verhouding kan licht verhoogd worden door een penalisatie van de dissipatie toe te voegen aan de kostfunctionaal. Voor drukgedreven grenslagen in evenwicht wordt geschat dat zulk een verhoging kan leiden tot een toename in energiewinning van het windturbinepark van 6%.

Het laatste deel van dit proefschrift bestudeert de toepassing van het ontwikkelde optimale controle platform op een windturbinepark van eindige grootte. Een *fringe region* techniek wordt gebruikt om niet-periodische randvoorwaarden in het simulatiedomein op te leggen en de adjoint formulering van de *fringe* krachtterm wordt toegevoegd aan de adjoint LES vergelijkingen. Simulatieresultaten tonen een toename in energiewinning van 7.3% in vergelijking met de ongecontroleerde studie. Deze waarde is gevoelig

lager dan de toename in energiewinning bij optimale controle van oneindige windturbineparken. Een mogelijke verklaring is dat de turbines op de eerste rij-dewelke 16.5% van het totale vermogen leveren in het beschouwde geval-reeds zeer dicht bij optimale condities werken. De performantie van deze turbines kan bijgevolg niet significant verbeterd worden door een gecoördineerd controle-algoritme. Desalniettemin kan de bekomen toename van 7.3% gunstig zijn, zeker in het geval van grote windturbineparken.

Nomenclature

Abbreviations

ABL	Atmospheric Boundary Layer
ADM	Actuator Disk Model
CFL	Courant–Friedrichs–Lewy number
COE	Cost of Energy
DNS	Direct Numerical Simulation
CG	Conjugate gradient
LES	Large-Eddy Simulation
PBL	Pressure-driven Boundary Layer
PDE	Partial Differential Equation
SGS	Subgrid-scale

Greek symbols

α	Angle between the geostrophic wind and the wind in the surface layer; Step length
β_k	Coefficient in the Polak–Ribière conjugate-gradient method
γ	Penalty factor
Γ_i^+, Γ_i^-	Domain boundaries, $i = 1, 2, 3$
$\delta(\boldsymbol{x})$	Dirac delta function
$\delta\boldsymbol{\varphi}^{(k)}$	Search direction
$\Delta_x,\ \Delta_y,\ \Delta_z$	Grid spacing
Δt	Time step
κ	von Kármán constant
$\lambda(x)$	Fringe function
λ'	Tip-speed ratio based on disk velocity
$\boldsymbol{\xi}$	Adjoint velocity
π	Adjoint pressure
ρ	Density

$\boldsymbol{\tau}_M$	Subgrid-scale model
$\boldsymbol{\tau}_M^*$	Adjoint subgrid-scale model
$\boldsymbol{\tau_w}$	Wall stress, $\boldsymbol{\tau_w} = [\tau_{w1}, \tau_{w2}]$
$\boldsymbol{\tau_w^*}$	Adjoint wall stress, $\boldsymbol{\tau_w^*} = [\tau^*_{w,1}, \tau^*_{w,2}]$
$\boldsymbol{\varphi}$	Control vector, $\boldsymbol{\varphi} \equiv [C'_{T,1}(t), C'_{T,2}(t), \cdots, C'_{T,N_t}(t)]$
Φ	Frequency spectrum
$\boldsymbol{\chi}$	Adjoint time-filtered velocity at the turbine rotor disk
ω	Turbine rotation speed
Ω	Computational domain
Ω_D	Horizontal slab of the computational domain in the turbine region (from $z_h - D/2$ to $z_h + D/2$ in the vertical direction)

Roman symbols

a_t	Tangential induction factor
A	Rotor-disk surface area
$\boldsymbol{B}(\boldsymbol{\varphi}, \boldsymbol{q})$	Short hand notation for the state constraints
BT_1, BT_2	Boundary terms
c	Blade chord
$c_L(r)$	Lift coefficient of the blade profiles
$c_D(r)$	Drag coefficient of the blade profiles
C_P	Power coefficient
$C'_{P,i}$	Disk-based power coefficient
C_s	Smagorinsky coefficient
$C'_{T,i}$	Disk-based thrust coefficient
D	Rotor diameter
$\mathscr{D}$	Time-averaged turbulent dissipation per unit farm area
$\mathscr{D}_\Omega$	Total turbulent dissipation per unit farm area
$\boldsymbol{e}_1,\ \boldsymbol{e}_2,\ \boldsymbol{e}_3$	Unit vectors in streamwise, spanwise and vertical directions respectively
$\boldsymbol{e}_\perp$	Unit vector perpendicular to the turbine disk
E	Total kinetic energy
$\boldsymbol{f}$	Forces (per unit mass) introduced by the turbines on the flow
$\boldsymbol{f}^*$	Adjoint forcing term
f_∞	Driving pressure gradient
f_c	Coriolis parameter
F_i	Axial force of a turbine
G	Magnitude of the geostrophic wind
$G(\boldsymbol{x})$	Gaussian filter kernel
H	Domain height
H_G	Boundary layer height

$\mathrm{H}(x)$	Heaviside function
$\mathcal{H}$	Hilbert space
$\mathscr{J}(\boldsymbol{\varphi}, \boldsymbol{q})$	Cost functional
$\tilde{\mathscr{J}}(\boldsymbol{\varphi})$	Reduced cost functional, $\tilde{\mathscr{J}}(\boldsymbol{\varphi}) \equiv \mathscr{J}(\boldsymbol{\varphi}, \boldsymbol{q}(\boldsymbol{\varphi}))$
$\nabla\tilde{\mathscr{J}}$	Gradient of the reduced cost functional
ℓ	Smagorinsky length $\ell = C_s\Delta$
L_{frin}	Length of the fringe region
L_x, L_y	Horizontal domain lengths
$\mathscr{L}$	Lagrangian
N	Number of blades
N_t	Total number of turbines
$\widetilde{p}$	Pressure field
P	Power extracted from the boundary layer by all turbines
P_{ax}	Power extracted at the turbine axle
$\mathscr{P}$	Time-averaged wind-farm power extraction per unit farm area
$\mathscr{P}_\Omega$	Total wind-farm power extraction per unit farm area
$\boldsymbol{q}$	State variables, $\boldsymbol{q} = (\widetilde{\boldsymbol{u}}, \widetilde{p}, \widehat{\boldsymbol{V}})$
$\boldsymbol{q}^*$	Lagrange multipliers and adjoint variables, $\boldsymbol{q}^* = (\boldsymbol{\xi}, \pi, \boldsymbol{\chi})$
R	Turbine radius
$\mathscr{R}_i(\mathbf{x})$	Geometrical smoothing function based on a Gaussian filter
Ro_h	Rossby number
$\boldsymbol{S}$	Resolved rate-of-strain tensor
S_{x}	Streamwise turbine spacing
S_{y}	Spanwise turbine spacing
t	Time
T_A	Optimization control window
$\overline{T}''$	Turbulent transport
$\widetilde{\boldsymbol{u}}$	Resolved velocity field, $\widetilde{\boldsymbol{u}} = [\widetilde{u}_1, \widetilde{u}_2, \widetilde{u}_3]$
$\widetilde{\boldsymbol{u}}_{\mathrm{pre}}$	Inflow velocity for the fringe region method
$u_{\tau l}$	Friction velocity unduced by the ground surface
$u_{\tau h}$	Friction velocity above the turbine
$\langle\widetilde{\overline{u}}_i\rangle$	Mean velocities
$\langle\widetilde{\overline{u}}_i''\widetilde{\overline{u}}_j''\rangle$	Total stresses
$\langle\widetilde{\overline{u}}_i''\widetilde{\overline{u}}_j''\rangle$	Dispersive stresses
$\langle\widetilde{\overline{u}}_i'\widetilde{\overline{u}}_j'\rangle$	Reynolds stresses
U_b	Bulk velocity
V_d	Disk-based velocity
V_i	Disk-averaged velocity
$\widehat{V}_i$	Average axial flow velocity at the turbine rotor disk
W	Relative velocity to the blade

z_0	Surface roughness of the wall
z_1	Vertical location of the first grid point in the computational domain
z_h	Hub height

Subscripts

i	Turbine number, $i = 1 \cdots N_t$
x, x_1	Streamwise direction
y, x_2	Spanwise direction
z, x_3	Vertical direction
FD	Finite difference

Superscripts

k	Conjugate-gradient iteration step
$\circ$	Entry-wise Hadamard product

Miscellaneous symbols

$\langle \cdot \rangle_\Gamma$	Horizontal averages
$\overline{\langle \cdot \rangle}^{T_A}$	Time average over a time window with length T_A

Contents

List of Figures

List of Tables

Chapter 1

Introduction

It has been over 120 years since the first electricity-generating wind turbines were developed separately by James Blyth (Anderson's College, now the University of Strathclyde, in Scotland), Charles F. Brush (Cleveland, United States) and Poul La Cour (Askov, Denmark). Although the basic aerodynamic principle of a wind turbine has remained unchanged, compared to those earlier designs, modern turbines are significantly more advanced and are guided by sophisticated control systems. When considering the size, some of the largest turbines today have a rotor diameter of 160 meters and can generate up to 8 MW of electricity (cf. figure 1.1). Similarly, the size of wind farms has also increased rapidly and the power production of these mega-farms are comparable to conventional thermal and nuclear power plants. The largest offshore wind farm to date is the 630 MW London Array with 175 turbines spread over an area of 100 km^2. The Alta Wind Energy Center in California, USA is currently the largest onshore windfarm with an operational capacity of 1.3 GW. According to the annual report released by the Global Wind Energy Council (GWEC), the global cumulative of installed wind energy capacity has reached 318 GW (cf. figure 1.2) in 2013, an increase of more than 250 GW in the last 10 years [37]. Just in 2013, more than 35 GW of new wind turbines were brought online.

Despite all the developments and encouraging facts and figures, wind energy still faces many engineering challenges which need to be addressed so that the technology can be more competitive with traditional power plants. For example, most commercial turbines, when operating below the rated wind speed, use generator torque control and simply try to produce as much power as possible (cf. §1.2.1). For a lone-standing turbine, this is aerodynamically efficient and maximizes the energy extraction. However, this approach ignores

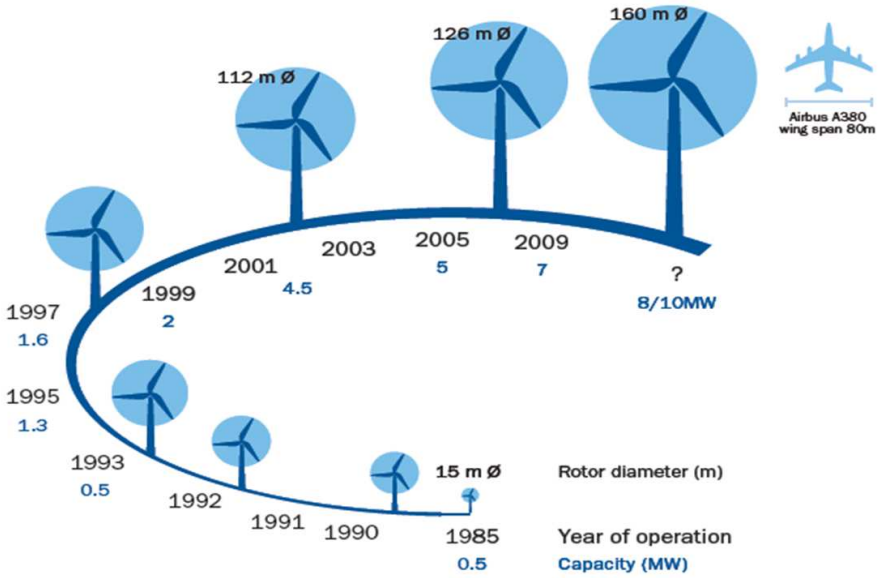

Figure 1.1: Evolution of turbine size and capacity. Reproduced from EWEA factsheet [28].

the interaction between wind turbines in a farm and therefore, may not optimize the total energy extraction from a wind farm. Furthermore, turbines in a farm operating in such conditions experience higher dynamic loads compared to a lone-standing turbine. These factors increase the Cost of Energy (COE) of wind power by reducing the overall efficiency of farms or by increasing the structural loading and reducing the life time of turbines.

As the number and size of wind farms continue to increase, interest has recently been shifting from single turbine controllers to advanced coordinated controllers at the farm level. A typical example of such a control approach is to reduce the effect of wake interaction and hence optimize the overall farm performance by adjusting the blade pitch and generator torque of each individual turbine based on information from neighboring turbines [54, 92, 29]. Other studies have also considered yaw control, in which the wake from upstream turbines is deflected away from downstream turbines using yaw misalignment [51, 30].

The current dissertation investigates the use of optimal control techniques combined with large-eddy simulations (LES) of wind-farm boundary-layer interactions for increasing the total energy extraction in large wind farms. To

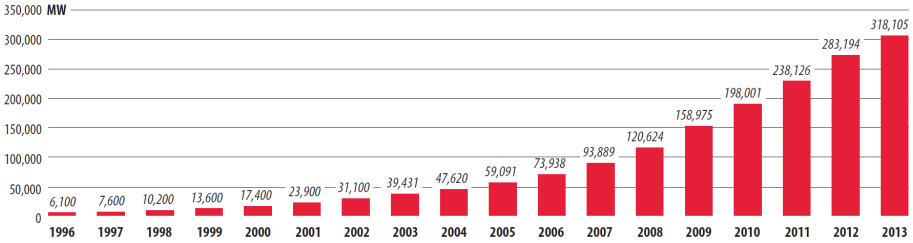

Figure 1.2: Global cumulative of installed wind energy capacity 1996–2013. Reproduced from GWEC: Global Wind Report 2013 [37].

this end, the individual wind turbines are considered as flow actuators, whose energy extraction can be dynamically regulated in time so as to optimally influence the flow field and the vertical turbulent energy transport, thereby maximizing the wind farm power.

In the following section, first the current status and findings of wind farm and atmospheric boundary layer (ABL) interactions is discussed. Section 1.2 provides information about control system used by modern commercial wind turbines and discusses approaches and challenges for the control and optimization of wind farms. Adjoint-based optimization and its application to the flow control problem is briefly reviewed in Section 1.3. Finally, in Section 1.4, aims and objectives are presented followed by an outline of the dissertation in Section 1.5.

1.1 ABL-wind farm interaction

In large wind farms, the effect of turbine wakes and the accumulated local energy extraction from the atmospheric boundary layer lead to a reduction in farm efficiency, with turbines in a farm generating up to 50% less power than a lone-standing turbine [44]. Measurements from the Horns Rev wind farm, as shown in figure 1.3, clearly indicate a significant power deficit starting from the second row; in particular, for a turbine spacing of $7D$, the deficit is higher than 40%. More detailed measurements and analysis of data from the Horns Rev wind farm can be found in Barthelmie *et al.* [7] and Hansen *et al.* [44].

Recently, a number of LES and experimental studies (see e.g. Ref. [16, 72, 1, 67, 62]) have been performed to investigate various aspects of wind farm and ABL interactions. One important conclusion that can be drawn from these studies is that *in very large wind farms or 'deep arrays', the interaction of*

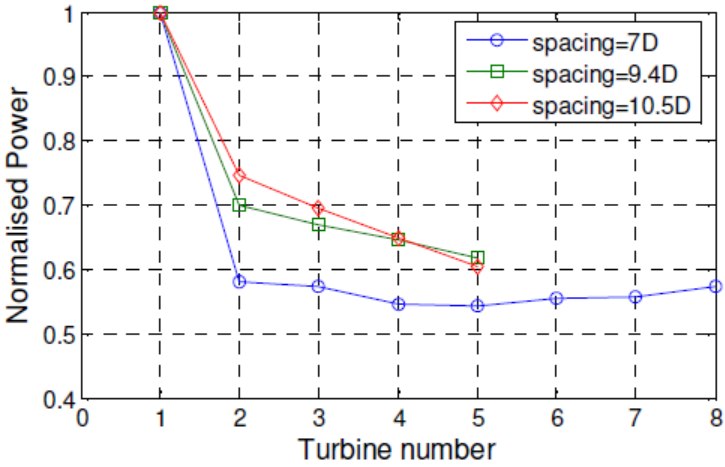

Figure 1.3: Power deficit inside Horns Rev wind farm for 8 m/s inflow and different turbine spacing. Reproduced from Barthelmie *et al.* [8].

the wind farm with the planetary boundary layer plays a dominant role in the efficiency loss mentioned above. For such cases, Calaf, Meneveau & Meyers [16] and Cal *et al.* [15] demonstrated that the wind-farm energy extraction is dominated by the vertical turbulent transport of kinetic energy from higher regions in the boundary layer towards the turbine level. Later, this was further corroborated in a series of studies, relying both on simulations (see e.g. Ref. [113, 72, 4]), as well as on wind-tunnel experiments [67, 62, 78]. Yang *et al.* [113] numerically studied the effects of turbine spacing in large aligned wind farms and found that larger streamwise spacing is more effective in increasing the power extraction and also in reducing the turbulence intensity at the turbine than when the spanwise spacing is increased. The reason for this dominant effect of the streamwise spacing is that the recovery of the wind-turbine wake depends on the area influenced by the wake and not on the land area occupied by each turbine. In their LES study, Wu & Porté-Agel [109] investigated the effect of wind farm layout on the flow structures by comparing results for aligned and staggered farms. They showed that the staggered farm is more efficient in energy extraction because of the fact that the distance between consecutive wind turbines is larger in this configuration, allowing for better wake recovery. Their results are in agreement with wind tunnel experiments of Chamorro *et al.* [20] and Markfort *et al.* [67]. Staggered configurations also exhibit stronger wake regions behind turbines due to better momentum transfer from the flow above.

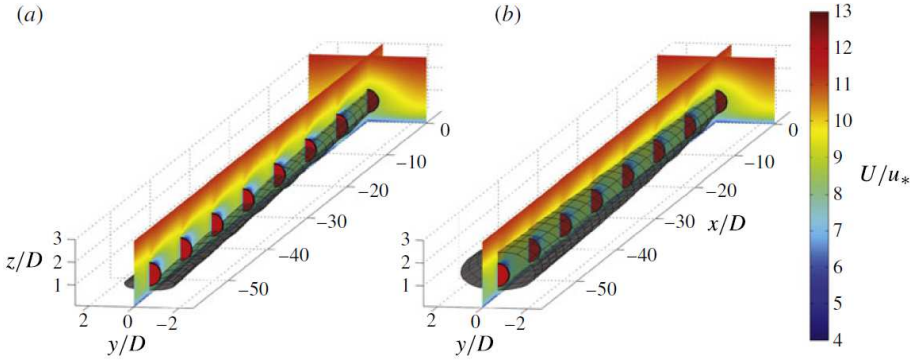

Figure 1.4: Mean streamwise velocity field: (a) stream tube; (b) total mechanical energy tube in a turbine row of a fully developed wind-turbine-array boundary layer. Reproduced from Meyers & Meneveau [72].

In an attempt to further understand the energy transport mechanism, several studies have tried to analyse the terms in the kinetic energy equation or have used visualization techniques such as stream tube analysis. For instance, Newman *et al.* [78] examined mean kinetic energy equations using control volumes defined at the level of the rotors. They observed that the terms involving wall normal mean velocity vary significantly in the streamwise direction, and the flux due to the mean streamwise velocity and the shear stress, transport the energy into the rotor region from both above and below the turbines. Lebron *et al.* [62] constructed a stream tube from a PIV measurement of a model wind farm, and examined the relevant fluxes of kinetic energy (including those due to turbulence) through the periphery of their stream tube. In addition to the classical stream tubes, Meyers & Meneveau [72] came up with the concept of momentum and energy transport tubes (see figure 1.4) and applied them to fully developed wind-turbine array boundary layers. From the energy tubes, they demonstrated that for wind farms with large spanwise spacings, the sideways energy flux is dominant, while for smaller spanwise spacings, the top-down flux is more important. However, sideways fluxes are also fed by a top-down mechanism in regions between turbine rows.

The LES data from wind-farm simulations can also be utilized for the identification of the dominant turbulent structures and provide a better insight into spatial and/or temporal patterns in wind-farm boundary layers. Such an analysis could be greatly beneficial for the construction of reduced order models, improvement of the wake models and ultimately, the development of better wind-farm controllers. Proper orthogonal decomposition (POD) is considered as a strong candidate for this purpose by several researchers [4, 9].

A three-dimensional POD analysis performed by VerHulst & Meneveau [104] suggests that streamwise counter rotating vortex pairs above the wind turbines are primary large-scale structures in the wind-farm boundary layers. It should also be remarked that to capture 80% of the flux, they only required 6% of the total modes needed to construct full flow fields.

One of the major challanges in wind-farm simulations is the correct representation of the ABL, which includes the effects of Coriolis forcing, thermal stratification and capping inversion. Most of the studies outlined above have considered a neutral pressure-driven boundary layer. Although these studies have provided much valuable information, more accurate representations of the ABL will be crucial, particularly because sizes of turbines and wind farms are increasing. The turbulence characteristic and the height of the boundary layer (H_G) are greatly affected by the buoyancy due to the surface temperature flux, which further depends on the diurnal cycle. During the daytime, due to surface heating, turbulence is predominantly generated by buoyancy and the height H_G increases with time due to entrainment from the free atmosphere. This type of boundary layer is called convective or unstable. On the other hand, during a clear night when the surface is cooler than the air above, negative buoyancy acts as a sink to the turbulence, resulting in a shallower boundary layer. This is called a stable boundary layer. Finally, when the effect of the surface temperature flux is negligible and the turbulence is predominantly generated mechanically due to wind shear, the boundary layer is called neutral. Usually, neutral boundary layers develop against the background of stable stratification; as in the case of the so-called conventionally neutral boundary layer [116].

The effect of Coriolis forces on very large wind farms was investigated by Johnstone & Coleman [55]. Their results indicated a good agreement with the surface roughness model proposed by Calaf, Meneveau & Meyers [16]. But the presence of a wind farm increased the boundary layer height and the rotation of the velocity vector away from the geostrophic wind G, implying the presence of a link between power extraction and strongly skewed flow. Lu & Porté-Agel [64] investigated the interactions between a stably-stratified ABL and an infinite farm. Abkar & Porté-Agel [1] studied the effect of free-atmosphere stratification on the structure of the ABL and the wind farm's power, and demonstrated that the presence of turbines significantly affect the ABL height. They also found that thermal stratification hindered the growth of the boundary layer, leading to lower energy entrainment from the flow above, and hence, lower power production by the wind farm. For large wind farms in a conventionally neutral ABL, Allaerts & Meyers [3] showed that the growth of the ABL height is limited by the capping inversion strength, which also reduces the entrainment at the top of the boundary layer.

In the current dissertation, a neutral pressure-driven boundary layer with

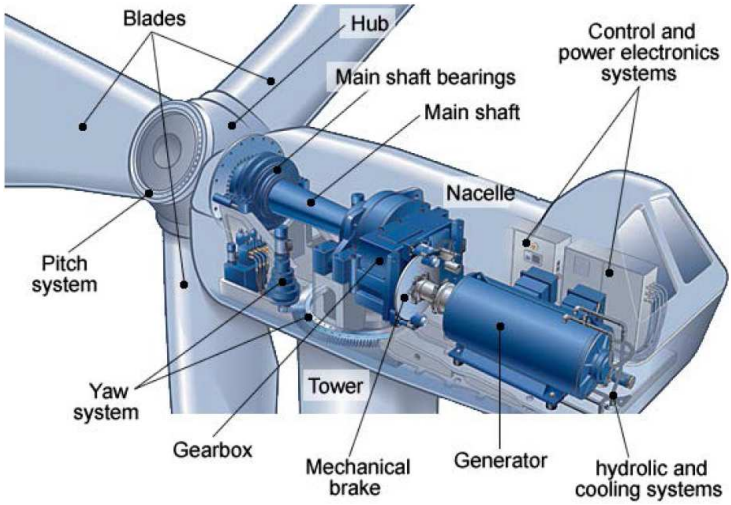

Figure 1.5: Main components of a utility-scale wind turbine. Reproduced from Tchakoua *et al.* [100].

symmetry conditions at the top is considered, instead of a full conventionally neutral atmospheric boundary layer that is driven by a geostrophic balance and includes free-atmosphere stratification, a capping inversion layer between the ABL and the free atmosphere, etc. Such an approach is relatively common for simulations of near-surface features in atmospheric boundary layers, and has been used also in the context of wind-farm simulations by many of the studies reviewed above [16, 17, 113, 4]. It presumes that the turbines are situated in the inner layer of the boundary layer (cf. Calaf, Meneveau & Meyers [16] for a more detailed discussion). This working hypothesis is limited by the fact that the turbines in the current dissertation are close to the upper limit of the inner layer, i.e. the hub height is 100 meters, while the top tip height is 150 meters, for a boundary layer height of 1km. Nevertheless, it is believed that such an approach is a good approximation for a first analysis of the optimal control of wind-farm boundary layers, and results are carefully discussed in view of differences to a real ABL.

1.2 Wind-turbine and wind-farm control

Modern wind turbines have multiple airfoil-shaped blades (usually 2 or 3 for a horizontal axis turbine). These blades capture kinetic energy from the incoming

wind and transform it into mechanical energy in a rotor shaft, which in turn drives a generator to produce electrical energy. Usually, the low-speed rotor shaft is connected through a gearbox system to the generator, so that the lower rotational speed of the rotor can be transformed into a higher rotation required by the generator. However, some turbine designs do not require a gearbox; in such cases, the generator is directly attached to the rotor shaft and spins at the same speed as the blades. The typical main components of a utility-scale wind turbine are shown in figure 1.5.

The aerodynamic efficiency of a turbine is defined by the power coefficient, i.e, $C_P = P/P_{\text{wind}}$. Here P is the actual power extracted by the turbine, and P_{wind} is the maximum energy flux available in the wind, given by

$$P_{\text{wind}} = 1/2\rho A u_{\text{wind}}^3, \tag{1.1}$$

where ρ is the density of the air, A is the area swept by the rotor, and u_{wind} is the wind speed. Although this is the maximum energy available in the wind, even an ideal wind turbine design with no losses (due to drag etc.) cannot capture all of it. Doing so would mean reducing the wind speed to zero at the turbine and, thus, no more wind can pass through the rotor to provide energy. A theoretical upper limit for the wind turbine efficiency is dictated by the Betz limit, which states that no more than 59.3% (i.e. $C_{P,\max} = 16/27 = 0.593$) of the total kinetic energy available in the wind can be captured by a turbine [14]. Thanks to advances in the design and optimization of rotor blades as well as other components, modern wind turbines are capable of operating close to the Betz Limit, with $C_P \approx 0.5$ [45]. Additionally, developments in advanced controllers have also contributed significantly to increasing the energy capture by turbines and improving their overall performance.

This section first provides information about some of the most important actuation systems that are used to achieve certain control objectives in modern commercial turbines (§1.2.1). This is followed by a brief discussion of the different operational regions of a turbine. Subsequently, approaches and challenges for the control and optimization of wind farms is discussed in §1.2.2.

1.2.1 Operation and control of wind turbines

Most utility-scale horizontal-axis wind turbines (HAWT) have three principal actuation systems, namely, (i) yaw control, (ii) generator torque control, and (iii) blade pitch control. The aim of yaw control is to turn the nacelle and the rotor so that the turbine aligns itself with the incoming wind to maximize the power output. Wind direction signals from a wind vane mounted on the nacelle is used to calculate the yaw error. This is then used as an input for

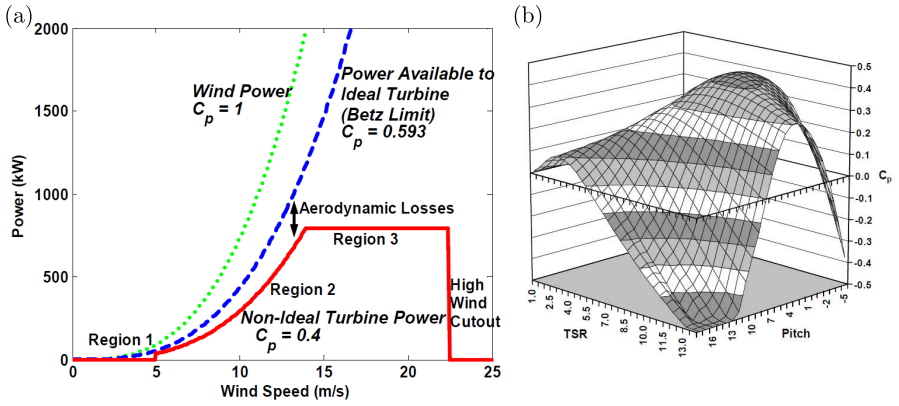

Figure 1.6: (a) Steady-state power curve. (b) An example of $C_p - \lambda$ – pitch angle surface. Reproduced from NREL technical report [53].

the yaw motor which turns to adjust the misalignment between the turbine and the incoming wind. For a large turbine, yaw control is performed at a very slow rate (less than 1 deg/s) in order to minimize the effect of gyroscopic forces [81]. However, as discussed below in §1.2.2, for farm-level control, some studies intentionally allow yaw misalignment to deflect the wake away from downstream turbines. This helps to improve the overall performance of a farm.

Generator torque control is a common actuation mechanism in variable-speed wind turbines. It uses the difference between the aerodynamic torque acting on the rotor and the torque from the generator as a mechanism to control the rotor speed. For instance, below the rated wind speed, the generator torque is actively varied to accelerate or decelerate the rotor and achieve the optimal tip-speed ratio. The generator torque is usually maintained at a constant value above the rated wind speed.

Finally, pitch control is another common mechanism of controlling wind turbine power output by changing the angle of attack of the blades. Blade pitch control is achieved either by using the combination of a piston placed inside the hollow main shaft and a hydraulic pressure tap or more commonly by using motors fitted to each blade [45]. Most wind turbines use full-span blade pitch control. Though not very common, there are turbines which use pitching of the blade tips or blade mounted flaps to achieve similar control objectives. Wind turbines can have collective pitch control, in which the pitch angle is adjusted identically for all blades, or individual pitch control for each blade. It is necessary that the pitch control response is fast enough to react to rapid changes in wind conditions and achieve good performance.

Control strategies for different regions of operation are discussed next. As shown in figure 1.6(a), depending on the wind speed and turbine design specification, modern wind turbine operation can be divided into three main control regions. Below the cut-in wind speed, the energy in the wind is not enough for the turbine to generate power from, and thus, the turbine does not operate in this low-wind region. This is known as Region 1. Generally, in this region, the turbine (or more precisely, the sensors) monitors the wind speed and sends information to the supervisory control, which determines if the condition is suitable for start-up or not.

Region 2 lies between the cut-in speed and the rated wind speed. In this region, it is desirable to operate the turbine at the maximum possible aerodynamic efficiency. Generator torque actuation is considered the most effective control mechanism for Region 2 control. The torque is controlled with the aim of adjusting the rotor speed relative to the varying wind speed, so that the optimum tip-speed ratio with peak aerodynamic efficiency can be maintained. Active pitch control is not necessary in Region 2 operation and the blade pitch angle is simply set to its optimum value corresponding to the peak C_P value illustrated in figure 1.6(b).

When the wind speed is above the rated speed (and below the cut-out speed), the turbine is said to be operating in Region 3. At the rated speed the turbine achieves the maximum power output that the generator is capable of, also called rated power. For higher wind speeds, the turbine has to limit the power production to the rated output so that it does not exceed the design limits of the electrical and mechanical components. In Region 3 operation, blade pitch control is used to regulate the power output and reduce the aerodynamic torque. The turbine maintains the constant rotor speed which corresponds to the rated speed, so that it does not exceed the rated power. When the wind speed is higher than the cut-out speed, the turbine is actively shut down in order to protect the wind turbine structure from excessive loading and risk of damage.

Before closing this subsection, it should be remarked that some controllers employ an additional Region 2.5 control, to enable a smooth transition between Region 2 and Region 3 [81].

1.2.2 Wind farm: optimization and control

A lot of studies have considered the optimization of wind-farm performance, many of them focusing on the optimization of the farm lay-out both in small farms [57, 60, 23] and in large arrays [77, 71, 95]. The general trend in layout optimization is to formulate analytical wake models and couple them

with techniques such as genetic algorithms [40], the evolutionary strategy algorithm [60] or particle swarm optimization [23], among others. For example, Chowdhury *et al.* [23] reported a remarkable increase in total power output (about 40%) when the optimum farm layout was combined with turbines with different rotor diameters. Although these algorithms have presented promising results for smaller farms, they may not be equally effective in large wind farms which have a large number of parameters and far more complex dynamics. For large wind-turbine arrays, Meyers & Meneveau [71] have predicted an optimal turbine spacing as a function of wind farm induced surface roughness as well as in terms of the ratio of turbine costs to land surface costs. Stevens *et al.* [96] studied the effect of incoming flow direction on the wind-farm alignment and found that a perfectly staggered configuration does not necessarily optimize the farm efficiency. In fact, the highest power output was obtained for an intermediate angle, since such a configuration was able to minimize the wake interactions.

Wind-farm control has also received considerable attention, focusing on various aspects of wind-farm operation such as reduction of structural loads, power regulation and grid support, or increasing energy extraction [93, 43, 54, 92]. One of the earliest applications of farm-level control was investigated by Steinbuch *et al.* [94]. They proposed a concept of downrating the power output from upwind turbines in a farm by reducing their tip-speed ratio, so that the wind speed in their wake would be higher. This would be beneficial for downstream turbines and, as a result, may also increase the total energy capture of the wind farm. Most of the developments in coordinated control are mainly based on the modification of the operational setpoint of the axial induction factor for each turbine in a farm, such that the overall energy capture of the arrays would increase [54, 59]. The axial induction factor can be modified by adjusting the blade pitch and generator torque. Horvat *et al.* [47] used a wake model to describe the aerodynamic coupling between turbines and solved the optimization problem by using sequential quadratic programming in Matlab. Their first objective was to find the optimum rotor speed for each turbine for which the wind farm achieves the maximum power in region 2 operation. The second objective was to optimize the wind-farm load in region 3 operation by evenly redistributing the load among the turbines. Soleimanzadeh *et al.* [91] employed a dynamic wind-farm model based on the two-dimensional linearized Navier-Stokes equation to develop a distributed wind-farm controller for load mitigation. The performance of new control strategies can also be evaluated in a high-fidelity CFD environment; for example, NREL has developed an LES-based framework called SOWFA (see Ref. [24, 29]) that allows the implementation and testing of multi-turbine control algorithm.

Several model-free approaches for wind-farm optimization have also been

proposed in the literature [114, 66, 35]. Such approaches have an advantage over model-based schemes as the latter usually rely on simplified wake models that cannot correctly describe the chaotic nature of the aerodynamic interactions in wind farms, or are based on more complex CFD-based models that are computationally demanding and, therefore, not suitable for online optimal control. Marden *et al.* [66] proposed two game theory-based distributed learning algorithms. In their first algorithm, each of the turbines is required to have knowledge regarding the total wind farm power production. In the second algorithm, individual turbines only require knowledge regarding the power produced by the turbine itself and limited information about neighboring turbines. Gebraad & van Wingerden [35] presented a data-driven control scheme that optimized the control settings of each turbine in a wind farm and adapted them to the time-varying wind speed. The scheme uses a gradient-based optimization technique to update the turbine control parameters in a distributed approach and only takes into account information from neighboring turbines. A model-free approach based on Multi-Resolution Simultaneous Perturbation Stochastic Approximation (MR-SPSA) was proposed by Ahmad *et al.* [2]. This method achieves faster convergence and even outperforms several other model-free approaches in terms of maximum power production.

Wind farm efficiency can also be increased by redirecting the wake away from downstream turbines. One method of achieving this wake deflection is through yaw misalignment of the upstream turbine, such that its wake avoids the downstream turbine. Fleming *et al.* [31] examined the potential of a wake-redirection-based control for a two-turbine case in large-eddy simulations using SOWFA. In addition to yaw misalignment, they further investigated the tilt angle-based method to redirect the wake upward or downward and individual pitch control to achieve a horizontal and vertical wake skew by inducing a yaw or tilt moment [30]. The maximum increases in power were 4.6% and 7.1% in yaw- and tilt-based control, respectively. Gebraad *et al.* [34] also presented a wind- farm control strategy that optimizes the yaw settings for a larger farm with 3×2 turbines. Another method for wake avoidance as proposed by van Wingerden [103] is repositioning of downstream turbines in a floating wind farm. This floating wind-farm control concept was later investigated by Fleming *et al.* [31] in CFD simulations.

However, as far as wind-farm–flow interactions are included in the studies discussed above, they are all based on fast heuristic models: e.g. models for wake interaction and merging such as presented by [63], [50] or [85] (see also Sanderse *et al.* [87] for a review), or models for boundary-layer response in large farms (see e.g. Ref. [32, 16, 69]). It should be noted that some of the control schemes presented above (see e.g. Ref [30, 31, 34, 35]) have been tested in high fidelity CFD-based models and have proven to be effective in improving

wind-farm performance. The current dissertation considers the optimal control of wind farms using large-eddy simulations of the wind-farm boundary layer as the state model, which allows for a detailed optimization of the dynamic interaction of the farm's turbines with the boundary layer and its large-scale three-dimensional turbulent structures.

In large-eddy simulations of wind-farm boundary layers, it is computationally not feasible to fully resolve blades and blade boundary layers on the mesh. Instead, simplified models are used that provide the turbine forces on the LES flow field. The most common is the Actuator Disk Model (ADM), in which a uniform force in the turbine disk region is smoothed onto the LES grid [75, 52, 48, 70, 16]. This dissertation employs such an ADM model, with a disk-based thrust coefficient that is dynamically controlled per turbine in time (see §3.2 for further discussion). It is presumed that this dynamic control of the thrust coefficient represents the possible blade pitch and generator torque-based control discussed above. Inclusion of all three actuation mechanisms discussed in §1.2.1 requires more detailed representations of wind-turbines, which will further complicate the implementation of the optimization algorithm. Therefore, it remains beyond the scope of this dissertation.

1.3 Adjoint approach to optimization

To date, the combination of optimal control techniques with time-resolved turbulent flow simulations such as direct numerical simulation (DNS) or LES has been mainly used for drag reduction in boundary layers [21, 10], noise control in jets [107], optimal nonlinear growth of mixing layers [26, 27, 5], or enhancing the turbulent mixing rate in jet flows [80]. All of these cases are PDE-constrained optimization problems with a large number of degrees of freedom in the control space, and a huge number in the state space. For instance, in the current study, the number of degrees of freedom in the control space is approximately 20,000, while the space-time state space has about 1.5 billion degrees of freedom. In such a case, the only viable optimization approach is gradient-based optimization combined with an adjoint-based gradient method. The adjoint-based method is discussed next.

The Adjoint method is a powerful tool for the computation of sensitivities in the gradient-based optimization of a large-scale problem. The gradient evaluation in this method is independent of the number of control parameters and can be achieved at the cost of one forward and one adjoint simulations, also called primal and adjoint solutions. There are two different methods for the derivation and implementaion of the adjoints, namely, the *continuous*

approach and the *discrete* approach. In the continuous approach, the adjoint equations are obtained from the differentiation of the governing equations (in their original continuous form) with respect to the control parameters. This is then discretized and solved to compute the gradient. On the other hand, in the discrete approach, the discretized form of the governing equations are differentiated to obtain a set of discrete adjoint equations. For an infinitely fine grid resolution, both methods should give the same gradient. However, this will not be the case for a finite grid resolution, since the differentiation as well as the discretization in both approaches follow different paths [41]. Advantages and disdavantages of these two methods have been discussed in detail in the literature and are therefore not discussed any further. For more comprehensive discussion on the derivation and application of the adjoint methods, the reader is referred to Gunzburger [41], Troltzsch[102], Giles and Pierce [36] and other related articles. In the current dissertation, the continuous adjoint method is chosen for the gradient evaluation, since it can easily be adapted to the optimization with different objective functions. Additionally, because of the strong resemblance between the adjoint and flow equations, it is possible to reuse much of the discretization from the forward problem, making the task of implementation easier.

1.4 Aims and Objectives

The main goal of this dissertation is to investigate the optimal control of wind-farm boundary layers in large-eddy simulations with the aim to increase wind-farm energy extraction. To this end, a receding-horizon optimal control approach is employed and conjugate-gradient algorithm in combination with adjoint LESs are used for the determination of the gradients of the cost functional. Although such a framework is not practicable for real wind-farm application, the insight and understanding gained from this dissertation can be used for the development of real-time active controllers. Furthermore, techniques and algorithms developed in this dissertation provide important guidance for future optimization studies of wind farms with different objectives.

The thesis also aims to give better insight into the mechanism responsible for improved energy extraction in wind farms.

The main objectives for the current dissertation can be summarized as follows:

1. Development of an optimal control framework for a gradient and adjoint based scheme for wind farm power optimization. The main extensions to the existing tool [26, 27] are the derivation and implementation of

- adjoints of the subgrid-scale model
- adjoints for the wall-stress model
- adjoints for the wind turbine model

2. Optimal control of energy extraction in infinite wind farms.
3. Explore the influence of penalizations to the original farm-power based cost functional.
4. Optimal control of energy extraction in finite wind farms.

1.5 Outline

In Chapter 2, the wind-farm-ABL interaction in the absence of optimal control of the turbines is studied with the aim to gain insight into the response of a wind-farm boundary layer to a different farm loading. Additionally, wind-farm simulations in the pressure-driven boundary layers are compared with simulations governed by the geostrophic balance between the Coriolis force and the pressure-gradient. First of all, Section 2.1 presents the governing flow equations for large-eddy simulation and the discretization scheme used in this dissertation, and also discusses about the model for wind turbine representation. In Section 2.2, the results for the boundary layers driven by a geostrophic balance and Coriolis forces are presented. Section 2.3 focuses on the response of the boundary layer and energy extraction for standard turbine control.

Chapter 3 presents the optimization approach used in this dissertation. The chapter starts with the discussion about a receding-horizon control approach employed for the wind-farm power optimization. In this approach, the control problem is split into a number of optimal control sub-problems. The formulation of these sub-problems is subsequently introduced in Section 3.2, followed by optimization method in Section 3.3. Gradient and adjoint-based approaches are elaborated in Section 3.4, and adjoint equations are derived in Section 3.5. Finally, the adjoint equations are verified by comparing the adjoint-based gradients with those obtained from a classical finite difference approach in Section 3.6.

In Chapter 4, the results of the optimal coordinated control of infinite wind-farm boundary layers are presented. First of all, Section 4.1 provides details about the computational set-up. Subsequently, in section 4.2, optimal control results are presented for the wind-farm control case in which the cost functional is simply the amount of energy extracted by the farm, and has no penalization

term. Section 4.3 presents the optimal control results for two additional cases where turbulent dissipation is penalized.

Chapter 5 investigates the application of the optimal coordinated control to a finite sized wind farm. The chapter first introduces modified governing flow equations including the fringe forcing term in Section 5.1. The adjoint for the fringe forcing term is also derived in this section. This is followed by the description of the case set-up in Section 5.2. Characteristics of the controls and the optimized power output are discussed in Section 5.3, and time averaged flow profiles are presented in Section 5.4

Finally, in Chapter 6, main conclusions and future research directions are discussed.

Chapter 2

Simulation of a wind-farm boundary layer

In this chapter, the wind-farm-ABL interaction in the absence of coordinated control of the turbines is studied. These studies provide insight into the response of a wind-farm boundary layer to a different farm loading and also serve as a reference for the optimal control studies in the following chapters. Additionally, wind-farm simulations in pressure-driven boundary layers are compared with simulations governed by the geostrophic balance between the Coriolis force and the pressure-gradient. Various relevant physics such as roughness length, variation in boundary layer height etc., are investigated.

The governing flow equations for large-eddy simulation are presented first in Section 2.1 along with the model for wind turbine representation and the discretization scheme. In Section 2.2, the results for the boundary layers driven by a geostrophic balance and Coriolis forces are presented. To this end, a number of cases are setup based on the ABL height and the geometrical arrangement of the turbines. The work discussed in this section is published in Goit & Meyers [38]. Section 2.3 focuses on the response of the boundary layer and energy extraction for standard turbine control. This involves simulations with different C_T' values. The C_T' value is kept constant in time and is kept the same for all the turbines in a simulation so as to determine the optimal C_T' setting which leads to the maximum energy extraction from the farm. A physical interpretation regarding the increase in the power extraction is also presented.

2.1 Numerical methods for large-eddy simulation

In this section, the governing flow equations, the model for wind turbine representation and the discretization scheme are presented. The flow equations for the large-eddy simulations are introduced first in §2.1.1. The subgrid-scale model together with the wall stress model and other boundary conditions are also discussed in this subsection. The forces exerted by wind turbines on the flow are represented using the actutator-disk model in the current dissertation. The implementation of the actuator-disk model is presented in §2.1.2. Finally, §2.1.3 describes discretization techniques and other details about the simulation tool.

2.1.1 Governing flow equations

A thermally neutral pressure-driven boundary layer, with a constant pressure gradient $-\nabla p_\infty/\rho \equiv f_\infty \boldsymbol{e}_1$ (with $\boldsymbol{e}_1$ being the unit vector in the streamwise direction) is considered. The governing equations are the filtered incompressible Navier-Stokes equations for neutral flows and the continuity equation, i.e.

$$\nabla \cdot \widetilde{\boldsymbol{u}} = 0 \tag{2.1}$$

$$\frac{\partial \widetilde{\boldsymbol{u}}}{\partial t} + \widetilde{\boldsymbol{u}} \cdot \nabla \widetilde{\boldsymbol{u}} = -\frac{1}{\rho}\nabla \widetilde{p} + f_\infty \boldsymbol{e}_1 + \nabla \cdot \boldsymbol{\tau}_M + \boldsymbol{f} \tag{2.2}$$

where $\widetilde{\boldsymbol{u}} = [\widetilde{u}_1, \widetilde{u}_2, \widetilde{u}_3]$ is the resolved velocity field, $\widetilde{p}$ is the remaining pressure field (after subtracting p_∞), $\boldsymbol{\tau}_M$ is the subgrid-scale model, and density ρ is assumed to remain constant. Furthermore, $\boldsymbol{f}$ represents the forces (per unit mass) introduced by the turbines on the flow (see discussion in §2.1.2). Since the Reynolds number in atmospheric boundary layers is very high, the resolved effects of viscous stresses in the LES are neglected.

The computational domain is schematically represented in figure 2.1. In streamwise and spanwise directions, periodic boundary conditions are used (i.e. respectively on Γ_1 and Γ_2). Note, however, that for the simulation and control of a finite farm in Chapter 5, a *fringe-region* method is used, which damps wakes downstream of wind farm and impose a clean inflow boundary layer profile. More on the implementation of the *fringe-region* method is discussed in Chapter 5. At the top boundary (Γ_3^+) symmetry conditions are imposed. At the ground surface (Γ_3^-), impermeability is imposed in combination with Schumann's [89] wall-stress boundary conditions and Monin–Obukhov similarity theory for neutral rough boundary layers. It relates the wall stress $[\tau_{w1}, \tau_{w2}]$ to the wall-

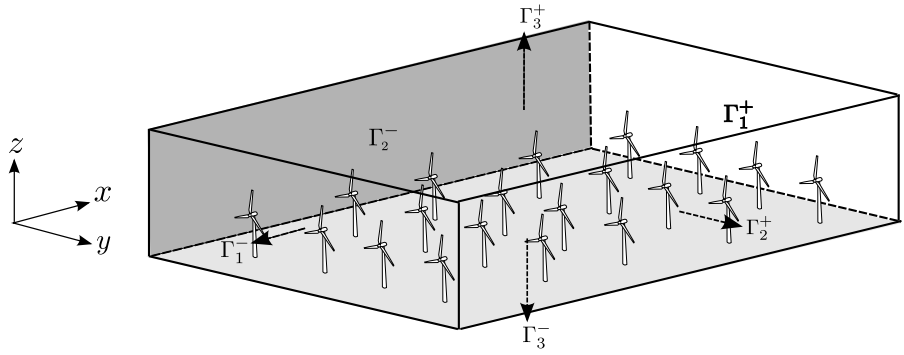

Figure 2.1: Computational domain Ω and boundaries Γ

parallel velocity components $[\widetilde{u}_1, \widetilde{u}_2]$ at the first grid point using [76, 13]

$$\tau_{w1} = -\left(\frac{\kappa}{\ln(z_1/z_0)}\right)^2 \left(\overline{\widetilde{u}}_1^2 + \overline{\widetilde{u}}_2^2\right)^{0.5} \overline{\widetilde{u}}_1, \tag{2.3}$$

$$\tau_{w2} = -\left(\frac{\kappa}{\ln(z_1/z_0)}\right)^2 \left(\overline{\widetilde{u}}_1^2 + \overline{\widetilde{u}}_2^2\right)^{0.5} \overline{\widetilde{u}}_2, \tag{2.4}$$

where z_0 is the surface roughness of the wall, and z_1 is the vertical location of the first grid point. Furthermore, the bar on $\overline{\widetilde{u}}_1$ and $\overline{\widetilde{u}}_2$ represents a local average obtained by filtering the wall-parallel velocity $[\widetilde{u}_1, \widetilde{u}_2]$ in directions parallel to the wall, avoiding an overestimation of the wall stresses [13]. In the current dissertation, two successive one-dimensional Gaussian filters with filter width 4Δ (where Δ is the grid spacing) are used.

In view of the complexity associated with the formulation of the adjoint equations and the adjoint subgrid-scale model required for the optimal control (cf. Chapter 3), a relatively simple subgrid-scale (SGS) model is chosen, i.e. the Smagorinsky model [90] with wall damping,

$$\boldsymbol{\tau}_M = 2\ell^2 (2\boldsymbol{S} : \boldsymbol{S})^{1/2} \boldsymbol{S}, \tag{2.5}$$

with $\boldsymbol{S} = (\nabla\widetilde{\boldsymbol{u}} + (\nabla\widetilde{\boldsymbol{u}})^T)/2$ being the resolved rate-of-strain tensor. The Smagorinsky length ℓ ($= C_s\Delta$ far from the wall) is damped using Mason & Thomson's [68] wall damping function, i.e. $\ell^{-n} = [C_s\Delta]^{-n} + [\kappa(z + z_0)]^{-n}$, where $\kappa = 0.4$ is the von Kármán constant, and where $n = 3$ is taken. Furthermore, $\Delta = (\Delta_1\Delta_2\Delta_3)^{1/3}$ is the local grid spacing, and C_s is the Smagorinsky coefficient. In this dissertation, $C_s = 0.14$, consistent with

the high-Reynolds-number Lilly value for cubical sharp cutoff filters [73] is employed. Note that some other works have used more advanced subgrid-scale models in the LES of wind farms, such as the scale-dependent Lagrangian model of Bou-Zeid *et al.* [13] [16, 17, 1]. In [16] a comparison was made between this model and the current Smagorinsky implementation, and differences in mean velocity and Reynolds stress distributions were found to be small. More recently, Sarlak *et al.* [88] investigated the role of several subgrid-scale models in their study of wind turbine wake interactions and concluded that for highly resolved case, subgrid-scale models have only a minor impact on the flow statistics compared to the effects of the rotor resolution. However, they also showed that the contribution of the SGS model increased in coarse-grid simulations.

2.1.2 Actuator-disk model

Actuator-disk models add the axial forces exerted by the wind turbines on the flow to the Navier–Stokes equations. Tangential forces are usually neglected (given the tip-speed ratios at which turbines are operated, they are more than an order of magnitude smaller). In a validation study, comparing ADMs with and without tangential forces [108], it was demonstrated that standard ADMs provide an accurate representation of the overall wake structures behind turbines except for the very near wake ($x/D < 3$). Moreover, Reynolds stresses were also found to be accurately predicted, thus yielding a good representation of the interaction of the wind farms with the boundary layer. Later this was further corroborated by Meyers & Meneveau [72] in a detailed analysis of energy fluxes in wind farms, comparing models with and without tangential forces. In the current dissertation, a standard ADM is employed. It corresponds to the version used by [70, 16, 72], and is briefly reviewed below.

The axial force of a turbine i ($= 1 \cdots N_t$) on the flow field can be expressed as

$$F_i = -\frac{1}{2} C'_{T,i} \rho \widehat{V}_i^2 A, \tag{2.6}$$

where $C'_{T,i}$ is the disk-based thrust coefficient, $\widehat{V}_i$ is the average axial flow velocity at the turbine rotor disk (see further below), and $A = \pi D^2/4$ is the rotor-disk surface area. The disk-based thrust coefficient $C'_{T,i}$ results from integrating lift and drag coefficients over the turbine blades, taking design geometry and flow angles into account (cf. Appendix A for a detailed formulation). For an ideal design, and in the absence of any drag forces, $C'_{T,i} = 2$. Moreover, below the rated wind speed, conventional turbines use generator torque control to keep the turbine at a constant optimal tip-speed ratio independent of wind speed, while the blade pitch is kept constant at its

optimal design value. In an ADM, this corresponds to using a constant value for $C'_{T,i}$ (see also Eq. (A.5) in Appendix A).

In an ideal turbine design, the force F_i is uniformly distributed over the disk area. Therefore, in an actuator disk model, a uniform force (per unit mass) is distributed over the LES grid cells in the vicinity of the actuator disk using [70, 16, 72]

$$\boldsymbol{f}^{(i)} = -\frac{1}{2} C'_{T,i} \widehat{V}_i^2 \mathscr{R}_i(\boldsymbol{x}) \boldsymbol{e}_\perp, \tag{2.7}$$

where $\boldsymbol{e}_\perp$ represents the unit vector perpendicular to the turbine disk, and in (2.2) $\boldsymbol{f} = \sum \boldsymbol{f}^{(i)}$ is employed.

Further, $\mathscr{R}_i(\mathbf{x})$ is a geometrical smoothing function that distributes the uniform surface force of turbine i over surrounding LES grid cells. To this end, a Gaussian filter is used, leading to [70]

$$\mathscr{R}_i(\boldsymbol{x}) = \int_\Omega G(\boldsymbol{x} - \boldsymbol{x}')\, \delta[(\boldsymbol{x}' - \boldsymbol{x}_i)\cdot \boldsymbol{e}_\perp]\, \mathrm{H}(D/2 - \|\boldsymbol{y}'\|)\, \mathrm{d}\boldsymbol{x}', \tag{2.8}$$

where $G(\boldsymbol{x}) = [6/(\pi\Delta_R^2)]^{3/2} \exp\left(-6\|\mathbf{x}\|^2/\Delta_R^2\right)$ is the Gaussian filter kernel, with filter width Δ_R. Further, $\boldsymbol{x}_i$ is the coordinate of the turbine rotor center, $\delta(x)$ is the Dirac delta function, $\mathrm{H}(x)$ is the Heaviside function, and $\boldsymbol{y}' = (\boldsymbol{x}' - \boldsymbol{x}_i) - ((\boldsymbol{x}' - \boldsymbol{x}_i)\cdot \boldsymbol{e}_\perp)\boldsymbol{e}_\perp$ is the projection of $(\boldsymbol{x}' - \boldsymbol{x}_i)$ on the rotor plane. Similar to earlier studies [70, 16, 72], $\Delta_R = 3\Delta/2$ is selected, with Δ being the LES grid resolution. Finally, note that by construction, $\int_\Omega \mathscr{R}_i(\boldsymbol{x})\mathrm{d}\boldsymbol{x}' = A$.

In order to determine the axial disk-averaged velocity $\widehat{V}_i$, spatial averaging of the velocity is first performed over the rotor disk using the geometrical rotor footprint $\mathscr{R}_i(\boldsymbol{x})$, followed by a local time filter. Thus, the disk-averaged velocity is first defined as

$$V_i(t) = \frac{1}{A} \int_\Omega \widetilde{\boldsymbol{u}}(\boldsymbol{x}, t)\cdot \boldsymbol{e}_\perp\, \mathscr{R}_i(\boldsymbol{x})\, \mathrm{d}\boldsymbol{x}, \tag{2.9}$$

and $\widehat{V}_i$ is obtained from V_i using a first-order time filter, i.e.

$$\frac{\mathrm{d}\widehat{V}_i}{\mathrm{d}t} = \frac{1}{\tau}(V_i - \widehat{V}_i), \tag{2.10}$$

where τ is the filter time scale. This ordinary differential equation is discretized using an implicit Euler method, such that

$$\widehat{V}_i^n = (1-\alpha)\widehat{V}_i^{n-1} + \alpha V_i^n, \tag{2.11}$$

with $\alpha = \Delta t/(\tau + \Delta t)$.

Finally, the power that is extracted from the boundary layer by all turbines is expressed as

$$P = -\int_\Omega \boldsymbol{f}\cdot\widetilde{\boldsymbol{u}}\mathrm{d}\boldsymbol{x} = \int_\Omega \sum_{i=1}^{N_t} \frac{1}{2} C'_{T,i}\widehat{V}_i^2\, \widetilde{\boldsymbol{u}}\cdot\boldsymbol{e}_\perp\, \mathscr{R}_i(\boldsymbol{x})\,\mathrm{d}\boldsymbol{x} = \sum_{i=1}^{N_t} \frac{1}{2} C'_{T,i}\widehat{V}_i^2 V_i A. \quad (2.12)$$

This is not equivalent to the power P_{ax} that is extracted at the turbine axle, which is related to the torque and rotational velocity of the turbine. The drag forces on the turbine blade increase the thrust force, but reduce the torque. Similar to $C'_{T,i}$ a disk-based power coefficient $C'_{P,i}$ may be defined that is based on projected forces in the tangential direction. In the absence of drag, $C'_{T,i} = C'_{P,i}$ (cf. Appendix A for details).

2.1.3 Discretization scheme

Simulations are performed in SP-Wind, an in-house research code that was developed in a series of earlier studies on large-eddy simulations, wind-farm simulations, and flow optimization (see e.g. Ref. [74, 26, 70]). SP-Wind uses pseudospectral discretization in the horizontal directions. The nonlinear convective terms and the subgrid-scale stress are de-aliased using the 3/2 rule [18]. Message Passing Interface (MPI) is used to run the simulations in parallel mode, and the FFTW library is employed for Fourier transforms [33]. In the vertical direction, a fourth-order energy-conservative finite-difference discretization scheme is used (see Verstappen & Veldman [105]). The computation grid in this direction is staggered; i.e. the wall normal velocity $\widetilde{u}_3$ locations are shifted by half a cell compared to $\widetilde{u}_1, \widetilde{u}_2$ and $\widetilde{p}$. For the continuity of the system, the pressure Poisson equation is solved at every time step. The Poisson equation for the pressure can be obtained from the divergence of the momentum equation. In spectral space space, the different Fourier modes are decoupled, and the remaining third direction is solved using a direct solver based on an LU-decomposition. Finally, time integration is performed using a classical four-stage fourth-order Runge–Kutta scheme. For the simulations discussed in §2.2, the time step Δt is restricted by setting both the convective and eddy-viscosity based Courant–Friedrichs–Lewy (CFL) numbers. However, for the simulations in §2.3 and the optimal control cases (cf. Chapter 4 and Chapter 5), a fixed time step corresponding to a CFL number of approximately 0.4 is used.

2.2 Comparison between pressure-driven BL and Ekman layer

In this section the influence of an outer-layer Ekman spiral (caused by Coriolis forces) on the mean flow solution in wind farms is investigated. Furthermore, effects on the global wind-farm induced roughness $z_{0,hi}$, are also investigated. This dissertation focusses on truly neutral ABLs and show that $z_{0,hi}$ changes with ABL height (H_G) when the boundary layer becomes shallow. Additionally, a wind farm simulation is also compared with an ABL simulation in which the farm is replaced by an increased equivalent surface roughness.

2.2.1 Simulation details

The Coriolis term is added to the original momentum equation, Eq. (2.2), such that,

$$\frac{\partial \widetilde{\boldsymbol{u}}}{\partial t} + \widetilde{\boldsymbol{u}} \cdot \nabla \widetilde{\boldsymbol{u}} = -\frac{1}{\rho}\nabla \widetilde{p} - \frac{1}{\rho}\nabla p_\infty + f_c \widetilde{\boldsymbol{u}} \times \boldsymbol{e}_3 + \nabla \cdot \boldsymbol{\tau}_M + \boldsymbol{f} \tag{2.13}$$

where f_c is the Coriolis parameter. The driving pressure-gradient force $(1/\rho)\nabla p_\infty$ should balance the Coriolis force in the outer atmosphere and therefore depends upon the geostrophic velocity above the ABL, i.e.

$$\frac{1}{\rho}\frac{\partial p_\infty}{\partial x} = f_c G \sin\alpha, \qquad \text{and} \quad \frac{1}{\rho}\frac{\partial p_\infty}{\partial y} = -f_c G \cos\alpha, \tag{2.14}$$

where G is the magnitude of the geostrophic wind and α is the angle between the geostrophic wind and the wind in the surface layer.

Because of the Coriolis force, the velocity vector rotates with height above the surface. Thus, an angle exists between the geostrophic wind direction and the wind direction at the turbine hub height. This angle is not known a priori, as it depends on the total drag exerted on the boundary layer by the turbines and the ground surface. Hence, it is necessary to reorient wind turbines so that they are always perpendicular to the incoming velocity. However, doing so would alter the inter-turbine spacing, such that the geometrical arrangement pattern is not fixed a priori. To avoid this, instead the pressure gradient angle is controlled artificially during the simulations such that a desired wind direction is obtained at the turbine hub height (i.e. in the positive x-direction). To that end, a PID controller is implemented: the equation for the controller corresponds to

$$\alpha_{\text{out}} = K_p e(t) + K_i \int_0^t e(\tau)\, d\tau + K_d \frac{d}{dt} e(t), \tag{2.15}$$

Table 2.1: Simulation cases based on the Rossby number and other parameters. $L_x \times L_y \times H$: domain size, $N_x \times N_y \times N_z$: grid-resolution, N_t: number of turbines, $s_x \times s_y$: turbine spacing normalized by rotor diameter $D = 100$ m, z_0/z_h: surface roughness and hub height $z_h = D$.

Cases	G (m/s)	Ro_h	$L_x \times L_y \times H$ (km^3)	$N_x \times N_y \times N_z$	N_t	$s_x \times s_y$	z_0/z_h
1a	4	400	$6.28 \times 3.14 \times 4.0$	$128 \times 192 \times 241$	8×6	7.85×5.23	10^{-3}
1b	5	500	$6.28 \times 3.14 \times 4.0$	$128 \times 192 \times 241$	8×6	7.85×5.23	10^{-3}
1c	6	600	$6.28 \times 3.14 \times 4.0$	$128 \times 192 \times 241$	8×6	7.85×5.23	10^{-3}
1d	7	700	$6.28 \times 3.14 \times 4.0$	$128 \times 192 \times 241$	8×6	7.85×5.23	10^{-3}
1e	8	800	$6.28 \times 3.14 \times 4.0$	$128 \times 192 \times 241$	8×6	7.85×5.23	10^{-3}
1f	9	900	$6.28 \times 3.14 \times 4.5$	$128 \times 192 \times 281$	8×6	7.85×5.23	10^{-3}
1g	10	1000	$6.28 \times 3.14 \times 5.0$	$128 \times 192 \times 311$	8×6	7.85×5.23	10^{-3}
1h	11	1100	$6.28 \times 3.14 \times 5.0$	$128 \times 192 \times 311$	8×6	7.85×5.23	10^{-3}
1i	12	1200	$6.28 \times 3.14 \times 5.2$	$128 \times 192 \times 321$	8×6	7.85×5.23	10^{-3}
2	10	1000	$6.28 \times 3.14 \times 5.0$	$128 \times 192 \times 311$	6×4	10.47×7.85	10^{-3}
3	10	1000	$6.28 \times 3.14 \times 5.0$	$128 \times 192 \times 311$	11×6	5.71×5.23	10^{-3}
4	BL		$6.28 \times 3.14 \times 4.0$	$128 \times 192 \times 241$	8×6	7.85×5.23	10^{-3}
5	12	1200	$6.28 \times 3.14 \times 5.2$	$128 \times 192 \times 321$	no farm		0.0372

where α_{out} is an output angle, K_p, K_i, K_d are proportional, integral and derivative gain parameters respectively, and e stands for the error on the angle. The values for the three gain parameters are set to $K_p = 0.008$, $K_i = 2 \times 10^{-8}\,\text{sec}^{-1}$, and $K_d = 0$ sec. This controller maintains the incoming flow direction perpendicular to the rotor (as is the case in a real wind farm); additionally, it also fixes the inter-turbine spacing so that simulation results give a roughness length value for a given turbine arrangement pattern. The rest of the implementations, including the wind turbine model and the discretization schemes are the same as those discussed in §2.1.

The parameter that affects the height of the boundary layer in an Ekman spiral is the Rossby number

$$Ro_h = \frac{G}{f_c z_h}, \tag{2.16}$$

defined here based on the hub height of the wind turbines. A set of simulations is performed in which the wind-farm arrangement are kept fixed, but different Rossby numbers between 400 and 1200 are used. In addition, simulations with different geometrical arrangements are performed, keeping $Ro_h = 1000$. Since the height of the boundary-layer depends on Ro_h, domain heights are adapted such that they are at least 1.5 times the expected boundary layer height. Domain sizes in streamwise and spanwise directions are kept constant. Full details of the simulation cases are provided in Table 2.1. Note that Case 4 (BL) is a classical pressure-driven wind-farm boundary layer without the Coriolis forces.

2.2.2 Velocity profiles and roughness length

Before presenting the velocity profiles and wind-farm induced roughness length, first some concepts related to wind-farm boundary layers with wind turbines situated in the inner layer are introduced. In such boundary layers, a double log layer is observed [32, 16], one below the turbine level, characterized by the friction velocity $u_{\tau l} = (\tau_w/\rho)^{1/2}$, and the other above the turbine level, characterized by the total friction induced by the ground surface and the turbines; thus with friction velocity [16]

$$u_{\tau h}^2 = u_{\tau l}^2 + \frac{1}{N_t} \sum \frac{1}{2} \rho \widehat{V}_i^2 \frac{C'_{T,i} A}{S_x S_y}, \tag{2.17}$$

with $A = \pi D^2/4$ being the turbine rotor area.

Figure 2.2 shows the x- and y-components of the mean velocity profiles for cases 1a – 1i. In these different simulations, the geostrophic wind speed ranges

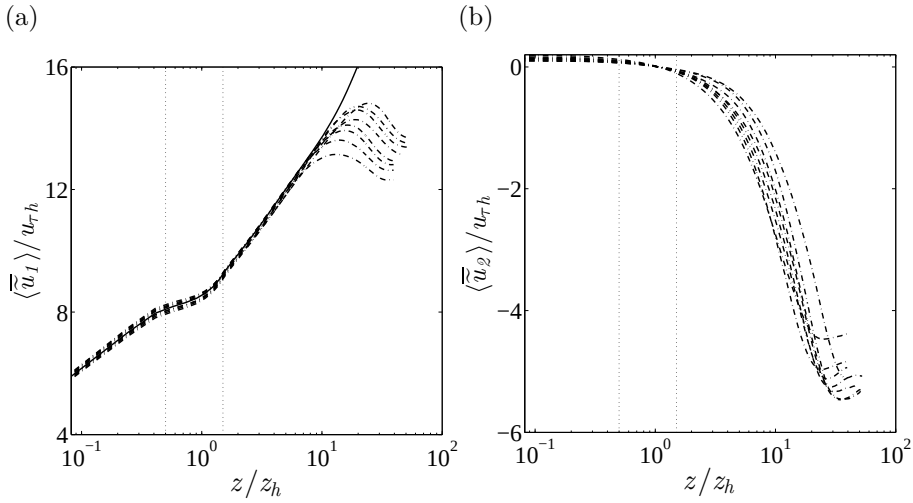

Figure 2.2: Mean velocity profiles (a) Streamwise component, (b) spanwise component. (- · - · -, dot-dashed): Ekman layer(cases 1a – 1i), (——, black): classical pressure-driven boundary layer (case 4)

from $G = 4$ to $G = 12$ (cf. Table 2.1). The velocities are normalized with the total friction velocity $u_{\tau h}$ above the farm. Looking at figure 2.2(a), it is observed that the $\langle\widetilde{\overline{u}}_1\rangle$-velocity is higher around $z/z_h \approx 20$ than above the boundary layer. This is typical for an Ekman layer; remember that the direction of the geostrophic wind is not parallel to the wind direction at turbine hub height, which is parallel to the x-direction. Similar to the observations by Calaf *et al.* [16], the streamwise velocity profile displays three regions around the turbines: (i) below the turbine disk, (ii) at the disc and (iii) above the turbine. Next to the results obtained using Coriolis forcing of the simulations, the result of a pressure-driven boundary layer flow (case 4) is also shown in figure 2.2(a). It is appreciated that below $z/z_h = 10$, this pressure-driven velocity profile collapses remarkably well with the results using the Coriolis force.

Following Calaf *et al.* [16], the roughness length induced by the wind farm for different simulations is estimated. To that end, the surface roughness $z_{0,hi}$ associated with the logarithmic velocity profile above the turbines is identified. This logarithmic profile is given by

$$\langle\widetilde{\overline{u}}_1\rangle(z) = \frac{u_{\tau h}}{\kappa} \ln\left(\frac{z}{z_{0,hi}}\right), \tag{2.18}$$

$$u_{\tau h}^2 = \int_0^{H_G} f_c(u_2 - Gsin\alpha)dz, \tag{2.19}$$

where the second relation is simply a result of integrating the x-momentum balance over the height of the boundary layer H_G. In Eq. (2.19), the term on the right hand side is the difference between the driving pressure gradient and the Coriolis force. To obtain the surface roughness, a point $z = 2z_h$ is chosen, and the velocity value is substituted into these equations to estimate $z_{0,hi}$.

In figure 2.3(a), results are shown for cases 1a – 1i, i.e. all cases with the same turbine arrangement pattern, but different geostrophic wind speeds, and corresponding Rossby numbers. As a point of reference, the value obtained by Calaf *et al.*'s analytical model for the wind-farm induced surface roughness is also displayed. This model corresponds to

$$\frac{z_{0,hi}}{z_h} = \left(1 + \frac{D}{2z_h}\right)^{\frac{\nu_w^*}{(1+\nu_w^*)}} \exp\left(-\left[\frac{c_{ft}}{2\kappa^2} + \left(\ln\left[\frac{z_h}{z_0}\left(1 - \frac{D}{2z_h}\right)^{\frac{\nu_w^*}{(1+\nu_w^*)}}\right]\right)^{-2}\right]^{-1/2}\right), \tag{2.20}$$

where $\nu_w^* \approx 28\sqrt{1/2c_{ft}}$ and $c_{ft} = \pi C_T/4s_x s_y$. For further details regarding the parameters and the derivation of Eq. (2.20), the reader is referred to Calaf, Meneveau & Meyers [16]. It is appreciated that this model does not display any Rossby-number dependence, as it is developed under the assumption that the outer-layer dynamics of the boundary layer do not affect the inner-layer behavior characterized by the induced surface roughness. Thus, in figure 2.3(a), Eq. (2.20) corresponds to a constant value.

It can be observed in figure 2.3(a) that for high Rossby numbers (i.e. when the ABL height is large), the surface roughness $z_{0,hi}$ is almost constant, with a value $z_{0,hi}/z_h \approx 0.037$ for the current wind-farm lay-out. In this case, the turbines are situated well inside the inner layer of the boundary layer ($< 0.1H_G$), and thus, the classical hypothesis that inner-layer dynamics are separated in scale from outer-layer effects may be justified, such that the global effect of the wind-farm on the outer layer can be lumped into one parameter, i.e. the surface roughness $z_{0,hi}$, that is further independent of the Rossby number or the ABL height.

For lower Rossby numbers ($Ro_h < 700$), it is observed that $z_{0,hi}$ is no longer constant, but gradually decreases with Ro_h. However, even at the lowest

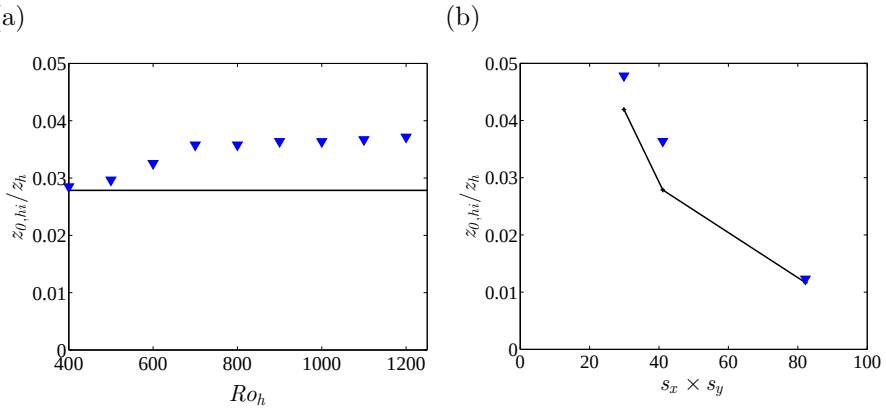

Figure 2.3: Comparison between the roughness height from the LES results and the model predicted value. (a) Function of Ro_h, (b) for different turbine spacings. (▼): from simulations, (—, line): model of Calaf *et al.* [16]

value $Ro_h = 400$, the truly neutral boundary layer is still rather thick, with $H_G/z_h = 18$. In reality, neutral atmospheric boundary layers are so-called 'conventionally neutral', i.e. in these ABLs, stable atmospheric stratification above the boundary layer damps the maximum thickness that the boundary layer can attain [1]. Hence, in these cases, the dependence of $z_{0,hi}$ on boundary layer height may be even more prominent.

In figure 2.3(b), results are shown for cases 1g, 2, and 3 (cf. Table 2.1), i.e. all with geostrophic wind $G = 10$, and $Ro_h = 1000$, but with different turbine spacings. The model of Calaf, Meneveau & Meyers is also displayed, and it is appreciated that the trends are well followed by this model, though it underpredicts the induced surface roughness at smaller turbine spacings.

Finally, an additional numerical experiment is performed to evaluate how well the surface roughness $z_{0,hi}$ characterizes the wind-farm boundary layer flow. Therefore, the wind turbine forces are removed from the domain, and instead replaced with a stress-boundary condition with surface roughness $z_{0,hi}$ (case 5). Figure 2.4 compares this simulation to a case with a wind farm. It is appreciated from this figure that the profile with surface roughness agrees well with the wind-farm simulation case and especially with its logarithmic fit. This agreement justifies the replacement of a wind-farm by its characteristic roughness length as a surface stress in large scale simulations such as regional climate models. In such simulations it is not feasible to simulate whole wind-farm canopies [6, 106].

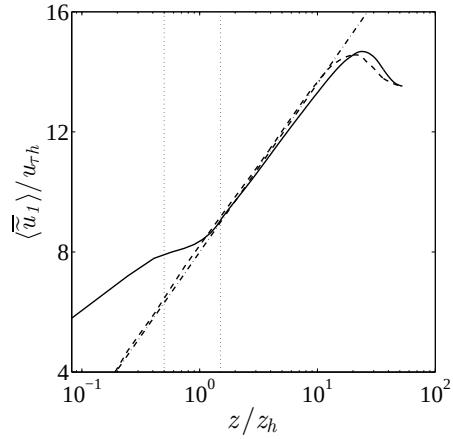

Figure 2.4: Comparison of profile for wind-farm simulation with that of the simulation in which farm is replaced by equivalent roughness length. (——, black): Wind-farm ABL, (- - -, dashed): with equivalent roughness, (- · - · -, dot-dashed): log law approximation.

2.2.3 Discussion

The dependency of the wind-farm induced surface roughness $z_{0,hi}$ on the Rossby number and boundary layer depth is determined. As observed in figure 2.3, when the boundary layer is shallow, outer-layer effects may become important at the level of the wind farm. For the particular turbine arrangement pattern used in the current simulations, it is observed that $z_{0,hi}$ is constant for $Ro_h \geq 700$. At lower values, $z_{0,hi}$ starts to decrease slightly with the Rossby number. However, the simulations in the current study correspond to what is often called a 'truly' neutral boundary layer. In reality, atmospheric stratification above the boundary layer inhibits boundary-layer growth, such that the depth of such a 'conventionally' neutral boundary layer is significantly lower (typically <1000m). Current results suggest that for such situations, outer-layer dynamics may have an important effect on the mean-flow distribution at the wind-turbine level. However, further investigations which also include the boundary layer stratification will be important to understand the mechanism.

It can be observed in figure 2.2(a) that the streamwise velocity profile for the pressure-driven boundary layer shows a remarkable agreement with the Ekman layer profile for $z/z_h \leq 10$. For the rest of this dissertation, the Coriolis force is not included in the momentum equation and only a thermally neutral pressure-driven boundary layer is considered(cf. Eq. (2.2)).

Table 2.2: Summary of the simulation set-up and the turbine arrangement parameters.

Domain size	$L_x \times L_y \times H = 7 \times 3 \times 1$ km^3
Driving pressure gradient[1]	$f_\infty = 10^{-3}$ m/s^2
Turbine dimensions	$D = 0.1H = 100$ m, $z_h = 0.1H = 100$ m
Turbine arrangement	10×5
Turbine spacing	$S_\mathrm{x} = 7D$, and $S_\mathrm{y} = 6D$
Surface roughness	$z_0 = 10^{-4}H = 0.1$m
Grid size	$N_x \times N_y \times N_z = 256 \times 192 \times 80$
Cell size	$\Delta_x \times \Delta_y \times \Delta_z = 27.3 \times 15.6 \times 12.5$ m^3
Time step	0.7 s

[1] Divided by density ρ

2.3 Boundary-layer response and optimal energy extraction using standard turbine control

In the current subsection, the response of a wind-farm boundary layer to static changes in C_T' is studied. This will help in defining a reference case, as well as a starting point for the dynamic optimization in Chapter 4.

2.3.1 Case setup

The focus is on the simulation and optimal control of an aligned wind farm, i.e. turbines are aligned in rows that are parallel to the wind direction. Details of the case set-up are summarized in Table 2.2 using typical orders of magnitude that are relevant for a wind farm. A boundary layer height corresponds to H =1km, and a domain size is $L_x \times L_y \times H = 7 \times 3 \times 1$ km^3. Fifty turbines with diameter $D = 100$m are arranged in a 10 by 5 matrix, with streamwise spacing $S_\mathrm{x} = 7D$, and spanwise spacing $S_\mathrm{y} = 6D$. As routinely done, the set-up can also be non-dimensionalized with the turbine hub height or boundary-layer height, and with the friction velocity $(f_\infty H)^{1/2}$ (= 1m/s here). The computational grid corresponds to $N_x \times N_y \times N_z = 256 \times 192 \times 80$. For dealiasing, this is extended to $384 \times 288 \times 80$ for all operations in real space.

The resulting case resembles earlier aligned wind-farm simulations (cf. Case A3 in [16], and Case 1 in [72]) but with slightly altered wind-farm parameters, so that the turbine spacings are integer multiples of the rotor diameter, while the ground surface per turbine are roughly the same ($S_x \times S_y = 7.85D \times 5.23D$ in the earlier studies, with 8×6 turbines). Furthermore, a slightly finer mesh spacing is used in the current dissertation. The reader is referred to Calaf *et al.* [16] and Meyers & Meneveau [72] for effects of domain size, and grid-refinement studies.

The simulations discussed in this section are first started from an initial logarithmic velocity profile to which a set of random perturbations are added. After an initial spin-up period of 16 hours (corresponding to approximately 85 through-flow times) during which the velocity profile and turbulence statistics evolve into a statistical equilibrium, averaged flow properties are accumulated for a time window of 21 hours. Subsequent simulations (for parameter variations, i.e. different C_T' setting) start from an earlier statistically stationary field, and use a spin-up period of 6 hours (30 through-flow times).

In figure 2.5, a snapshot of the instantaneous velocity field is shown. In the horizontal plane, the typical meandering of the turbine wakes can be observed. At the same time, patches of high speed wind can also be seen passing through the spaces between turbine columns.

2.3.2 Mean power output

When considering a single turbine in idealized conditions, the optimal operating condition of the turbine corresponds to $C_T' = 2$ (cf. Appendix A), corresponding to the Betz limit. However, in an infinite wind-farm boundary layer, the boundary layer responds to the surface roughness induced by the wind farm, and the wind velocity at the turbine hub height depends on parameters such as the turbine spacing and the thrust coefficient. Therefore, when comparing different control cases, it is important to normalize the total power extraction of the farm P by a correct reference value that itself is not dependent on the control and remains constant in real conditions. The logical reference to use for a wind farm in the atmospheric boundary layer is the geostrophic wind G in the free atmosphere above the ABL. This approach was, e.g. followed by Meyers & Meneveau [71] when investigating optimal turbine spacing for large wind farms, thus optimizing $P_{ABL}^+ = P/G^3$.

An issue is that the boundary layer considered in the current study is a regular pressure-driven boundary layer. However, it is possible to use the main working hypothesis that the wind turbines are in the inner layer of the boundary layer (cf. discussion in the introduction), and thus, their overall effect on the outer

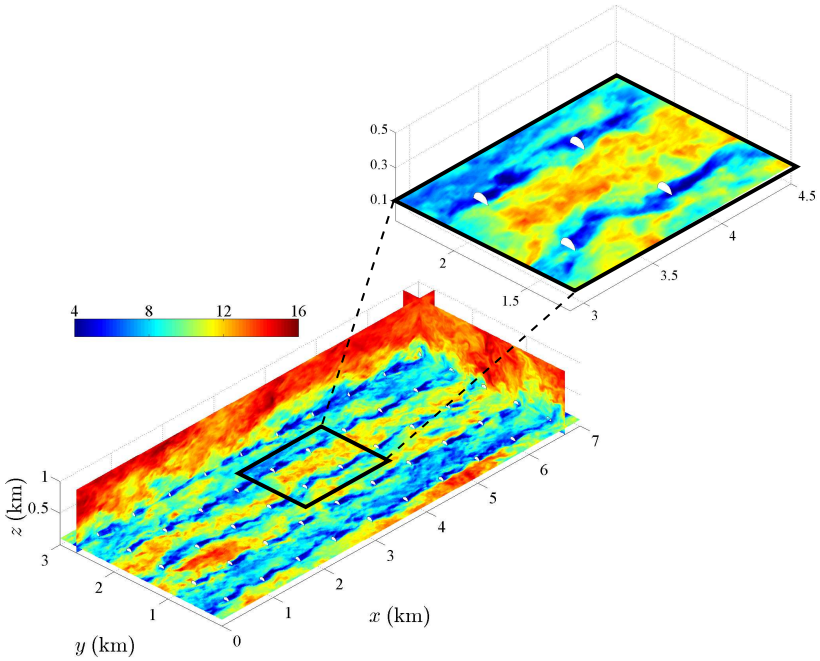

Figure 2.5: Snapshot representing an instantaneous streamwise velocity field and zoom on a subset of four turbines. The horizontal plane in the figure is taken at the hub height, and the turbines are represented by small white disks.

layer is characterized by the friction velocity $u_{\tau h}$. It should be noted that, in a pressure-driven boundary layer, integration of the momentum balance over the full height of the boundary layer yields $u_{\tau h}^2 = f_\infty H$. By further using basic momentum and energy conservation laws for an Ekman spiral, it is then possible to obtain a simple heuristic relation between $u_{\tau h}$ and G, i.e. (cf. Appendix B)

$$G = u_{\tau h}\sqrt{A^2 + \left(\frac{\mathscr{D}+\mathscr{P}}{u_{\tau h}^3}\right)^2}, \tag{2.21}$$

where $\mathscr{D}$ is the total turbulent dissipation per unit wind-farm area, and $\mathscr{P}$ is the average turbine power extraction per unit farm area (i.e. $\mathscr{P} = \overline{P}/(L_x L_y)$, with $\overline{P}$ being the time average of P). Furthermore, $A \approx 12$ is an empirical constant that depends on the outer-layer behavior of the ABL.

The response of the boundary layer to changes in C_T' is now investigated. Note that the optimal coordinated control of C_T' at the farm level is not considered yet, but instead C_T' is kept constant in time, and the same for all turbines.

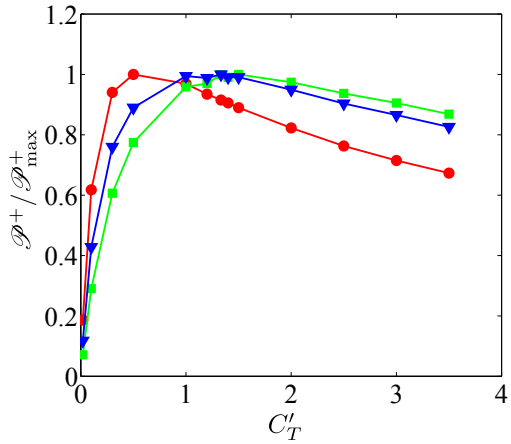

Figure 2.6: Mean power output of uncontrolled wind farm as function of C'_T. Power $\mathscr{P}^+$ is normalized by either $u_{\tau h}$ (●), geostrophic wind G (■), or driving power (▼). Curves are further normalized by their maximum values of $\mathscr{P}^+$.

Thirteen different cases are considered, with $0.02 \leq C'_T \leq 3.5$. Results for the averaged total power extraction are shown in figure 2.6. Two normalizations are shown, i.e. one using $\mathscr{P}^+_{PBL} = \mathscr{P}/u^3_{\tau h}$, which is the standard normalization for a Pressure-driven Boundary Layer (PBL), and the other using $\mathscr{P}^+_{ABL} = \mathscr{P}/G^3$, as relevant for ABLs. For the second normalization, Eq. (2.21) is used to determine $u_{\tau h}/G$. These two normalizations reflect the different reactions of a PBL and an ABL to a changing load. In figure 2.6, it is appreciated that the extracted power depends strongly on the disk-based thrust coefficient. Furthermore, the selected normalization leads to quite different optimal values for C'_T: using the maximum of $\mathscr{P}/u^3_{\tau h}$ leads to much lower optimal C'_T values than when using $\mathscr{P}^+_{ABL} = \mathscr{P}/G^3$. Thus, presuming a constant pressure gradient, independent from the wind-farm load, does not lead to the same optimum as when presuming a constant geostrophic wind.

Figure 2.6 also shows a third normalization that is based on the total driving power of the PBL, i.e. $\mathscr{P}^+_{DRP} = \mathscr{P}/(f_\infty U_b H)$, with U_b being the total bulk velocity. Thus, such a normalization presumes a constant driving power in the boundary layer that is independent of the wind-farm load. It is observed that this third normalization leads to an optimal C'_T value that is close to the one found for $\mathscr{P}/G^3$, with $C'_T \approx 1.33$.

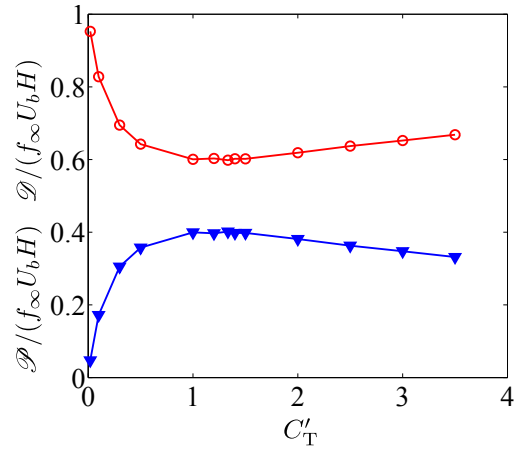

Figure 2.7: Mean power output (▼) and dissipation (○) as functions of C'_T for uncoordinated cases. Both power and dissipation are normalized by the driving power.

2.3.3 Discussion

As observed in figure 2.6, the optimal setting of C'_T and the maximum normalized wind-farm power output depend much on the impedance of the driving force. The logical approach for wind farms is to use $\mathscr{P}^+_{ABL} = \mathscr{P}/G^3$ to determine the maximum power that can be extracted from an 'uncontrolled' wind farm with static C'_T values. This maximal power can serve as a logical reference that optimal control (cf. Chapter 4) should improve upon. However, results for $\mathscr{P}_{ABL}$ in figure 2.6 are based on a heuristic relation for the ABL response (2.21). For instance, the empirical constant A (cf. Eq. (B.8)) may itself depend in subtle ways on the wind-farm loading, etc. Also, the evaluation of $\mathscr{D}$ in Eq. (2.21) requires the integration of the total dissipation in the inner as well as the outer layer. The latter is not the same in PBLs and ABLs.

In order to avoid these issues, and to keep the approach internally consistent with the idea of a pressure-driven boundary layer, for the 'uncontrolled' reference in this dissertation the case with a constant driving power that maximizes $\mathscr{P}^+_{DRP}$, i.e. with $C'_T \approx 1.33$, is chosen. As observed in figure 2.6, this maximum is close to that for $\mathscr{P}^+_{ABL}$. Moreover, the physical interpretation as to how gains in power extraction are achieved is straightforward. In a statistically stationary system, the energy balance can be expressed as

$$f_\infty U_b H = \mathscr{P} + \mathscr{D}. \tag{2.22}$$

Here, $f_\infty U_b H$ is the total driving power per unit farm area. Thus, given a constant total driving power in a PBL, the only way that the wind-farm output may be increased is by increasing the ratio $\mathscr{P}/\mathscr{D}$, and reducing the turbulent dissipation. In figure 2.7, $\mathscr{P}/(f_\infty U_b H)$ and $\mathscr{D}/(f_\infty U_b H)$ are shown as functions of C_T'. For the current wind farm and turbine arrangement, it is observed that at the optimal point $C_T' = 1.33$, only 40% of the total power input is actually harvested by the wind farm, while 60% is dissipated by turbulence.

Finally, the power optimization in a real ABL may involve more than only improving the ratio of wind-farm energy extraction to turbulent dissipation. In particular, the entrainment at the top of the boundary layer may play an important role in the total power that is available. For boundary layers that are thick compared to the size of the wind turbines, the entrainment can be expected to be a secondary effect. However, for boundary layers that are shallow, or for internal boundary layers developing over finite wind farms, entrainment will play an important role in the total power available, and may be strongly influenced by the wind-farm itself.

Chapter 3

Optimal coordinated control: formulation and methodology

This chapter presents the optimization approach used in this dissertation. The optimal control problem is introduced along with the mathematical formulation of the gradient and adjoint-based optimization method. The key to the formulation of an optimization problem is the correct definition of the cost functional which should be minimized to satisfy a certain control objective. The cost functional for the present wind-farm boundary layer control is rather straightforward, and includes the total energy extraction of the farm. In the current optimal control problem, the disk-based thrust coefficients are dynamically changed as a function of time and per turbine in the farm, and are optimized to increase the overall energy extraction. Thus, the actual generator torque and blade pitch control actions that would in reality determine the disk-based thrust coefficient are not directly included in the optimal control model. It is presumed that these actions are performed sufficiently fast for the required dynamical changes in the thrust coefficient in the optimal control. As further shown in Chapter 4, these dynamic changes occur over time scales that are larger than 10 seconds, so this is a reasonable approximation.

Section 3.1 discusses a receding-horizon control approach employed in the current setting. In this approach, the control problem is split into a number of optimal control sub-problems. The formulation of these sub-problems is subsequently introduced in Section 3.2 followed by optimization method in Section 3.3. A gradient-based approach and the determination of the gradients based on an adjoint approach is elaborated in Section 3.4. Adjoint equations are derived in Section 3.5. In Section 3.6, the implementations of the adjoint

equations are verified by comparing the adjoint-based gradients with those obtained from a classical finite difference approach.

3.1 Receding-horizon approach

A receding-horizon optimal control approach is employed for the control of wind-farm boundary layer interaction. This essentially follows the standard paradigm of model-predictive control [86], but where the model in this case consists of the full LES equations Eq. (2.1,2.2), and where there is no problem regarding the state estimation, i.e. in these simulations, the flow state is perfectly known at each time step. In the context of DNS-based and LES-based optimal control, a similar setting was employed by Bewley *et al.* [10], and Chang & Collis [21].

In a receding-horizon optimal control approach, time is split into a number of control windows of length T, also called the time horizon – a schematic overview is presented in figure 3.1(a). Starting with the first time horizon, an optimization problem is formulated (cf. Section 3.2) in which the control parameters are optimized as a function of time. To that end, an iterative, gradient-based optimization approach is used (cf. Section 3.3) requiring several large-eddy simulations, combined with adjoint simulations for the determination of the gradients (cf. Section 3.4 and 3.5). Once a set of optimal controls is found for the interval $[0, T]$, they are effectively used as control inputs to advance the system over a time window T_A (see figure 3.1). Subsequently, a new optimization problem is formulated that optimizes the controls for the time window $[T_A, T_A+T]$, and so forth. An example of how control (disk-based thrust coefficient) evolves in the receding-horizon approach is shown in figure 3.1(b) for the first three consecutive control windows. It can be appreciated that the C_T' changes dynamically in response to the flow.

In standard receding-horizon optimal control, T_A often just corresponds to the control time step, so that with every time step a control optimization problem is solved, leading to an optimization time horizon that smoothly moves forward with the control inputs. In the context of DNS-based or LES-based optimal control, this is not done, as every optimization problem itself requires very large computational resources. Bewley *et al.* [10] used $T_A = T$ to limit computational cost, although this led to non-smooth transitions between time windows. They also looked at one case with $T_A = T/2$, and in a similar study, Collis *et al.* [25] also explored $T_A = 3T/4$, and $T_A = T/4$. In the current work, $T_A = T/2$ is chosen as an ad-hoc balance between computational cost

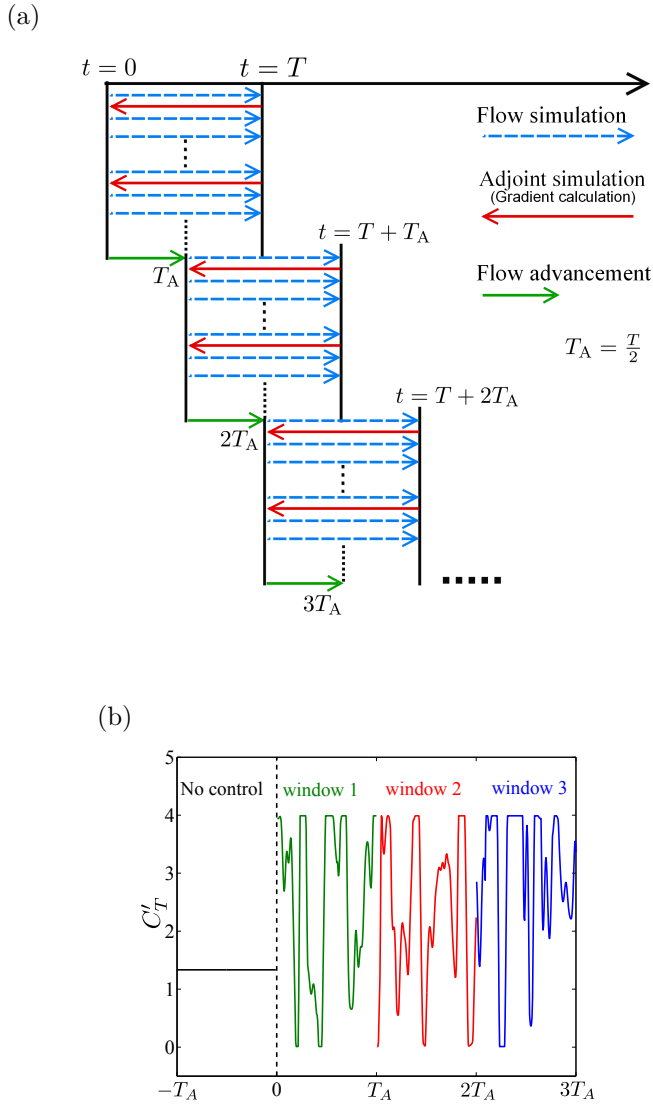

Figure 3.1: (a) Schematic of receding-horizon optimal control approach. (b) An example of the evolution of control in the present receding-horizon approach.

and control smoothness, and time windows of length T_A are referred to as the control windows.

3.2 Optimization problem formulation

The control parameters correspond to all disk-based turbine thrust coefficients $\boldsymbol{\varphi} \equiv [C'_{T,1}(t), C'_{T,2}(t), \cdots, C'_{T,N_t}(t)]$ (with N_t being the total number of turbines). The state variables in the optimal control problem are $\boldsymbol{q} \equiv [\widetilde{\boldsymbol{u}}(\boldsymbol{x},t), \widetilde{p}(\boldsymbol{x},t), \widehat{\boldsymbol{V}}(t)]$, i.e. corresponding to the LES velocity field, pressure field, and the time-filtered turbine-disk velocity fields $\widehat{\boldsymbol{V}} \equiv [\widehat{V}_1, \cdots, \widehat{V}_{N_t}]$.

The optimal control problem is formulated as a minimization problem in which the two different cost functionals $\mathscr{J}(\boldsymbol{\varphi}, \boldsymbol{q})$ below are employed:

$$\mathscr{J}_1(\boldsymbol{\varphi}, \boldsymbol{q}) = \int_0^T -P(t)\,\mathrm{d}t \tag{3.1}$$

$$\mathscr{J}_2(\boldsymbol{\varphi}, \boldsymbol{q}) = (1-\gamma)\int_0^T -P(t)\,\mathrm{d}t + \gamma \mathscr{D}_\Omega L_x L_y. \tag{3.2}$$

Here,

$$\int_0^T P(t)\,\mathrm{d}t = \int_0^T \int_\Omega \sum_{i=1}^{N_t} \frac{1}{2} C'_{\mathrm{T,i}} \widehat{V}_i^2\, \mathscr{R}_i(\boldsymbol{x}) \widetilde{\boldsymbol{u}}(\boldsymbol{x},t) \cdot \boldsymbol{e}_\perp \,\mathrm{d}\boldsymbol{x}\,\mathrm{d}t, \tag{3.3}$$

corresponds to the amount of energy extracted from the boundary layer by the wind turbines over the optimization time horizon T. The current dissertation focusses on increasing P by controlling $C'_{T,i}$, and does not explicitly take $C'_{P,i}$ into account. It is presumed that $C'_{T,i}/C'_{P,i}$ is roughly constant, so that the power extracted from the boundary layer is representative of the mechanical power at the turbine axle. Such an approximation does not take into account deleterious effects that increased turbulence levels may have on local blade lift and drag coefficients, in particular as a result of increased occurrences of stall. However, as further shown in Chapter 4, turbulence levels do not increase in front of the turbines in the considered optimal control cases, so that above working assumption is reasonable. A more involved representation that more accurately models the effect of turbulence levels on blade performance is a subject for further research (see also the discussion in Chapter 6).

The second terms in Eq. (3.2) is penalization terms based on the total dissipation $\mathscr{D}_\Omega L_x L_y$. Thus, $\gamma > 0$ leads to an optimization problem that

penalizes $\mathscr{D}_\Omega$. Moreover, it is required that $\gamma < 1$, as $\gamma = 1$ leads to a cost functional that reduces dissipation but no longer has any impact on wind-farm energy extraction, while $\gamma > 1$ starts penalizing wind-farm energy extraction. The optimization results for the cost functional with the penalty term i.e. $\mathscr{J}_2$, are presented in Section 4.3. Unpenalized cases, i.e. those with the $\mathscr{J}_1$ cost functional, are discussed in Section 4.2 as well as in Chapter 5 for the optimal control of a finite farm.

The optimal control problem under consideration is a PDE-constrained optimization problem that corresponds to

$$\min_{\boldsymbol{\varphi},\boldsymbol{q}} \quad \mathscr{J}(\boldsymbol{\varphi},\boldsymbol{q}) \tag{3.4}$$

s.t.

$$\begin{cases} \dfrac{\partial \widetilde{\boldsymbol{u}}}{\partial t} + \widetilde{\boldsymbol{u}} \cdot \nabla \widetilde{\boldsymbol{u}} = & -\dfrac{1}{\rho}\nabla \widetilde{p} + f_\infty \boldsymbol{e}_1 + \nabla \cdot \boldsymbol{\tau}_M \\ & + \boldsymbol{f} + \delta(\boldsymbol{x} - z_1 \boldsymbol{e}_3)\boldsymbol{\tau}_{\boldsymbol{w}} \end{cases} \quad \text{in } \Omega \times (0,T] \\ \nabla \cdot \widetilde{\boldsymbol{u}} = 0 \quad \text{in } \Omega \times (0,T] \\ \dfrac{\mathrm{d}\widehat{\boldsymbol{V}}}{\mathrm{d}t} = \dfrac{1}{\tau}(\boldsymbol{V} - \widehat{\boldsymbol{V}}) \quad \text{in } (0,T] \end{cases} \tag{3.5}$$

In (3.5), the wall-stress model is explicitly added to the momentum equation using the Dirac delta function $\delta(\boldsymbol{x} - z_1\boldsymbol{e}_3)$ with z_1 being the location of the first grid point near the wall, and where $\boldsymbol{\tau}_{\boldsymbol{w}} = [\tau_{w1}, \tau_{w2}, 0]$, with τ_{w1} and τ_{w2} defined by Eq. (2.3, 2.4). For the sake of further use, the state constraints (3.5) are written in short-hand notation as $\boldsymbol{B}(\boldsymbol{\varphi},\boldsymbol{q}) = 0$, representing LES momentum and continuity equations, and the time filter of the disk velocity.

Finally, note that some additional box constraints on the controls, i.e. $0 \leq C'_{T,i}(t) \leq 4$, are added. These are trivial to add, and are not formally included here to not further complicate the equations. See Section 4.1 for further discussion on these constraints.

3.3 Optimization method

In this dissertation, the PDE-constrained optimization problem is not solved in its standard form as written in Eq. (3.4) and (3.5) where the PDE is explicitly formulated as a constraint. Although it is possible and sometimes beneficial to do this for smaller problems (see e.g. Hinze & Kunisch [46], for a discussion), the size of the space–time state space in the present optimal control problem (order of 1 billion degrees of freedom) does not allow such an approach. Instead,

the problem is reformulated in a reduced form, with a reduced cost functional, i.e.

$$\min_{\boldsymbol{\varphi}} \tilde{\mathscr{J}}(\boldsymbol{\varphi}) \equiv \mathscr{J}(\boldsymbol{\varphi}, \boldsymbol{q}(\boldsymbol{\varphi})), \tag{3.6}$$

where $\boldsymbol{q}(\boldsymbol{\varphi})$ is the solution to the state equations given the control inputs $\boldsymbol{\varphi}$, implicitly defined by $\boldsymbol{B}(\boldsymbol{\varphi}, \boldsymbol{q}(\boldsymbol{\varphi})) \equiv 0$. Thus, in its reduced form the problem is unconstrained, but at every step of the optimization algorithm the state constraints need to be explicitly satisfied. The size of the optimization space in this reduced formulation corresponds to the number of degrees of freedom of $\boldsymbol{\varphi}$, which is approximately 2×10^4 in this study.

To solve Eq. (3.6), the same approach is followed as first used by Bewley *et al.* [10] for DNS-based optimal control, i.e. the combination of a Polak–Ribière conjugate-gradient method and the Brent line-search algorithm [84, 65, 79]. It is an iterative method for solving unconstrained optimization problems. Given an intermediate estimate of the optimum $\boldsymbol{\varphi}^{(k)}$, a search direction $\delta\boldsymbol{\varphi}^{(k)}$ is determined using the Polak–Ribière conjugate-gradient direction

$$\delta\boldsymbol{\varphi}^{(k)} = -\nabla\tilde{\mathscr{J}}^{(k)} + \beta_k \delta\boldsymbol{\varphi}^{(k-1)}, \tag{3.7}$$

where $\nabla\tilde{\mathscr{J}}^{(k)}$ is the gradient of the cost functional (cf. Section 3.5 for its determination based on the adjoint equations), and β_k is given by

$$\beta_k = \frac{\left(\nabla\tilde{\mathscr{J}}^{(k)} - \nabla\tilde{\mathscr{J}}^{(k-1)}\right) \cdot \nabla\tilde{\mathscr{J}}^{(k)}}{\nabla\tilde{\mathscr{J}}^{(k-1)} \cdot \nabla\tilde{\mathscr{J}}^{(k-1)}}. \tag{3.8}$$

Using the search direction $\delta\boldsymbol{\varphi}^{(k)}$, a new estimate of the optimum is obtained from

$$\boldsymbol{\varphi}^{(k+1)} = \boldsymbol{\varphi}^{(k)} + \alpha\, \delta\boldsymbol{\varphi}^{(k)}, \tag{3.9}$$

where α is the result of a line search that minimizes $\tilde{\mathscr{J}}(\boldsymbol{\varphi}^{(k)})$ in the direction $\delta\boldsymbol{\varphi}^{(k)}$. To that end, an iterative gradient-free line-search method is used that is based on the *mnbrak* and Brent algorithms [84]. Details on the implementation used in this dissertation can be found in Delport, Baelmans & Meyers [26].

3.4 Derivation of the gradient of the reduced cost functional

An important element in the conjugate-gradient algorithm discussed above is the determination of the gradient of the reduced cost functional $\nabla\tilde{\mathscr{J}}$ for a given set of controls $\boldsymbol{\varphi}$. The use of a simple finite difference approach is not feasible if the design space $\boldsymbol{\varphi}$ is large, since this requires an evaluation of the

state equations for every possible dimension in $\boldsymbol{\varphi}$. Instead, a mathematically equivalent formulation for the determination of the gradient can be used that requires once the solution of an additional set of partial differential equations, i.e. the adjoint equations, with a cost that is roughly equivalent to that of the original state equations.

The definition of the gradient of the cost functional and the derivation of the adjoint equations that can be used for the determination of the gradient are presented next. To that end, some definitions are first introduced, i.e. a proper definition of inner products, a definition of the gradient of a functional, the linearization of the state equations and the adjoint of a linear operator.

3.4.1 Some definitions

First of all, the inner product between state variables $\boldsymbol{q}_1$ and $\boldsymbol{q}_2$ and between control variables $\boldsymbol{\varphi}_1$ and $\boldsymbol{\varphi}_2$ (all in suitable Hilbert spaces $\mathcal{H}$) are defined as

$$(\boldsymbol{q}_1, \boldsymbol{q}_2) = \int_0^T \int_\Omega \widetilde{\boldsymbol{u}}_1 \cdot \widetilde{\boldsymbol{u}}_2 \, \mathrm{d}\boldsymbol{x} \, \mathrm{d}t + \int_0^T \int_\Omega \widetilde{p}_1 \widetilde{p}_2 \, \mathrm{d}\boldsymbol{x} \, \mathrm{d}t + \int_0^T \widehat{\boldsymbol{V}}_1 \cdot \widehat{\boldsymbol{V}}_2 \, \mathrm{d}t, \quad (3.10)$$

$$(\boldsymbol{\varphi}_1, \boldsymbol{\varphi}_2) = \int_0^T \boldsymbol{\varphi}_1 \cdot \boldsymbol{\varphi}_2 \, \mathrm{d}t. \quad (3.11)$$

Using these definitions of inner products and the associated functional spaces, the gradient of a differentiable functional is now defined as the Riesz representation of its derivative (see Ref. [102, 12]). Thus, for the reduced cost functional and using the definition of the Gateau derivative in the direction $\delta\boldsymbol{\varphi}$, this leads to

$$\tilde{\mathscr{J}}_{\boldsymbol{\varphi}}(\delta\boldsymbol{\varphi}) \equiv \frac{\mathrm{d}}{\mathrm{d}\alpha} \tilde{\mathscr{J}}(\boldsymbol{\varphi} + \alpha\delta\boldsymbol{\varphi})\Big|_{\alpha=0} = (\nabla\tilde{\mathscr{J}}, \delta\boldsymbol{\varphi}) \qquad \forall \delta\boldsymbol{\varphi} \in \mathcal{H}. \quad (3.12)$$

Since the derivative is a linear functional, the Riesz representation theorem ensures that the form on the right-hand side can always be found.

The state equations $\boldsymbol{B}(\boldsymbol{\varphi}, \boldsymbol{q}) = 0$ can be linearized around $(\boldsymbol{\varphi}, \boldsymbol{q})$ in a direction $(\delta\boldsymbol{\varphi}, \delta\boldsymbol{q})$, leading to a set of linear (partial) differential equations

$$\frac{\partial \boldsymbol{B}}{\partial \boldsymbol{\varphi}} \delta\boldsymbol{\varphi} + \frac{\partial \boldsymbol{B}}{\partial \boldsymbol{q}} \delta\boldsymbol{q} = 0, \quad (3.13)$$

where $\partial\boldsymbol{B}/\partial\boldsymbol{\varphi}$ and $\partial\boldsymbol{B}/\partial\boldsymbol{q}$ are linear operators.

Finally, the adjoints of these linear operators can be defined. For the operator $\partial \boldsymbol{B}/\partial \boldsymbol{q}$, the adjoint is defined through

$$\left(\boldsymbol{q}^*, \frac{\partial \boldsymbol{B}}{\partial \boldsymbol{q}}\delta\boldsymbol{q}\right) \equiv \left(\left[\frac{\partial \boldsymbol{B}}{\partial \boldsymbol{q}}\right]^* \boldsymbol{q}^*, \delta\boldsymbol{q}\right) + BT_1, \tag{3.14}$$

where $[\partial \boldsymbol{B}/\partial \boldsymbol{q}]^*$ is typically found using integration by parts (see further below for practical derivations), and BT_1 are boundary terms that arise as a result of this. Similarly,

$$\left(\boldsymbol{\varphi}^*, \frac{\partial \boldsymbol{B}}{\partial \boldsymbol{\varphi}}\delta\boldsymbol{\varphi}\right) \equiv \left(\left[\frac{\partial \boldsymbol{B}}{\partial \boldsymbol{\varphi}}\right]^* \boldsymbol{\varphi}^*, \delta\boldsymbol{\varphi}\right) + BT_2. \tag{3.15}$$

This second identity is usually trivial. In the current work, it is easily found that $\partial \boldsymbol{B}/\partial \boldsymbol{\varphi} = [\partial \boldsymbol{B}/\partial \boldsymbol{\varphi}]^*$ and $BT_2 = 0$. Further elaboration follows in §3.4.2.

3.4.2 Gradient of the reduced cost functional

Using (3.12) and (3.6), the gradient of the reduced cost functional can be expressed as

$$\begin{aligned}(\nabla\tilde{\mathscr{J}}, \delta\boldsymbol{\varphi}) &= \left(\frac{\partial \mathscr{J}}{\partial \boldsymbol{\varphi}}, \delta\boldsymbol{\varphi}\right) + \left(\frac{\partial \mathscr{J}}{\partial \boldsymbol{q}}, \frac{\partial \boldsymbol{q}}{\partial \boldsymbol{\varphi}}\delta\boldsymbol{\varphi}\right) \\ &= \left(\frac{\partial \mathscr{J}}{\partial \boldsymbol{\varphi}}, \delta\boldsymbol{\varphi}\right) + \left(\frac{\partial \mathscr{J}}{\partial \boldsymbol{q}}, \delta\boldsymbol{q}\right).\end{aligned} \tag{3.16}$$

However, straightforwardly using this formulation leads to very expensive gradient evaluations, as $\delta\boldsymbol{q}$ requires the solution of (a linearized version of) the governing partial differential equations (i.e. given by Eq. (3.13)) for every possible direction $\delta\boldsymbol{\varphi}$ represented in the gradient. Instead, an adjoint-based approach is usually followed for the gradient calculation. This has long been established in problems related to aerodynamic design (see e.g. Ref. [82, 49]), and has also been adapted to transient Navier–Stokes simulations (see Choi *et al.* [22] and Bewley *et al.* [10], among others).

The formal Lagrangian method (see e.g. Ref. [102, 12]) is followed to formulate the gradient of the reduced cost functional $\nabla\tilde{\mathscr{J}}$ in an adjoint formulation. To this end, the Lagrangian associated with the problem formulation used in Eq. (3.4) and (3.5) is introduced first. Introducing a set of Lagrange multipliers $\boldsymbol{q}^* = (\boldsymbol{\xi}, \pi, \boldsymbol{\chi})$ for each state constraint, with state variables $\boldsymbol{q} = (\widetilde{\boldsymbol{u}}, \widetilde{p}, \widehat{\boldsymbol{V}})$, this

leads to

$$\mathscr{L}(\boldsymbol{\varphi},\boldsymbol{q},\boldsymbol{q}^{*}) = \mathscr{J}(\boldsymbol{\varphi},\boldsymbol{q}) + (\boldsymbol{q}^{*},\boldsymbol{B}(\boldsymbol{\varphi},\boldsymbol{q})) \tag{3.17}$$

$$\equiv \mathscr{J}(\boldsymbol{\varphi},\boldsymbol{q}) + \int_0^T \int_\Omega \pi \nabla\cdot\widetilde{\boldsymbol{u}}\,\mathrm{d}\boldsymbol{x}\,\mathrm{d}t + \int_0^T \left[\tau\frac{\mathrm{d}\widehat{\boldsymbol{V}}}{\mathrm{d}t} - (\boldsymbol{V}-\widehat{\boldsymbol{V}})\right]\cdot\boldsymbol{\chi}\,\mathrm{d}t$$

$$+ \int_0^T \int_\Omega \Bigg[\frac{\partial\widetilde{\boldsymbol{u}}}{\partial t} + \widetilde{\boldsymbol{u}}\cdot\nabla\widetilde{\boldsymbol{u}} + \frac{1}{\rho}\nabla\widetilde{p} - f_\infty\boldsymbol{e}_1 - \nabla\cdot\boldsymbol{\tau}_M - \boldsymbol{f}$$

$$- \delta(\boldsymbol{x}-z_1\boldsymbol{e}_3)\boldsymbol{\tau}_{\boldsymbol{w}}\Bigg]\cdot\boldsymbol{\xi}\,\mathrm{d}\boldsymbol{x}\,\mathrm{d}t, \tag{3.18}$$

Now, if the reduced optimization problem is considered, it can be found trivially that (see e.g. Borzi & Schultz [12])

$$\tilde{\mathscr{J}}(\boldsymbol{\varphi}) = \mathscr{L}(\boldsymbol{\varphi},\boldsymbol{q}(\boldsymbol{\varphi}),\boldsymbol{q}^{*}) = \mathscr{J}(\boldsymbol{\varphi},\boldsymbol{q}(\boldsymbol{\varphi})) + (\boldsymbol{q}^{*},\boldsymbol{B}(\boldsymbol{\varphi},\boldsymbol{q}(\boldsymbol{\varphi}))), \tag{3.19}$$

since by definition the implicit relation $\boldsymbol{q}(\boldsymbol{\varphi})$ is equivalent to $\boldsymbol{B}(\boldsymbol{\varphi},\boldsymbol{q}(\boldsymbol{\varphi})) \equiv 0$. Thus, applying the chain rule of differentiation, and using the Riesz representation theorem, this leads to

$$\begin{aligned}(\nabla\tilde{\mathscr{J}},\delta\boldsymbol{\varphi}) &= \left(\frac{\partial\mathscr{J}}{\partial\boldsymbol{\varphi}},\delta\boldsymbol{\varphi}\right) + \left(\boldsymbol{q}^{*},\frac{\partial\boldsymbol{B}}{\partial\boldsymbol{\varphi}}\delta\boldsymbol{\varphi}\right)\\ &\quad + \left(\frac{\partial\mathscr{J}}{\partial\boldsymbol{q}},\frac{\partial\boldsymbol{q}}{\partial\boldsymbol{\varphi}}\delta\boldsymbol{\varphi}\right) + \left(\boldsymbol{q}^{*},\frac{\partial\boldsymbol{B}}{\partial\boldsymbol{q}}\frac{\partial\boldsymbol{q}}{\partial\boldsymbol{\varphi}}\delta\boldsymbol{\varphi}\right)\\ &= \left(\frac{\partial\mathscr{J}}{\partial\boldsymbol{\varphi}},\delta\boldsymbol{\varphi}\right) + \left(\left[\frac{\partial\boldsymbol{B}}{\partial\boldsymbol{\varphi}}\right]^{*}\boldsymbol{q}^{*},\delta\boldsymbol{\varphi}\right)\\ &\quad + \left(\left\{\frac{\partial\mathscr{J}}{\partial\boldsymbol{q}} + \left[\frac{\partial\boldsymbol{B}}{\partial\boldsymbol{q}}\right]^{*}\boldsymbol{q}^{*}\right\},\delta\boldsymbol{q}\right) + BT_1\end{aligned} \tag{3.20}$$

Now, provided that

$$\mathscr{L}_{\boldsymbol{q}}(\delta\boldsymbol{q}) = \left(\frac{\partial\mathscr{L}}{\partial\boldsymbol{q}},\delta\boldsymbol{q}\right) = \left(\left\{\frac{\partial\mathscr{J}}{\partial\boldsymbol{q}} + \left[\frac{\partial\boldsymbol{B}}{\partial\boldsymbol{q}}\right]^{*}\boldsymbol{q}^{*}\right\},\delta\boldsymbol{q}\right) + BT_1 = 0, \tag{3.21}$$

which defines the adjoint equations and boundary conditions (cf. further §3.5.5), one can identify the gradient of the cost functional as

$$\nabla\tilde{\mathscr{J}} = \frac{\partial\mathscr{L}}{\partial\boldsymbol{\varphi}} = \frac{\partial\mathscr{J}}{\partial\boldsymbol{\varphi}} + \left[\frac{\partial\boldsymbol{B}}{\partial\boldsymbol{\varphi}}\right]^{*}\boldsymbol{q}^{*}, \tag{3.22}$$

where $[\partial \boldsymbol{B}/\partial \boldsymbol{\varphi}]^*$ is the adjoint of $\partial \boldsymbol{B}/\partial \boldsymbol{\varphi}$ (cf. §3.4.1), and $\boldsymbol{q}^* = (\boldsymbol{\xi}, \pi, \boldsymbol{\chi})$ is the solution of the adjoint equations (see further below). This can be evaluated at the cost of one adjoint LES simulation, and does not need a direct evaluation of $\delta \boldsymbol{q}$. Using (3.22), (3.18), (2.7) and either of (3.1) or (3.2), the gradient of the reduced cost functional may be written as

$$\begin{aligned}\nabla \tilde{\mathscr{J}} &= \frac{\partial \mathscr{J}}{\partial \boldsymbol{\varphi}} + \frac{1}{2}\int_\Omega \widehat{\boldsymbol{V}}^{\circ 2} \circ \boldsymbol{\mathscr{R}}(\mathbf{x})\,[\boldsymbol{\xi}\cdot\boldsymbol{e}_\perp]\,\mathrm{d}\boldsymbol{x} \\ &= \frac{1}{2}\int_\Omega \widehat{\boldsymbol{V}}^{\circ 2} \circ \boldsymbol{\mathscr{R}}(\mathbf{x})\,[(-\widetilde{\boldsymbol{u}} + \boldsymbol{\xi})\cdot\boldsymbol{e}_\perp]\,\mathrm{d}\boldsymbol{x}, \end{aligned} \tag{3.23}$$

with $\boldsymbol{\mathscr{R}} \equiv [\mathscr{R}_1, \cdots, \mathscr{R}_{N_t}]$, and where $\circ$ is used to denote the entry-wise product (or Hadamard product), and $\widehat{\boldsymbol{V}}^{\circ 2}$ is the entry-wise square of $\widehat{\boldsymbol{V}}$. Furthermore, $\boldsymbol{\xi}(\boldsymbol{x}, t)$ is the adjoint velocity field that is obtained by solving the adjoint equations.

3.5 Derivation of the adjoint equations

From (3.21), it is clear that the adjoint equations can be found by expressing $\mathscr{L}_{\boldsymbol{q}}(\delta \boldsymbol{q}) = 0$ in its Riesz representation form $(\partial \mathscr{L}/\partial \boldsymbol{q}, \delta \boldsymbol{q}) = 0$. Thus, based on (3.18) one can express

$$\begin{aligned}\mathscr{L}_{\boldsymbol{q}}(\delta \boldsymbol{q}) =& \mathscr{L}_{\widetilde{\boldsymbol{u}}}(\delta \widetilde{\boldsymbol{u}}) + \mathscr{L}_{\widetilde{p}}(\delta \widetilde{p}) + \mathscr{L}_{\widehat{\boldsymbol{V}}}(\delta \widehat{\boldsymbol{V}}) \\ =& \mathscr{J}_{\widetilde{\boldsymbol{u}}}(\delta \widetilde{\boldsymbol{u}}) + \int_0^T \int_\Omega (\nabla \cdot \delta \widetilde{\boldsymbol{u}})\pi \,\mathrm{d}\boldsymbol{x}\,\mathrm{d}t - \int_0^T \boldsymbol{V}_{\widetilde{\boldsymbol{u}}}(\delta \widetilde{\boldsymbol{u}}) \cdot \boldsymbol{\chi}\,\mathrm{d}t \\ &+ \underbrace{\int_0^T \int_\Omega \Big[\frac{\partial \delta \widetilde{\boldsymbol{u}}}{\partial t} + (\widetilde{\boldsymbol{u}} \cdot \nabla)\delta \widetilde{\boldsymbol{u}} + (\delta \widetilde{\boldsymbol{u}} \cdot \nabla)\widetilde{\boldsymbol{u}} - \nabla \cdot (\boldsymbol{\tau}_M{}_{\widetilde{\boldsymbol{u}}}(\delta \boldsymbol{u})) - \delta(\boldsymbol{x} - z_1 \boldsymbol{e}_3)\boldsymbol{\tau}_{\boldsymbol{w}}{}_{\widetilde{\boldsymbol{u}}}(\delta \widetilde{\boldsymbol{u}}) \Big] \cdot \boldsymbol{\xi}\,\mathrm{d}\boldsymbol{x}\,dt}_{\mathscr{L}_{\widetilde{\boldsymbol{u}}}(\delta \boldsymbol{u})} \\ &+ \underbrace{\int_0^T \int_\Omega \boldsymbol{\xi} \cdot \nabla \delta \widetilde{p}\,\mathrm{d}\boldsymbol{x}\,\mathrm{d}t}_{\mathscr{L}_{\widetilde{p}}(\delta \widetilde{p})} \end{aligned} \tag{3.24}$$

$$+\ \mathscr{J}_{\widehat{\boldsymbol{V}}}(\delta\widehat{\boldsymbol{V}}) - \int_0^T \int_\Omega \boldsymbol{f}_{\widehat{\boldsymbol{V}}}(\delta\widehat{\boldsymbol{V}}) \cdot \boldsymbol{\xi}\, \mathrm{d}\boldsymbol{x}\, \mathrm{d}t \tag{3.25}$$

$$\underbrace{+ \int_0^T \left[\tau \frac{\mathrm{d}(\delta\widehat{\boldsymbol{V}})}{\mathrm{d}t} + \delta\widehat{\boldsymbol{V}}\right] \cdot \boldsymbol{\chi}\, \mathrm{d}t.}_{\mathscr{L}_{\widehat{\boldsymbol{V}}}(\delta\widehat{\boldsymbol{V}})}$$

Since $\mathscr{J}_{\widetilde{p}}(\delta\widetilde{p}) = 0$, it drops out from the above expression (cf. (3.1), (3.2)).

Casting (3.25) in the form $(\partial\mathscr{L}/\partial\boldsymbol{q}, \delta\boldsymbol{q}) = 0$ is now a matter of exchanging $\delta\boldsymbol{q}$ and $\boldsymbol{q}^*$ by partial integration and similar algebraic manipulations. The adjoint equations are then identified with $\partial\mathscr{L}/\partial\boldsymbol{q}$, and boundary conditions are defined by the requirement that the boundary terms originating from the partial integration are equal to zero. This procedure is well known, and for details regarding the derivation of the adjoint equations for the standard Navier–Stokes equations, the reader is referred to Choi *et al.* [22], Bewley *et al.* [10] and Delport *et al.* [26], among others. The current dissertation only discusses the derivation of the adjoints with respect to the additional terms that do not appear in the standard DNS adjoint equations, i.e. the adjoint forcing term $\boldsymbol{f}^*$ ((3.41) and (3.28)), the adjoint time-filtered velocity, the adjoint wall-stress model, and the adjoint Smagorinsky model. The resulting adjoint equations in their final form are presented in subsection 3.5.5

3.5.1 Adjoint forcing term

The adjoint forcing term $\boldsymbol{f}^*$ is identified from (using (3.25), (3.1) and (2.9))

$$(-\boldsymbol{f}^*, \delta\widetilde{\boldsymbol{u}}) = \mathscr{J}_{\widetilde{\boldsymbol{u}}}(\delta\widetilde{\boldsymbol{u}}) - \int_0^T \boldsymbol{V}_{\widetilde{\boldsymbol{u}}}(\delta\widetilde{\boldsymbol{u}}) \cdot \boldsymbol{\chi}\, \mathrm{d}t \tag{3.26}$$

$$= \int_0^T \int_\Omega \sum_{i=1}^{N_t} -\frac{1}{2} C'_{\mathrm{T,i}} \widehat{V}_i^2\, \mathscr{R}_i(\boldsymbol{x})\, \boldsymbol{e}_\perp \cdot \delta\widetilde{\boldsymbol{u}}\, \mathrm{d}\boldsymbol{x}\, \mathrm{d}t$$

$$- \int_0^T \sum_{i=1}^{N_t} \left(\frac{1}{A} \int_\Omega \chi_i\, \mathscr{R}_i(\boldsymbol{x}) \boldsymbol{e}_\perp \cdot \delta\widetilde{\boldsymbol{u}}\ \mathrm{d}\boldsymbol{x}\right)\ \mathrm{d}t. \tag{3.27}$$

Thus,

$$\boldsymbol{f}^* = \sum_{i=1}^{N_t} \left(\frac{1}{2} C'_{T,i} \widehat{V}_i^2 + \frac{\chi_i}{A}\right) \mathscr{R}_i(\boldsymbol{x}) \boldsymbol{e}_\perp. \tag{3.28}$$

3.5.2 Adjoint of the time-filtered velocity

The adjoint of the velocity time filter corresponds to $\partial\mathscr{L}/\partial\widehat{\boldsymbol{V}} = 0$, and follows from expressing the Riesz representation of $\mathscr{L}_{\widehat{\boldsymbol{V}}}(\delta\widehat{\boldsymbol{V}})$. Thus, substituting for $\mathscr{J}$ and $\boldsymbol{f}$ yields

$$\begin{aligned}\left(\frac{\partial\mathscr{L}}{\partial\widehat{\boldsymbol{V}}}, \delta\widehat{\boldsymbol{V}}\right) &= \int_0^T \int_\Omega \sum_{i=1}^{N_t} C'_{\mathrm{T,i}} \widehat{V}_i \mathscr{R}_i(\mathbf{x})\ (-\widetilde{\boldsymbol{u}} + \boldsymbol{\xi})\cdot\boldsymbol{e}_\perp \delta\widehat{V}_i \,\mathrm{d}\boldsymbol{x}\,\mathrm{d}t \\ &\quad + \int_0^T \sum_{i=1}^{N_t} \left[\tau\frac{\mathrm{d}\delta\widehat{V}_i}{\mathrm{d}t} + \delta\widehat{V}_i\right]\cdot\chi_i \,\mathrm{d}t \\ &= \int_0^T \sum_{i=1}^{N_t} \left\{-\tau\frac{\mathrm{d}\chi_i}{\mathrm{d}t} + \chi_i + C'_{\mathrm{T,i}}\widehat{V}_i \int_\Omega \mathscr{R}_i(\mathbf{x})(\boldsymbol{\xi} - \widetilde{\boldsymbol{u}})\cdot\boldsymbol{e}_\perp \mathrm{d}\boldsymbol{x}\right\}\delta\widehat{V}_i \,\mathrm{d}t \\ &\quad + \sum_{i=1}^{N_t} \tau\left[\delta\widehat{V}_i\cdot\chi_i\right]_0^T. \end{aligned} \tag{3.29}$$

This identifies the adjoint time filter in Eq.(3.41). The boundary term $[\delta\widehat{V}_i\cdot\chi_i]_0^T$ vanishes provided that $\chi_i(T) = 0$ (at $t = 0$, $\delta\widehat{V}_i(0) = 0$ is given). This yields the boundary condition for the adjoint time filter, i.e.

$$\chi_i(T) = 0 \qquad \text{for } \ i = 1\cdots N_t. \tag{3.30}$$

3.5.3 Adjoint of the wall-stress boundary condition

The wall-stress model (2.3) and (2.4) has two wall-parallel components, while the third component equals zero. Starting from (3.25), the adjoint can be identified through

$$\begin{aligned}(\boldsymbol{\tau}^*_{\boldsymbol{w}}, \delta\widetilde{\boldsymbol{u}}) = \int_0^T \int_\Omega \left[\frac{\kappa}{\ln(z_1/z_0)}\right]^2 \Bigg\{ &\|\widetilde{\boldsymbol{u}}\|_{12}\overline{\overline{\delta\widetilde{u}}}_i\xi_i \\ &+ \frac{\overline{\overline{\widetilde{u}}}_i\overline{\overline{\delta\widetilde{u}}}_i(\overline{\overline{\widetilde{u}}}_1\xi_1 + \overline{\overline{\widetilde{u}}}_2\xi_2)}{\|\widetilde{\boldsymbol{u}}\|_{12}}\Bigg\}\delta(\boldsymbol{x} - z_1\boldsymbol{e}_3)\,\mathrm{d}\boldsymbol{x}\,\mathrm{d}t, \end{aligned} \tag{3.31}$$

using the Einstein summation convention over repeated indices ($i = 1, 2$), and the short-hand notation $\|\widetilde{\boldsymbol{u}}\|_{12} = (\overline{\overline{\widetilde{u}}}_1^2 + \overline{\overline{\widetilde{u}}}_2^2)^{1/2}$. Furthermore, the wall-parallel

filtering is defined as

$$\overline{\widetilde{u}}_i = \iint_\Omega G(\boldsymbol{x}-\boldsymbol{x}')\ \widetilde{u}_i(x_1', x_2', x_3)\mathrm{d}x_1'\mathrm{d}x_2', \tag{3.32}$$

with $G(\boldsymbol{x}-\boldsymbol{x}') = [6/(\pi\Delta^2)]\exp(-6\|\boldsymbol{x}-\boldsymbol{x}'\|_{12}^2/\Delta^2)$.

Further elaboration of (3.31) requires the transfer of wall-parallel filter operations from $\delta\widetilde{u}_i$ to ξ_i. This is straightforward, since the selected Gaussian filter is self-adjoint, i.e. for any two fields $\boldsymbol{\psi}$ and $\boldsymbol{\phi}$

$$\begin{aligned}
(\overline{\boldsymbol{\psi}}, \boldsymbol{\phi}) =& \int_0^T \int_\Omega \overline{\boldsymbol{\psi}} \cdot \boldsymbol{\phi}\ \ \mathrm{d}\boldsymbol{x}\mathrm{d}t \\
=& \int_0^T \iiint_\Omega \left(\iint_\Omega G(\boldsymbol{x}-\boldsymbol{x}')\ \boldsymbol{\psi}(x_1', x_2', x_3)\,\mathrm{d}x_1'\mathrm{d}x_2' \right) \cdot \boldsymbol{\phi}(\boldsymbol{x})\ \mathrm{d}x_1\mathrm{d}x_2\mathrm{d}x_3\mathrm{d}t \\
=& \int_0^T \iiint_\Omega \left(\iint_\Omega G(\boldsymbol{x}-\boldsymbol{x}')\ \boldsymbol{\phi}(\boldsymbol{x})\,\mathrm{d}x_1\mathrm{d}x_2 \right) \cdot \boldsymbol{\psi}(x_1', x_2', x_3)\ \mathrm{d}x_1'\mathrm{d}x_2'\mathrm{d}x_3\mathrm{d}t \\
=& (\boldsymbol{\psi}, \overline{\boldsymbol{\phi}}).
\end{aligned} \tag{3.33}$$

Using this in (3.31) leads to

$$\begin{aligned}
(\boldsymbol{\tau}_{\boldsymbol{w}}^*, \delta\widetilde{\boldsymbol{u}}) = \int_0^T \int_\Omega \left[\frac{\kappa}{\ln(z_1/z_0)}\right]^2 \Bigg\{ & \overline{\|\widetilde{\boldsymbol{u}}\|_{12}\xi_i}\,\delta\widetilde{u}_i \\
& + \overline{\left(\frac{\overline{\widetilde{u}}_1\xi_1 + \overline{\widetilde{u}}_2\xi_2}{\|\widetilde{\boldsymbol{u}}\|_{12}}\overline{\widetilde{u}}_i\right)}\,\delta\widetilde{u}_i \Bigg\} \delta(\boldsymbol{x}-z_1\boldsymbol{e}_3)\ \mathrm{d}\boldsymbol{x}\ \mathrm{d}t,
\end{aligned} \tag{3.34}$$

yielding,

$$\tau_{w,i}^* = -\left[\frac{\kappa}{\log(z_1/z_0)}\right]^2 \overline{\left\{ \left(\overline{\widetilde{u}}_1^2 + \overline{\widetilde{u}}_2^2\right)^{1/2} \xi_i + \frac{\overline{\widetilde{u}}_1\xi_1 + \overline{\widetilde{u}}_2\xi_2}{\left(\overline{\widetilde{u}}_1^2 + \overline{\widetilde{u}}_2^2\right)^{1/2}} \overline{\widetilde{u}}_i \right\}}, \quad \text{for} \quad i = 1, 2, \tag{3.35}$$

and $\boldsymbol{\tau}_{\boldsymbol{w}}^* = [\tau_{w,1}^*, \tau_{w,2}^*, 0]$.

3.5.4 Adjoint of the subgrid-scale model

The adjoint of the subgrid-scale stresses are identified through (cf. (3.25) and (2.5))

$$(\nabla \cdot \boldsymbol{\tau}^*_{\boldsymbol{M}}, \delta\widetilde{\boldsymbol{u}}) = \int_0^T \int_\Omega \nabla \cdot (\boldsymbol{\tau}_{M\widetilde{\boldsymbol{u}}}(\delta\widetilde{\boldsymbol{u}})) \cdot \boldsymbol{\xi} \, \mathrm{d}\boldsymbol{x} \, \mathrm{d}t \tag{3.36}$$

$$= \int_0^T \int_\Omega \nabla \cdot \left(2\ell^2 \left[\frac{(2\boldsymbol{S} : \delta\boldsymbol{S})\boldsymbol{S}}{(2\boldsymbol{S} : \boldsymbol{S})^{1/2}} + (2\boldsymbol{S} : \boldsymbol{S})^{1/2} \delta\boldsymbol{S} \right] \right) \cdot \boldsymbol{\xi} \, \mathrm{d}\boldsymbol{x} \, \mathrm{d}t \tag{3.37}$$

with $\delta\boldsymbol{S} = (\nabla\delta\widetilde{\boldsymbol{u}} + (\nabla\delta\widetilde{\boldsymbol{u}})^T)/2$. Using integration by parts on (3.37), and the fact that $\boldsymbol{S}$ and $\delta\boldsymbol{S}$ are symmetric tensors, leads to

$$(\nabla \cdot \boldsymbol{\tau}^*_{\boldsymbol{M}}, \delta\widetilde{\boldsymbol{u}}) = \int_0^T \Bigg\{ BT - \int_\Omega \Bigg(2\ell^2 \Bigg[\frac{(2\boldsymbol{S} : \delta\boldsymbol{S})\boldsymbol{S}}{(2\boldsymbol{S} : \boldsymbol{S})^{1/2}} + (2\boldsymbol{S} : \boldsymbol{S})^{1/2} \delta\boldsymbol{S} \Bigg] \Bigg) : \boldsymbol{S}^* \, \mathrm{d}\boldsymbol{x} \Bigg\} \mathrm{d}t, \tag{3.38}$$

with $\boldsymbol{S}^* = (\nabla\boldsymbol{\xi} + (\nabla\boldsymbol{\xi})^T)/2$. The boundary term $BT = 0$, since ℓ equals zero at $x_3 = 0$, $\boldsymbol{S}$ equals zero at the top boundary, and periodic boundary conditions are used in the other directions. A second integration by parts yields

$$(\nabla \cdot \boldsymbol{\tau}^*_{\boldsymbol{M}}, \delta\widetilde{\boldsymbol{u}}) = \int_0^T \Bigg\{ BT' + \int_\Omega \nabla \cdot \Bigg(2\ell^2 \Bigg[\frac{(2\boldsymbol{S} : \boldsymbol{S}^*)\boldsymbol{S}}{(2\boldsymbol{S} : \boldsymbol{S})^{1/2}} + (2\boldsymbol{S} : \boldsymbol{S})^{1/2} \boldsymbol{S}^* \Bigg] \Bigg) \cdot \delta\widetilde{\boldsymbol{u}} \, \mathrm{d}\boldsymbol{x} \Bigg\} \mathrm{d}t. \tag{3.39}$$

The boundary term $BT' = 0$, provided that $\boldsymbol{S}^* = 0$ at the top boundary (consistent with a symmetry boundary condition), and periodic boundary conditions are used for $\boldsymbol{\xi}$ in wall-parallel directions. Then (3.39) identifies the adjoint subgrid-scale stresses, i.e.

$$\boldsymbol{\tau}^*_M = 2\ell_s^2 \left(\frac{2\boldsymbol{S} : \boldsymbol{S}^*}{(2\boldsymbol{S} : \boldsymbol{S})^{1/2}} \boldsymbol{S} + (2\boldsymbol{S} : \boldsymbol{S})^{1/2} \boldsymbol{S}^* \right), \tag{3.40}$$

where $\boldsymbol{S}^* = (\nabla\boldsymbol{\xi} + (\nabla\boldsymbol{\xi})^T)/2$.

3.5.5 Adjoint equations and boundary conditions

The resulting adjoint equations correspond to

$$-\frac{\partial \boldsymbol{\xi}}{\partial t} - \widetilde{\boldsymbol{u}} \cdot \nabla \boldsymbol{\xi} - (\nabla \boldsymbol{\xi})^T \cdot \widetilde{\boldsymbol{u}} = -\frac{1}{\rho}\nabla \pi + \nabla \cdot \boldsymbol{\tau}_M^* + \boldsymbol{f}^* + \delta(\boldsymbol{x} - z_1 \boldsymbol{e}_3)\boldsymbol{\tau}_{\boldsymbol{w}}^*$$

$$\nabla \cdot \boldsymbol{\xi} = 0 \tag{3.41}$$

$$-\frac{\mathrm{d}\chi_i}{\mathrm{d}t} = \frac{1}{\tau}\left[-\chi_i + C'_{T,i}\widehat{V}_i \int_\Omega \mathscr{R}_i(\mathbf{x})\ (\widetilde{\boldsymbol{u}} - \boldsymbol{\xi})\cdot \boldsymbol{e}_\perp \,\mathrm{d}\boldsymbol{x}\right], \qquad \text{for } \ i = 1 \cdots N_t,$$

where $\boldsymbol{f}^*$, $\boldsymbol{\tau}_{\boldsymbol{w}}^*$ and $\boldsymbol{\tau}_M^*$ are given by Eq. (3.28), (3.35) and (3.40) respectively.

The spatial boundary conditions of the adjoint equations are equivalent to those of the forward equations. In the streamwise and spanwise directions, periodic boundary conditions are required. In the normal direction, impermeability is required at the top and the bottom walls, and a symmetry boundary condition is required at the top wall. For the 'initial conditions', it is important to realize that the adjoint equations are solved backwards in time (cf. the sign of the time derivatives), so the 'initial' conditions should be provided at $t = T$. They correspond to

$$\boldsymbol{\xi}(\boldsymbol{x}, T) = 0 \qquad \text{for } \mathscr{J}_1(\boldsymbol{\varphi}, \boldsymbol{q}), \tag{3.42}$$

$$\boldsymbol{\xi}(\boldsymbol{x}, T) = \gamma \widetilde{\boldsymbol{u}}(\boldsymbol{x}, T) \qquad \text{for } \mathscr{J}_2(\boldsymbol{\varphi}, \boldsymbol{q}), \tag{3.43}$$

$$\chi_i(T) = 0 \qquad \text{for } \ i = 1 \cdots N_t. \tag{3.44}$$

The adjoint equations (3.41) show some similarity to the flow equations of the forward problem, e.g. time derivatives and convective terms can be recognized (though with different signs), continuity looks the same, and there is also an adjoint pressure variable. Therefore, much of the discretization of the forward problem can be reused, with the same pseudospectral discretization in the horizontal directions, in combination with a fourth-order energy-conservative discretization in the vertical direction. For the time integration, a fourth-order Runge–Kutta method is also used. Note that the adjoint equations follow from a linearization of the governing equations around a state $(\widetilde{\boldsymbol{u}}, \widetilde{p}, \widehat{\boldsymbol{V}})$. In the adjoint equations, this state is also required (cf. Eq. (3.41)). To this end, the nonlinear forward problem is solved first, and the full space-time state is stored on disk. Subsequently, it is used during the solution of the adjoint equations.

Finally, for the discretization of the filter equation, a time discretization that is equivalent to the discrete adjoint of the discrete forward filter equation (2.11)

Table 3.1: Summary of the case set-up for verification of the adjoints.

Domain size	$L_x \times L_y \times H = 3.5 \times 2 \times 1$ km^3
Driving pressure gradient	$f_\infty = 4 \times 10^{-4}$ m/s^2
Turbine dimensions	$D = 0.1H = 100$ m, $z_h = 0.1H = 100$ m
Number of turbine	1
C'_T	1.33
Surface roughness	$z_0 = 10^{-4}H = 0.1$m
Grid size	$N_x \times N_y \times N_z = 128 \times 128 \times 80$
Cell size	$\Delta_x \times \Delta_y \times \Delta_z = 27.3 \times 15.6 \times 12.5$ m^3
Time step	0.7 s

is chosen. This corresponds to

$$\chi_i^{n-1} = (1-\alpha)\chi_i^n + \alpha C'_{T,i}\widehat{V}_i^{n-1}\int_\Omega \mathscr{R}_i(\mathbf{x})\,(\widetilde{\boldsymbol{u}} - \boldsymbol{\xi})\cdot\boldsymbol{e}_\perp \,\mathrm{d}\boldsymbol{x}. \tag{3.45}$$

3.6 Verification of the adjoints

The implementation of the adjoint equations is verified in this section by comparing the adjoint-based gradients with those obtained from a finite difference method. Such a comparison is not feasible for the actual case setup, which has 50 turbines and each turbine is allowed to change its thrust coefficient as a function of time. As stated earlier, the degrees of freedom of the control parameter in this setup is approximately 2×10^4, requiring the same number of flow simulations (plus an additional base flow simulation) for the gradient calculation with a finite difference approach. Therefore, for the purpose of comparison, a case with a single turbine and a reduced domain size is considered. Additionally, in this setup, the thrust coefficient does not change in every time step, but instead it is kept constant during the simulation, i.e. there is only one control parameter. Details of the modified case set-up are summarized in Table 3.1.

Figure 3.2 displays snapshots of the instantaneous velocity field and adjoint field in a vertical plane through the turbine. The wake downstream of the

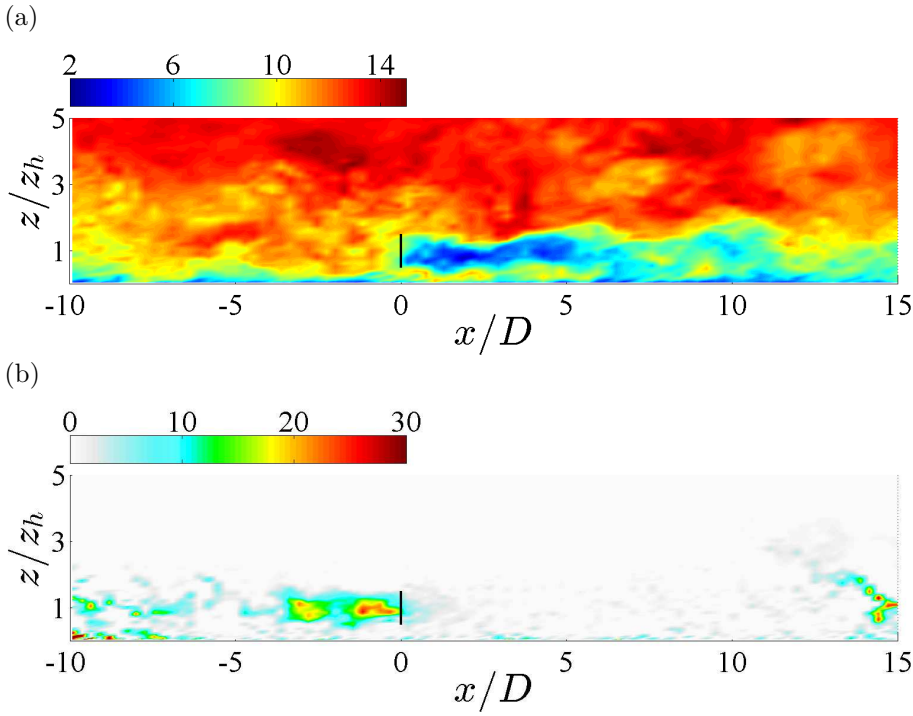

Figure 3.2: Contours of (a) instantaneous streamwise velocity field, (b) instantaneous streamwise adjoint field in a vertical plane through the turbine.

turbine is clearly visible in figure 3.2(a). However, it gets weaker starting from $x/D \approx 5$, as a result of wake expansion and entrainment from the surrounding flow. Nevertheless, the wake persists (although small) for a very long distance downstream of the turbine. Unlike the flow field, the adjoint field in 3.2(b) propagates upstream in the domain, since the adjoint equations (3.41) are solved backward in time. It can be appreciated from the figure that the turbine acts as a source term. This is because the cost function which is defined at the turbine location is a driving force in the adjoint simulation.

For the verification of the adjoints, the base flow and the adjoint simulations presented in figure 3.2 are first performed. Information from these two simulations can be used to calculate the adjoint-based gradient $\nabla\tilde{\mathscr{J}}_{\text{adj}}$ using Eq.(3.23). Next, the control is slightly perturbed with a disturbance $\mathrm{d}C_T' << C_T'$ and a flow simulation is performed with this modified control. Using the cost functional information from the base simulation $\mathscr{J}(C_T')$ and the perturbed

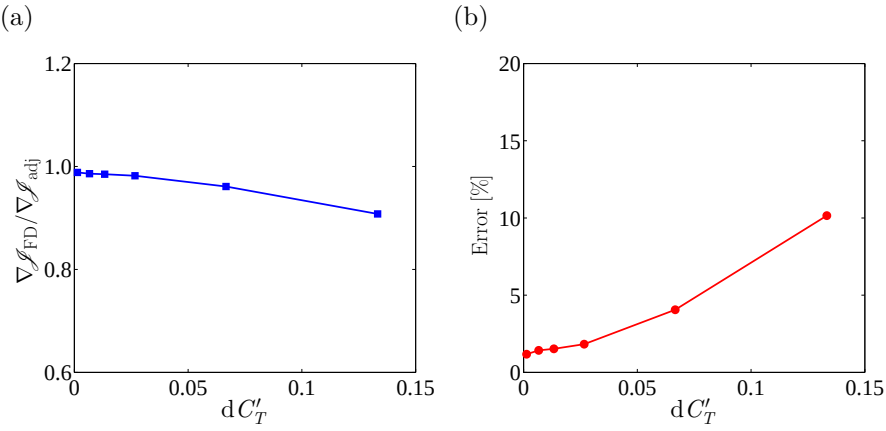

Figure 3.3: Comparison of the adjoint-based and finite-difference based gradients. (a) Ratio of the finite-difference based and adjoint-based gradients. (b) Error in the adjoint-based gradient computation.

simulation $\mathscr{J}(C_T' + \mathrm{d}C_T')$, the gradient can be approximated as

$$\nabla\tilde{\mathscr{J}}_{\mathrm{FD}} = \frac{\tilde{\mathscr{J}}(C_T' + \mathrm{d}C_T') - \tilde{\mathscr{J}}(C_T')}{\mathrm{d}C_T'}, \tag{3.46}$$

where FD stands for finite difference. An important issue with the gradient calculation using the finite difference method is the choice of the perturbation magnitude [79]. For the forward-difference approximation of Eq. (3.46), the truncation error or discretization error is proportional to the size of the perturbation. Therefore, in order to minimize the discretization error, it is preferable to choose the perturbation as small as possible. However, due to the finite precision of the floating point representation during the computation, an extremely small perturbation can introduce roundoff errors which can be significant. Nevertheless, one can obtain accurate gradient information using the finite-difference approximation, if the perturbation size is chosen properly [58].

Results of the comparison are presented in figure 3.3(a) as a ratio of $\nabla\tilde{\mathscr{J}}_{\mathrm{FD}}$ and $\nabla\tilde{\mathscr{J}}_{\mathrm{adj}}$. For small perturbations (i.e. $\mathrm{d}C_T' \leq 2\%$ of C_T'), the adjoint-based gradient agrees very well with its finite difference counterpart, verifying the fact that the adjoint solution is able to compute the gradient accurately. The error margin, as shown in figure 3.3(b), is well within 2% for smaller $\mathrm{d}C_T'$. When the perturbation is large, i.e. $\mathrm{d}C_T' \geq 5\%$ of C_T', the finite-difference gradient shows a strong deviation. As explained above, this is due to the fact that for large $\mathrm{d}C_T'$, finite-difference approximation cannot accurately predict the gradient.

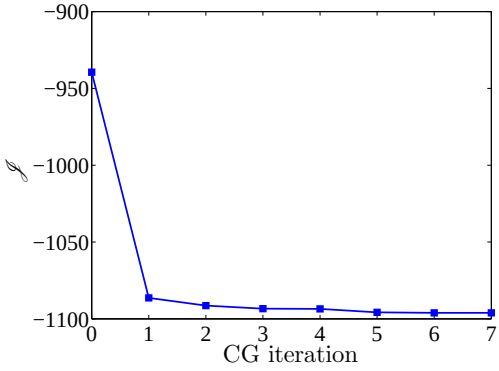

Figure 3.4: Convergence of the cost functional over the conjugate-gradient iteration.

Convergence of the cost functional

Figure 3.4 shows the convergence history of the cost function as a function of the conjugate-gradient iteration. While the domain size, grid resolutions and turbine parameters (rotor diameter and hub height) are kept the same as those described in Table 3.1, the thrust coefficient is now allowed to change freely during the simulation. The first CG iteration achieves about a 15% reduction in the cost function (equivalent to an increase in the energy extraction by the turbine). The reduction is not equally significant for the higher iterations, and beyond the fifth iteration, convergence is almost flat. Therefore, it can be concluded that the optimization results are well converged. Note, however, that in order to limit the computational cost, the number of function evaluations (LES simulations) during the line search is limited in this dissertation, and the result may differ if such constraint is removed.

3.7 Summary

In this chapter, the optimization approach employed in the current dissertation was presented. The cost functionals based on the wind-farm energy extraction and the PDE-constrained optimization problem for the wind-farm boundary layers in the large-eddy simulation were defined and discussed. The non-linear Polak-Ribière conjugate-gradient method [10] and the Brent line search algorithm [84, 65, 79] are chosen for the solution of the optimization problem. Moreover, the gradient of the cost functional required by the conjugate-gradient method was determined using a continuous adjoint-based approach. To this

end, the formal Lagrangian method was followed to derive the adjoint equations and formulate the gradient of the cost functionals. The adjoint equations for the standard Navier-Stokes equations were extended to include the adjoints for the Smagorinsky model and wall-stress model, and the adjoint of the actuator disk model. The implementation of the adjoint equations was first verified by comparing the adjoint-based gradients with those obtained from a finite difference method. It was found that both the gradients agreed very well, and the error margin for the adjoint-based gradient was well within 2%. Finally, the performance of the optimization algorithm was tested by analyzing the convergence history of the cost functional. It was observed that the optimization results converged very well and that after the first five conjugate-gradient iterations, the profile was almost flat.

Chapter 4

Optimal control of a very large wind farm

This chapter presents the results of the optimal coordinated control of infinite wind-farm boundary layers. The work discussed in this chapter is published in Goit & Meyers [39]. Methods and formulations discussed in Chapter 3 are used for the optimization. The chapter is organized as follows. Section 4.1 gives details about the computational set-up. In Section 4.2, results for the unpenalized case, corresponding to the cost functional of Eq. (3.1), are discussed. Section 4.3 presents results for the penalized cases corresponding to the cost functionals defined by Eq. (3.2).

4.1 Computational set-up

In the current section, computational details for the optimization studies are provided. The choice of the box constraints imposed on the controls is also discussed. Finally, the convergence history of the current optimization setup is presented.

The geometrical setup, grid, time step, etc. remain the same as in §2.3.1 (cf. Table 2.2). The optimal control is started from a statistically stationary field of an 'uncontrolled', and $\varphi^{(0)} = 1.33$ is used for the starting value of the optimization algorithm.

As already introduced in Section 3.2, box constraints are imposed on the

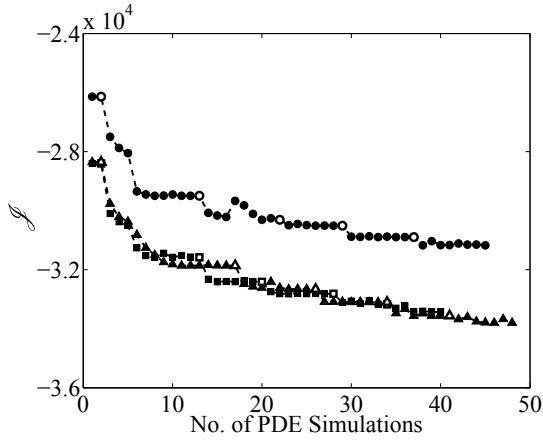

Figure 4.1: Typical convergence history of a conjugate-gradient optimization for three different control windows $[(n-1)T_A, (n-1)T_A+T]$, with (■): control window $n = 1$; (▲): control window $n = 13$; (●): control window $n = 20$. Open symbols (○, □, △) correspond to adjoint simulations required for gradient evaluations, and are plotted at the same cost-functional level as the previous forward simulation.

controls, i.e. $0 \leq C'_{T,i}(t) \leq 4$. The lower constraint prevents the turbine from starting to operate as a fan, even if the optimization algorithm would ask for this. For the upper boundary, we do not want a priori to limit C'_T to the Betz limit ($C'_T = 2$), but at the same time, it cannot be left free as $C'_T \to \infty$ is not very practicable from a turbine-construction point of view. Therefore, an ad-hoc limit of $C'_T = 4$ is selected, which, e.g. corresponds to a wind turbine that is constructed with double blade chord lengths compared to the Betz-optimal blade design (cf. Appendix A). Moreover, an extra case with optimal control over one control window without box constraints on C'_T (and using $\gamma = 0$) has also been investigated. For this case, it was found that C'_T fluctuates between -19 and $+24$, but compared to the case with box constraints, this leads to no significant additional energy extraction (i.e. 17.7% extra energy for the case without versus 17.66% for the case with box constraints, averaged over the first control window).

For the optimal receding-horizon control cases considered here, an optimization time horizon $T = 280$s is selected. This corresponds to approximately 0.4 times the through-flow time, or the average convection time taken for the flow to pass 4 rows of turbines. In this way, it is possible to avoid any interaction between the optimal control approach and the periodicity of the streamwise boundary

conditions. Once the optimization of the controls is converged, they are used for $T_A = 140$s, before the next optimization problem is started. This process is repeated for a total of 25 control windows, totalling to 3500s (approx. 1h) of wind-farm operation. Every optimization time horizon (except the first one) uses the flow field at the end of the previous control window as an initial field and $C'_{T,i}(t) = 1.33$ as the starting control values for all turbines. As discussed earlier, for the first optimization time horizon, a statistically stationary field of an uncontrolled wind-farm simulation is used as an initial field.

Finally, in order to limit computational costs, neither the CG algorithm nor the line-search algorithms are fully converged. Instead, the optimization is stopped after 5 CG iterations, and a maximum of 3 line-search iterations per CG iteration. This leads to approximately 45 PDE simulations per control window, or about 1125 PDE simulations in total, where one PDE simulation takes approximately 90 minutes of wall time on 32 processors.

In figure 4.1, a typical convergence history of an optimization (for an unpenalized cost functional) for three different control windows is shown. On the x-axis, the number of successive PDE simulations during the iterative CG optimization algorithm is shown. Closed symbols refer to standard LES, while open symbols refer to adjoint simulations. It is appreciated that the cost function does not decrease monotonically with the number of simulations. This is related to the line-search algorithm (cf. §3.3) that sometimes overshoots the optimal step length along a CG search direction. In figure 4.1, it is appreciated that the cost functional decreases significantly during the optimization in each control window. But since the optimization is stopped after 5 CG iterations, it is not formally converged to $\nabla\tilde{\mathscr{J}} = 0$.

4.2 Optimal control without penalization

In this section, optimal control results are presented for the wind-farm control case in which the cost functional is simply the amount of energy extracted by the farm (i.e. Eq. (3.1)), and has no penalization term. First, some characteristics of the adjoint solution and the controls are shown in §4.2.1. Subsequently, a detailed analysis of energy budgets in the wind-farm boundary layer is presented in §4.2.2 and §4.2.3. Flow statistics are presented in §4.2.4 and compared to the uncontrolled case. Finally, in §4.2.5, the results are further discussed.

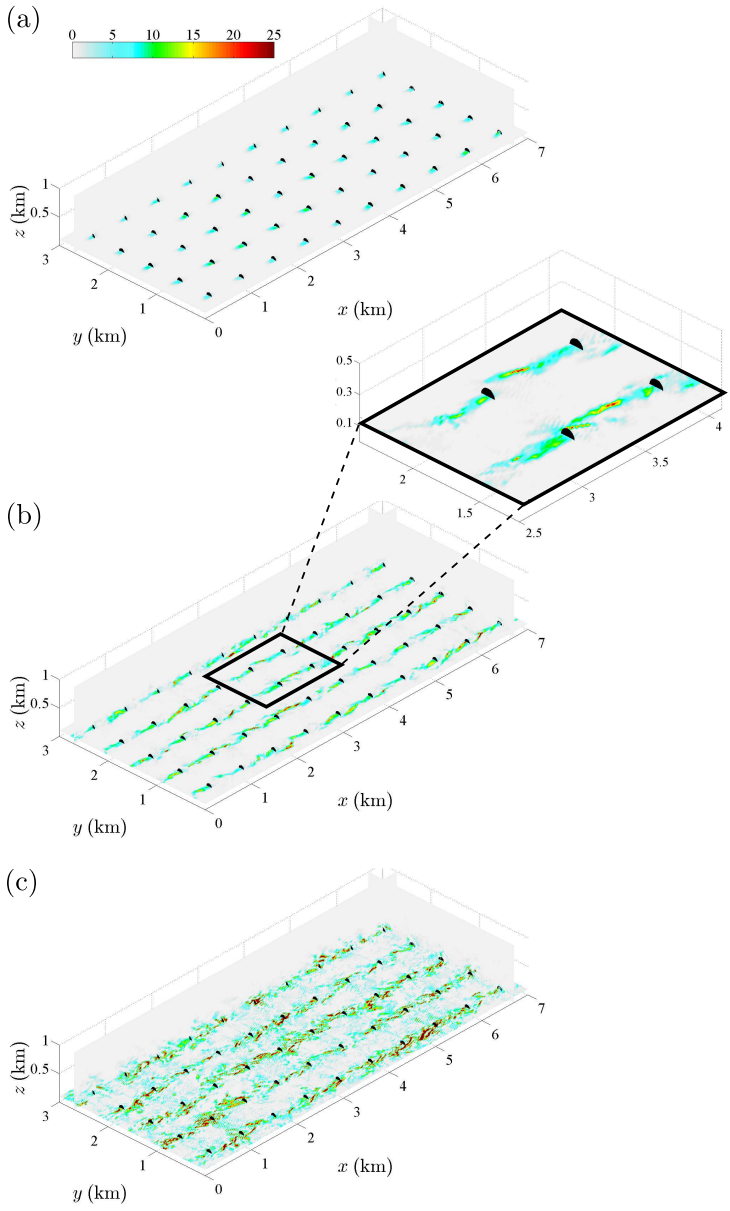

Figure 4.2: Contours of instantaneous streamwise adjoint fields. Horizontal planes in the figures are taken at the hub height. (a) $T-t = 14$s, (b) $T-t = 70$s, (c) $T - t = 174$s

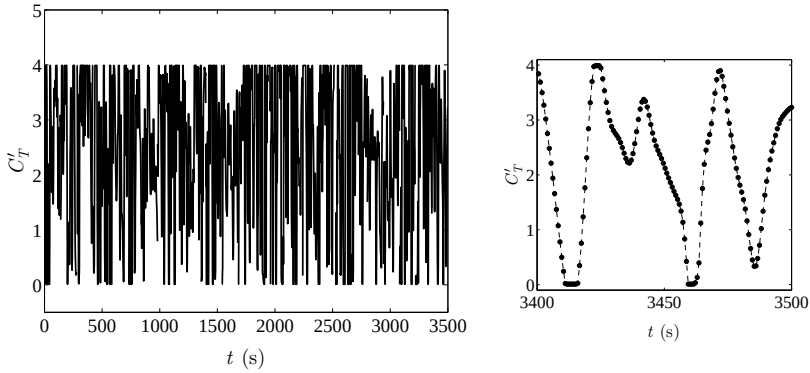

Figure 4.3: Time evolution of the thrust coefficient of one of the turbines in the farm.

4.2.1 Adjoint fields and optimal controls

In figure 4.2, snapshots of the instantaneous adjoint fields are shown. Unlike the flow field, the adjoint equations evolve backward in time and propagate in the upstream direction. The adjoint field depends strongly on the definition of the cost functional and the forward flow state around which the equations are linearized. The fields that are shown in figure 4.2 belong to the first adjoint equations in the optimization sequence of the first optimal control time horizon (see figure 3.1): at this point, the equations are linearized around a flow state that is obtained for initially constant controls at all turbines with $C'_{T,i}(t) = 1.33$ ($i = 1 \cdots N_t$). The initial condition for the adjoint equations corresponds to $\boldsymbol{\xi}(\boldsymbol{x}, T) = 0$. This is also visible in the first snapshot at $T - t = 14$ (figure 4.2 (a)), where the field is still largely zero.

The adjoint equations are driven by the cost function of the optimization problem (i.e. $\partial \mathscr{J} / \partial \boldsymbol{q}$ in 3.21). They essentially express where possible changes in the cost function $\mathscr{J}$ may be originating from (thus the equations evolve backwards in time and in the reverse flow direction). When looking at the first two snapshots in figure 4.2 (at $T - t = 14$, and $T - t = 70$), it can be seen that changes to the cost functional in the last time interval of the optimal control time horizon originate from a tube upstream of the turbine rotors. At this point, only changes to the flow velocity in this region affect the later energy extraction at the turbine rotor. When looking earlier in time ($T - t = 174$), the 'tube' observed in figure 4.2(b) 'hits' the previous row of turbines; hence, upstream turbines have the potential to influence the energy extraction of their downstream neighbours. Looking at figure 4.2(c) (at $T - t = 174$), it is observed

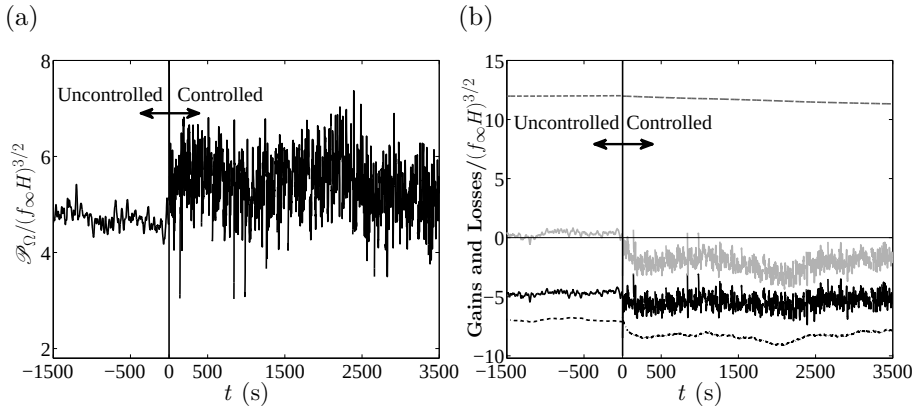

Figure 4.4: Time evolution of (a) total wind-farm power output, and (b) gains and losses. (- - -, grey dashed): driving power by pressure force; (——, grey): rate of change of kinetic energy; (——, black): farm power; (- · - · -, dot-dashed): dissipation.

that the adjoint field has become fully turbulent in the whole domain. This shows that it is the full interaction with the boundary layer that influences the wind-farm energy extraction.

In figure 4.3, the behavior of the optimal thrust coefficient is shown for one of the turbines in the controlled wind farm. Approximately 1h of time is shown, corresponding to 25 consecutive control windows. It is appreciated that C_T' changes strongly with time but remains limited by the box constraints used during the optimization (cf. §4.1). Zooming further into the figure reveals that the changes in C_T' are well resolved in time; no additional smoothing of the gradients used in the optimization was required for this. Moreover, typical time scales with which the controls change remain above 10 seconds.

4.2.2 Optimized power output

In the current subsection, the energy balance and power extraction are discussed in detail. In figure 4.4, the total wind-farm power extraction per unit wind-farm area $\mathscr{P}_\Omega$ $(= P/(L_x L_y))$ and the total gains and losses per unit area are shown. To this end, the total kinetic energy equation is horizontally averaged and integrated over the boundary layer height, leading to

$$\frac{\mathrm{d}E_\Omega}{\mathrm{d}t} \equiv \frac{\mathrm{d}}{\mathrm{d}t}\int_0^H \frac{1}{2}\langle \widetilde{\boldsymbol{u}}\cdot\widetilde{\boldsymbol{u}}\rangle_\Gamma \mathrm{d}x_3 = f_\infty U_b H - \mathscr{P}_\Omega - \mathscr{D}_\Omega, \tag{4.1}$$

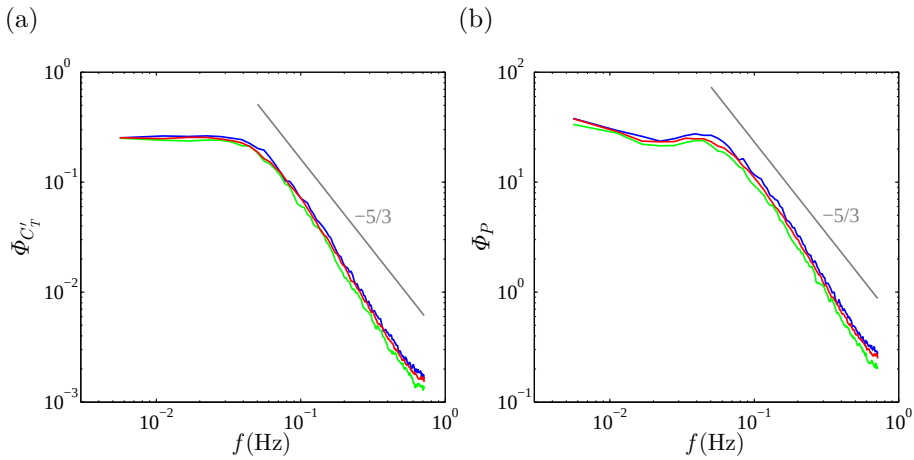

Figure 4.5: Frequency spectra of (a) thrust coefficient, and (b) power output for the controlled case averaged over all the turbines. (—, blue; —, red; —, green): respectively averaged over time windows $[0, 5T_A]$, $[5T_A, 20T_A]$, and $[20T_A, 25T_A]$.

where $\langle\cdot\rangle_\Gamma$ denotes horizontal averages, and the subscript Γ indicates that the averages are taken over a finite-domain horizontal plane $\Gamma \subset \Omega$. In contrast to $\mathscr{P}$ and $\mathscr{D}$ in §2.3, $\mathscr{P}_\Omega$, and $\mathscr{D}_\Omega$ are not averaged in time; therefore, they still fluctuate significantly from time step to time step (i.e. the horizontal extent of the domain is not large enough to obtain statistical convergence based on horizontal averaging only).

In figure 4.4(a), the power extraction is shown before ($t < 0$), and after the start of the optimal model predictive control. It is seen that the power extraction increases overall, but starts to fluctuate significantly more than before the coordinated optimal control. On average, a gain in energy extraction of 16% is achieved (integrated between $t = 0$ and $t = 3500$ sec). In figure 4.4(b), gains and losses to the boundary layer are shown. Here, the wind-farm power is plotted as a loss term, together with the dissipation $\mathscr{D}_\Omega$. It can be observed that the increase in power extraction is mainly balanced by an overall deceleration of the flow. In addition, the dissipation $\mathscr{D}_\Omega$ also increases (remember that the dissipation is not penalized, i.e. $\gamma = 0$).

In figure 4.4(b), the driving power $f_\infty U_b H$ is also plotted. It is observed that the driving power slowly decreases during the optimal control. This is directly related to the fact that f_∞ is kept constant during the optimization, while the flow slowly decelerates. Returning to the discussion in §2.3, it is remarked here

that $f_\infty U_b H$ is not explicitly kept constant during the optimization. This would require adding a non-trivial state constraint to Eq. (3.4), requiring the solution of an additional set of adjoint equations for every gradient evaluation. However, it is appreciated that changes in the driving power remain small. Moreover, it is also remarked that the average level of C_T' in the optimal control is moving to higher values, and thus away from the constant C_T' optimum observed in figure 2.6 for the constant-forcing case. This clearly indicates that the optimal controls found here do not lead to a statistically stationary optimal situation, but instead purely exploit transient boundary-layer deceleration.

Figure 4.5 shows the frequency spectra of the thrust coefficient and the turbine power output. The spectra presented in the figures are first averaged over all the turbines in the farm and further averaged over the control windows. It is observed that both C_T' (figure 4.5(a)) and the turbine power (figure 4.5(b)) have a slope of approximately $-5/3$ in the frequency range from 0.06 to 0.2 Hz. A similar power-law behavior was also observed for the farm power output by Stevens *et al.* [98] in their LES investigation. For frequencies below 0.05 Hz, the spectrum of the C_T' is almost constant, without any slope. However, in the power output spectrum, a small peak can be observed around 0.05 Hz before the slope transitions from -5/3 to -0.5 in the lower frequency range.

4.2.3 Energy balance in the turbine region

The energy balances in the wind farm are further investigated. To smoothen results, they are additionally integrated per control window T_A. In addition to the balance integrated over the whole height of the computational domain Ω (cf. 4.1), the balance in the turbine region i.e. integrated from $z_h - D/2$ to $z_h + D/2$, is also investigated. This horizontal slab of the computational domain is denoted with Ω_D and is schematically represented in figure 4.6 (note that for numerical evaluation, slightly wider integration bounds are taken to ensure that all filtered turbine forces (cf. Eq. (2.7)) are included in Ω_D).

The following notation is used for the horizontal and time average (here for $\widetilde{\boldsymbol{u}}$)

$$\overline{\langle \widetilde{\boldsymbol{u}} \rangle_\Gamma}^{T_A} = \frac{1}{T_A L_x L_y} \int_{nT_A}^{(n+1)T_A} \int_0^{L_y} \int_0^{L_x} \widetilde{\boldsymbol{u}} \, \mathrm{d}x_1 \mathrm{d}x_2 \mathrm{d}t, \tag{4.2}$$

using $\overline{\cdot}^{T_A}$ to denote the time average over a time window with length T_A. Moreover, the following definitions are used: $\widetilde{\boldsymbol{u}}'' = \widetilde{\boldsymbol{u}} - \overline{\langle \widetilde{\boldsymbol{u}} \rangle_\Gamma}^{T_A}$, $e = \widetilde{\boldsymbol{u}} \cdot \widetilde{\boldsymbol{u}}/2$, and $e'' = e - \overline{\langle e \rangle_\Gamma}^{T_A} = \widetilde{\boldsymbol{u}}'' \cdot \widetilde{\boldsymbol{u}}''/2 + \widetilde{\boldsymbol{u}}'' \cdot \overline{\langle \widetilde{\boldsymbol{u}} \rangle_\Gamma}^{T_A}$. The energy balance for Ω_D is then

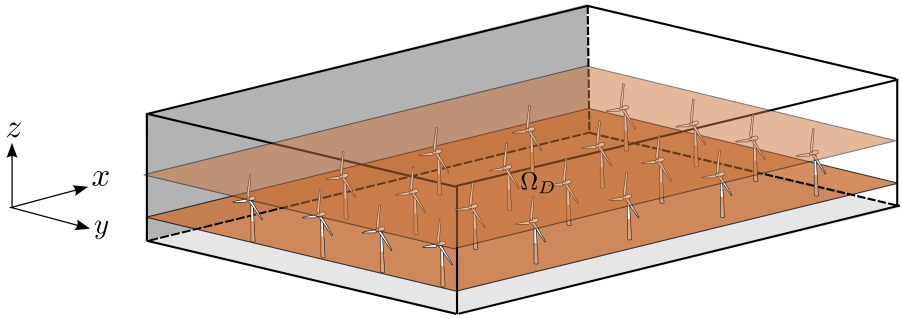

Figure 4.6: Schematic of the computational domain with horizontal slab Ω_D in the turbine region.

expressed as

$$\begin{aligned}\frac{\Delta E_{\Omega_D}}{T_A} &\equiv \int_{z_h-D/2}^{z_h+D/2} \overline{\langle \mathrm{d}e/\mathrm{d}t\rangle_\Gamma}^{T_A}\,\mathrm{d}x_3 \\ &= \underbrace{-\overline{\langle \widetilde{u}_3''(e''+p''/\rho)\rangle_\Gamma}^{T_A}\Big|_{z_h-D/2}^{z_h+D/2}}_{\overline{T}''(z+D/2)-\overline{T}''(z-D/2)} + \underbrace{\int_{z_h-D/2}^{z_h+D/2} f_\infty \overline{\langle \widetilde{u}_1\rangle_\Gamma}^{T_A}\,\mathrm{d}x_3}_{\mathscr{F}_{\Omega_D,T_A}} \\ &\quad \underbrace{+\int_{z_h-D/2}^{z_h+D/2} \overline{\langle \boldsymbol{f}\cdot\widetilde{\boldsymbol{u}}\rangle_\Gamma}^{T_A}\,\mathrm{d}x_3}_{\mathscr{P}_{\Omega_D,T_A}=\mathscr{P}_{\Omega,T_A}} \underbrace{-\int_{z_h-D/2}^{z_h+D/2} \overline{\langle \boldsymbol{\tau_M}:\nabla\widetilde{\boldsymbol{u}}\rangle_\Gamma}^{T_A}\,\mathrm{d}x_3}_{\mathscr{D}_{\Omega_D,T_A}}, \end{aligned} \tag{4.3}$$

further introducing the following notation: turbulent (and dispersive) transport $\overline{T}''$, driving power $\mathscr{F}_{\Omega_D,T_A}$, wind-farm power extraction $\mathscr{P}_{\Omega,T_A}$, and dissipation $\mathscr{D}_{\Omega_D,T_A}$, all per unit wind-farm area. The terms of equation (4.3) are plotted in figure 4.7(b). For reference, in figure 4.7(a), the same terms are shown integrated for the whole domain: this corresponds to the balance shown in figure 4.4(b), but in addition averaged in time per control window.

From figure 4.7(b), it is observed that the turbine region is in equilibrium for $t \geq 5T_A$, i.e. in this region $\Delta E_{\Omega_D}(t)$ is approximately zero. The farm power extraction is the largest sink in this region, followed by the dissipation, which amounts to 37% of the dissipation in the whole boundary layer. The main source of energy is the turbulent transport $\overline{T}''(z+D/2)$ at the top boundary of the region.

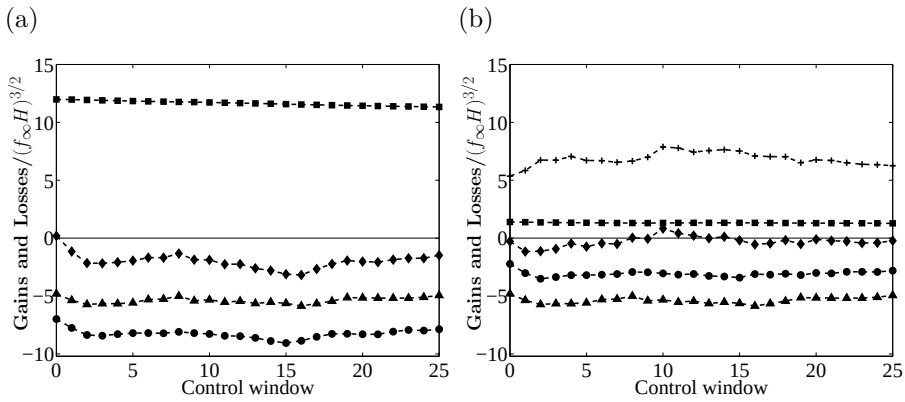

Figure 4.7: Gains and losses per unit wind-farm area averaged over control windows for (a) the whole computation domain Ω, (b) the disk region Ω_D. (⧫): rate of change of kinetic energy $\Delta E_\Omega/T_A$; (■): driving power $\mathscr{F}_{\Omega,T_A}$; (▲): wind-farm power extraction $\mathscr{P}_{\Omega,T_A}$; (•): dissipation $\mathscr{D}_{\Omega,T_A}$; (+): total transport $\overline{T}''(z+D/2)-\overline{T}''(z-D/2)$.

The results in figure 4.7 suggest that the inner region of the boundary layer reaches a new statistical equilibrium after roughly 5 control windows (which is roughly equivalent to one through-flow time period), and only the outer layer decelerates. Moreover, the energy is transported from the outer region towards the turbine region by increased turbulent and dispersive transport. This is further investigated next.

4.2.4 Flow profiles in the controlled wind farm

In the current subsection, time-averaged and horizontally averaged profiles are investigated. First of all, the streamwise velocity profile averaged over five different time windows, i.e. corresponding to the windows $[5(n-1)T_A, 5nT_A]$, with $n = 1 \cdots 5$, are shown in figure 4.8 together with the velocity profile for the uncontrolled case. For all cases, two distinct logarithmic regions – one above and one below the turbines – are observed. This is consistent with observations by Calaf *et al.* [16], and Cal *et al.* [15] for uncontrolled wind farms (see also §2.2.2). The control in the current work does not change these features. It is further observed in figure 4.8 that the velocity profile for the controlled cases are lower than that for the uncontrolled case. When looking at the inner layer ($z/H < 0.15$), it is seen that the velocity profiles of the middle three averages cluster around a new equilibrium position (see inset in the figure). The first

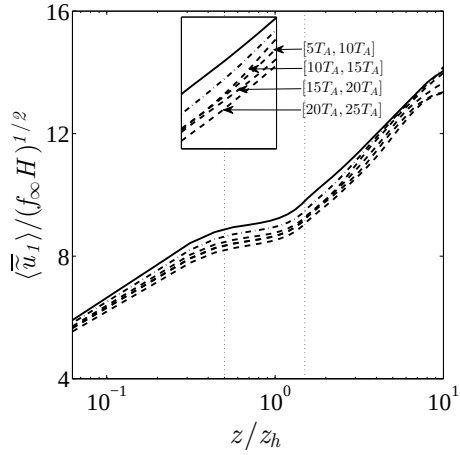

Figure 4.8: Streamwise mean velocities. (——): uncontrolled case; (- · - · -): optimal control case averaged over the time interval $[0, 5T_A]$; (- - -; see also inset): averaged over later intervals.

average $[0, 5T_A]$ is found to be somewhat higher (closer to the uncontrolled case), while the last average $[20T_A, 25T_A]$, is somewhat lower than the three previous averages. For the current case, the optimal control was pushed a bit further, i.e. up to 33 control windows (results not shown in the plots), and this further confirms that the inner layer starts to decelerate again after 20 to $25T_A$. When looking higher up in the wind-farm boundary layer and close to the top, it is appreciated that the velocity profiles keep decreasing in all control windows. This is consistent with the observations in figure 4.7. Therefore, for analysis of higher-order moments, averages over the middle time window $[5T_A, 20T_A]$ are mainly shown, which extends over 35 minutes of wind-farm operation during which it is presumed that the flow is in statistical equilibrium in the inner layer.

In figures 4.9 and 4.10, the total, dispersive, and Reynolds stresses are shown for the different cases. Remember that these stresses are constructed based on horizontal averages over a domain that is horizontally periodic, but not homogeneous. Figure 4.9 shows the total shear stress averaged over different windows in the controlled case and for the uncontrolled case. For the latter, it is seen that $-\langle \widetilde{u}_1'' \widetilde{u}_3'' \rangle = (1 - z/H) f_\infty H$ above the turbines, as can be expected from the plane-averaged momentum balance in a conventional channel-flow boundary layer. Below the turbine level, the turbine forces and subgrid-scale stresses (close to the wall) take over the role of the turbulent shear stress in the total balance.

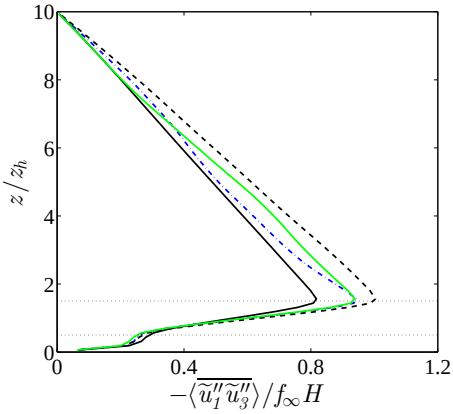

Figure 4.9: Vertical profiles of total stresses. (——, black): uncontrolled case; (-·-·-, blue dot-dashed; - - -, dashed; ——, green): controlled case respectively averaged over time windows $[0, 5T_A]$, $[5T_A, 20T_A]$, and $[20T_A, 25T_A]$.

Looking at the total shear stresses $\langle\widetilde{\widetilde{u}_1''}\widetilde{\widetilde{u}_3''}\rangle$ for the controlled cases in figure 4.9, the picture changes. Now, the boundary layer is no longer in equilibrium, so $u_{\tau h} \neq f_\infty H$, but rather

$$u_{\tau h} = f_\infty H - \frac{\mathrm{d}U_b}{\mathrm{d}t}, \tag{4.4}$$

where $-\mathrm{d}U_b/\mathrm{d}t$ is the deceleration of the bulk flow. Since $\mathrm{d}U_b/\mathrm{d}t$ is roughly constant for $t \in [5T_A, 20T_A]$ (cf. figure 4.7), it can be expected that $u_{\tau h}$ is also roughly constant in this region, but higher than $f_\infty H$. This is observed in figure 4.9 for the average over the interval $[5T_A, 20T_A]$. Note that for this case, the deceleration is mainly taking place in the outer layer of the boundary layer, while the inner layer ($z/H < 0.15$) is in a new equilibrium (cf. discussion above). For the average over $[0, 5T_A]$, this is not yet the case, and this is also apparent from figure 4.9.

In figure 4.10, the total stresses (both the shear stress and the normal stresses) are further decomposed into dispersive stresses ($\langle\widetilde{\widetilde{u}_i''}\widetilde{\widetilde{u}_j''}\rangle$) and plane-averaged Reynolds stresses ($\langle\widetilde{\widetilde{u}_i'}\widetilde{\widetilde{u}_j'}\rangle$), averaged over the time window $[5T_A, 20T_A]$, i.e. (e.g. following [16]) $\langle\widetilde{\widetilde{u}_i''}\widetilde{\widetilde{u}_j''}\rangle = \langle\widetilde{\widetilde{u}_i''}\widetilde{\widetilde{u}_j''}\rangle + \langle\widetilde{\widetilde{u}_i'}\widetilde{\widetilde{u}_j'}\rangle$, with $\widetilde{u}_i' = \widetilde{u}_i - \overline{\widetilde{u}}_i$. First of all, in figure 4.10(a), it is very interesting to notice that the increase in total stress is caused by an increase in dispersive shear stresses, which are roughly doubled, while the plane-averaged Reynolds stresses decrease. The same trends are observed in figure 4.10(b) for the streamwise stresses: the dispersive stresses increase significantly, but the Reynolds stresses decrease. For the spanwise, and vertical stresses, the dispersive stresses also increase significantly. However, the

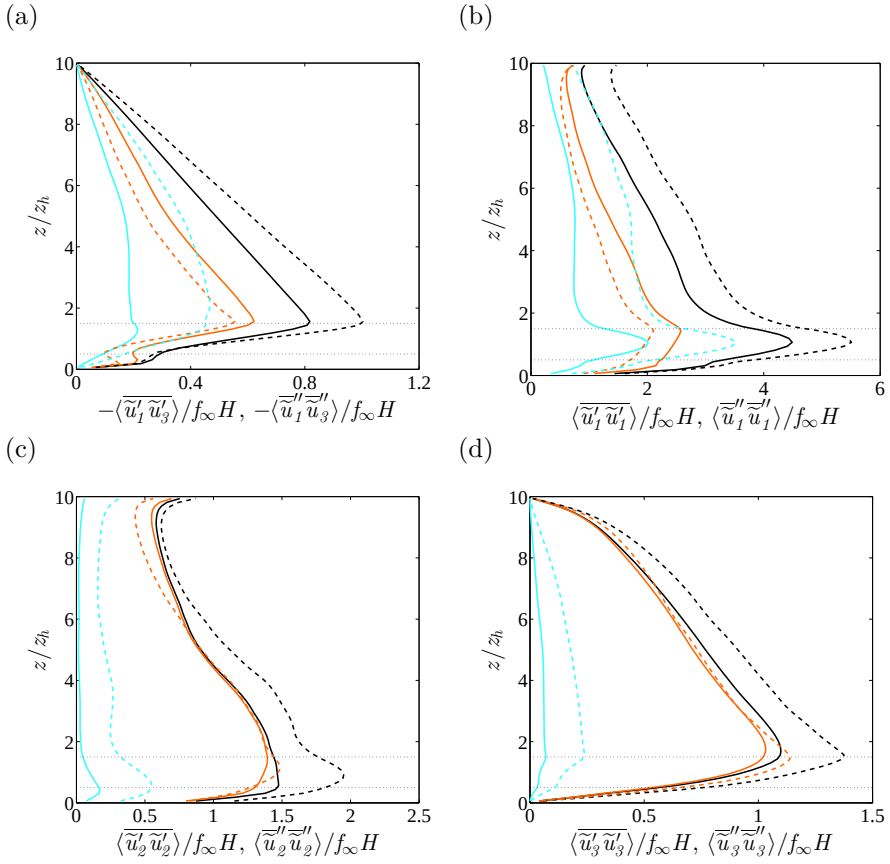

Figure 4.10: Vertical profiles of total, Reynolds and dispersive stresses. (——, black; ——, orange; ——, cyan): respectively total stresses, Reynolds stresses, and dispersive stresses for the uncontrolled case. (- - -, dashed; - - -, orange dashed; - - -, cyan dashed): respectively total stresses, Reynolds stresses, and dispersive stresses for the controlled case averaged over $[5T_A, 20T_A]$.

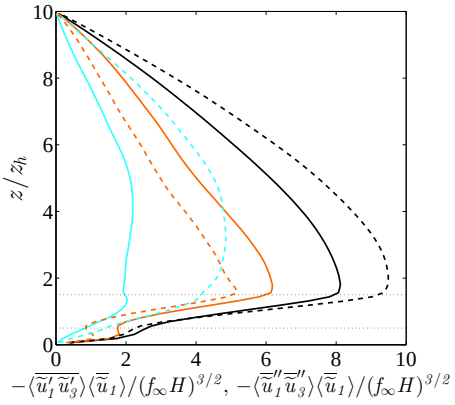

Figure 4.11: Vertical profiles of horizontally averaged mean-flow kinetic energy flux. Uncontrolled case, (——, black): total kinetic energy flux; (——, orange): flux due to Reynolds stress; (——, cyan): flux due to dispersive stress. The optimal control case averaged over time window $[5T_A, 20T_A]$, (- - -, dashed): total kinetic energy flux; (- - -, orange dashed): flux due to Reynolds stress; (- - -, cyan dashed): flux due to dispersive stress.

Reynolds stresses remain largely unchanged, except in the turbine-tip region, where they slightly increase.

Looking at the fluxes of horizontally averaged mean-flow energy in figure 4.11, the same trends are observed. It is seen that the energy flux at the top of the farm ($z = z_h + D/2$) is considerably higher for the controlled case than for the uncontrolled case. Below the farm, the inverse is observed. Here, the energy flux towards the flow below the farm is lower compared to the uncontrolled case. Thus, as a result of the optimal control, the energy flux towards the farm increases, while at the same time, this energy is better captured by the turbines. We also further looked at the total kinetic energy fluxes (not shown here), which contain additional elements of triple dispersive correlations and turbulent and pressure diffusion, but these are minor effects, and differences to the fluxes in figure 4.11 are small.

In order to further understand the increase in dispersive stresses and decrease in Reynolds stresses observed above, the velocity and stresses averaged in time and over the 10×5 turbine subdomains (each with horizontal size $S_x \times S_y$) are analyzed next. First of all, in figures 4.12(a, b), the mean streamwise velocity is shown in a horizontal plane at the hub level. It is appreciated that the inflow velocity of the turbines in the controlled and uncontrolled cases is more or less the same. However, the wake velocity in the controlled case is much lower than

for the uncontrolled case, which is clearly related to the fact that more energy is extracted in the controlled case. In spite of the lower wake velocity in the controlled case, the wake recovers faster than the uncontrolled wake. This is also visible in figures 4.12(c, d), where the streamwise velocity is shown in a vertical–streamwise plane through the turbine center. Here, it is appreciated that over the rotor height, the turbine inflow in the controlled case is even a bit higher than for the uncontrolled case. In figures 4.12(e, f), a vertical streamwise plane of $-\widetilde{\overline{u}}_1''\widetilde{\overline{u}}_3''$ is shown, which contributes to the dispersive shear stress (i.e. $-\langle\widetilde{\overline{u}}_1''\widetilde{\overline{u}}_3''\rangle$) when averaged over the horizontal planes. It is observed that positive $-\widetilde{\overline{u}}_1''\widetilde{\overline{u}}_3''$ regions increase in strength for the controlled case, while negative regions are not altered much. Given the distribution of the horizontal velocity in figures 4.12(c, d), it is clear that these positive $-\widetilde{\overline{u}}_1''\widetilde{\overline{u}}_3''$ regions are associated with a correlation of low mean streamwise velocity with upward mean motion. In the high-speed channels between the turbines (not shown here), an increased positive $-\widetilde{\overline{u}}_1''\widetilde{\overline{u}}_3''$ correlation is observed in the controlled case, which is here associated with high mean streamwise velocity transported downward by mean negative vertical motion.

In figures 4.13 and 4.14, the Reynolds stresses are further investigated in a turbine subdomain. In figures 4.13(a,b), the Reynolds shear stresses are shown in a horizontal plane through the turbine rotor tip (this is the region where the Reynolds stresses are largest in figure 4.10). It is observed that in the controlled case, the Reynolds shear stresses increase significantly above the turbine-wake region, which can explain the faster wake recovery observed in figure 4.12(b). On average, the increased effect of Reynolds shear stresses is compensated by lower shear stresses in the regions between the turbine rows when comparing controlled and uncontrolled cases, leading to lower horizontally averaged values (cf. figure 4.10(a)). Also, in a vertical plane (figures 4.13 (c), (d)), it is appreciated that Reynolds shear stresses increase significantly in the wake region for the controlled case. However, they do not increase in front of the turbine.

In figures 4.14 (a, b), the streamwise component of the normal Reynolds stresses are shown in a horizontal plane through the turbine rotor tip. Figures 4.14 (c –h) show all three components of the normal Reynolds stresses in a vertical plane. All normal stresses increase significantly in the wake region for the controlled case. When looking 1D upstream of the turbine, it can be observed that the streamwise stresses $\overline{\widetilde{u}_1'\widetilde{u}_1'}$ decrease in the controlled case compared to the uncontrolled case. This is possibly beneficial for reducing turbine loading and local blade stall (cf. also discussion in §3.2). The spanwise stresses $\overline{\widetilde{u}_2'\widetilde{u}_2'}$ remain roughly unchanged in front of the turbine, while the vertical stresses $\overline{\widetilde{u}_3'\widetilde{u}_3'}$ slightly increase. Nevertheless, overall, compared to the uncontrolled case,

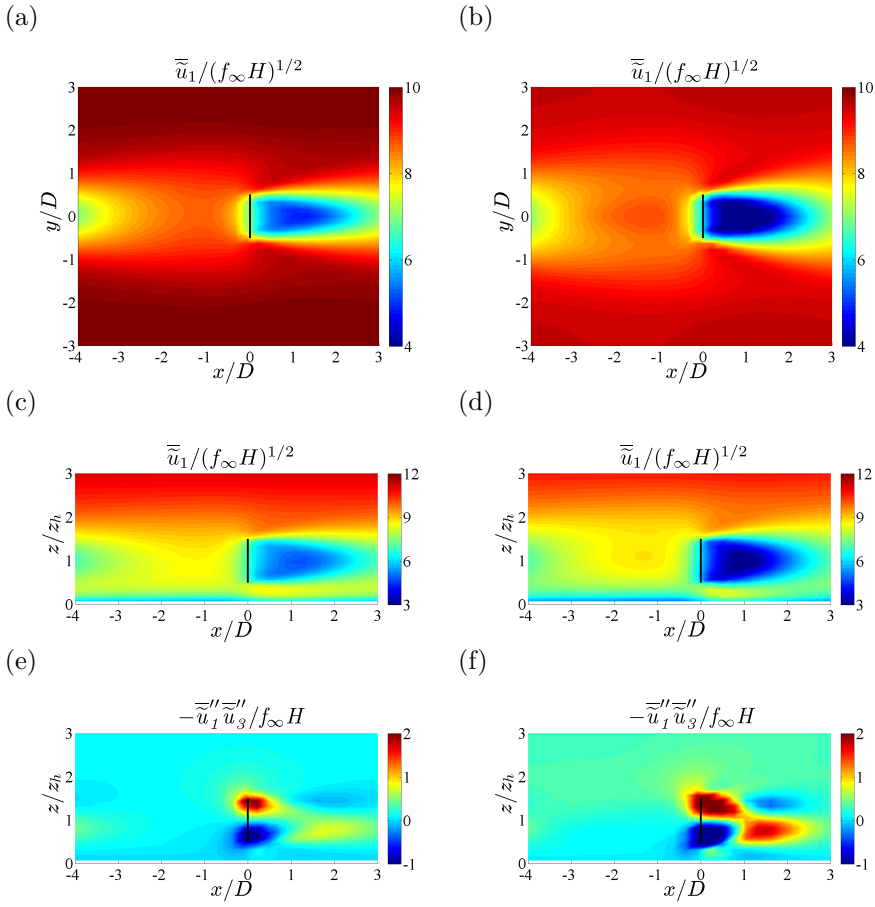

Figure 4.12: (a–d) Contours of mean streamwise velocity field averaged over control windows and turbine elements; (a,b) in a horizontal plane through the hub; (c,d) in a vertical plane through the turbine. (e,f): Contours of $\overline{\widetilde{u}}_1''\overline{\widetilde{u}}_3''$ in a vertical plane through the turbine. (left)(a,c,e): uncontrolled case; (right)(b,d,f): the optimal control case averaged over time window $[5T_A, 20T_A]$.

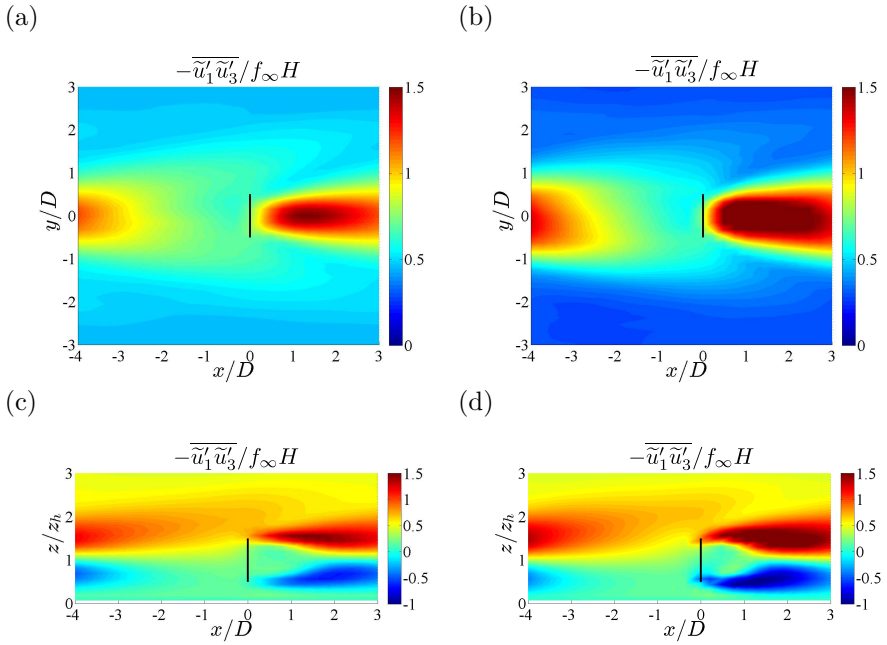

Figure 4.13: Contours of Reynolds shear stresses averaged over control windows and turbine elements. (a, c): uncontrolled case; (b, d): the optimal control case averaged over time window $[5T_A, 20T_A]$. Figures (a) and (b) show a horizontal plane at the turbine-tip level; while (c) and (d) show xz–planes through the rotor center.

the turbulent kinetic energy $\overline{\widetilde{u}_i'\widetilde{u}_i'}/2$ in the controlled case decreases by almost 9% in front of the turbines (measured 1D upstream). It should be remarked that the simulations in this dissertation do not resolve turbulent fluctuations on the size of the turbine blade chord. It has been demonstrated experimentally that the energy exchange is dominated by turbulent scales with sizes similar to the rotor diameter [42]. However, smaller scales can be very relevant for the local blade performance, e.g. having an effect on local blade stall. In a classical turbulent energy cascade, it is expected that such smaller scales follow the larger scales (that are here resolved), but this has to be further established using better turbine representations (e.g. using actuator line models) and finer resolutions. This is a subject of further research (cf. discussion in Chapter 6).

Given the fact that the turbulence levels decrease in front of the turbines, the increased fluctuations in power output observed in figure 4.4 all result from fluctuations in the control C_T'. It is possible to make a Reynolds decomposition

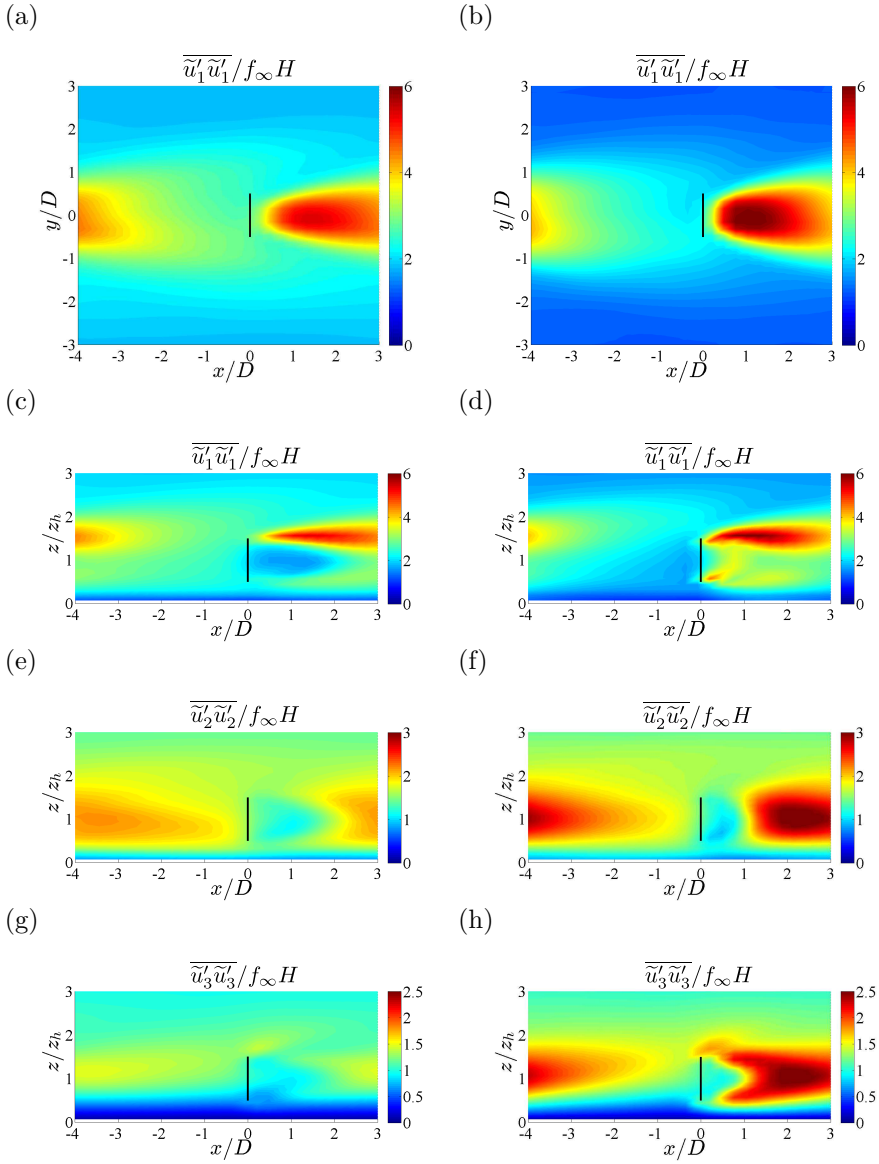

Figure 4.14: Contours of normal Reynolds stresses averaged over control windows and turbine elements. (a,c,e,g): uncontrolled case; (b,d,f,h): the optimal control case averaged over time window $[5T_A, 20T_A]$. Figure (a) and (b) show a horizontal plane at the turbine-tip level; while (c–h) show xz–planes through the rotor center.

of the extracted power, using (2.12) and defining $C'_{T,i} \equiv \overline{C'_{T,i}} + \Delta[C'_{T,i}]$ and $\widehat{V}_i^2 V_i \equiv \overline{\widehat{V}_i^2 V_i} + \Delta[\widehat{V}_i^2 V_i]$. Thus,

$$P = \sum_{i=1}^{N_t} \frac{1}{2} \overline{C'_{T,i}}\ \overline{\widehat{V}_i^2 V_i} A + \sum_{i=1}^{N_t} \frac{1}{2} \Delta[C'_{T,i}]\ \Delta[\widehat{V}_i^2 V_i] A. \tag{4.5}$$

In the uncontrolled case, the second term on the right-hand side is zero. In the controlled case, it is found that C'_T is slightly anticorrelated with $\widehat{V}_i^2 V_i$, leading to a negative value for the second term, with an observed magnitude that is approximately 6% of the total extracted power P (the first term on the right-hand side is 106% of P). Consequently, the second term is a source in the turbulent kinetic energy equation. This may explain the locally increased turbulence levels observed in the turbine wakes above.

4.2.5 Discussion

As shown above, the average power extraction by the wind farm increases by 16% averaged over $[0, 25T_A]$, corresponding to 1 hour of wind-farm operation. This directly results from a large increase in the vertical transport of energy by dispersive stresses, together with a local increase of Reynolds stresses in the wake region of the turbines.

In the current set-up, the increased transport of energy towards the inner layer cannot be sustained by the driving power, and the outer layer decelerates. Thus, it is clear that it will not be possible to sustain these increased levels of power extraction indefinitely. However, for boundary layers that are characterized by a top boundary condition with entrainment, such as developing internal boundary layers above finite farms, or shallow atmospheric boundary layers, the situation may be entirely different. In such cases, entrainment is typically proportional to $u_{\tau h}^2$, such that increased levels of inner-layer vertical transport may well be sustained by higher entrainment levels at the BL top. Note for instance, that for a finite farm with an extent of 20km, the characteristic through-flow time at a wind-speed of 10m/s corresponds to approximately 30 minutes, which is in the same order of magnitude as the sustained inner-layer equilibrium realized in the current case, so BL entrainment may not even need to fully compensate for increased wind-farm extraction. This discussion is very speculative, but given the current results, it points to very promising tracks for future research.

Finally, even in a BL context without entrainment at the top, a temporary increase of power extraction by 16% over a period of 1 hour, as covered in figure 4.4, is potentially quite relevant in the context of ancillary services

for the power grid, where reserve power is often required for similar time spans. Moreover, for a shorter time interval covering the first 12 minutes only ($[0, 5T_A]$), which is also relevant for ancillary services, power extraction increases by even 19%.

4.3 Optimal control with penalization of turbulent dissipation

This section presents the optimal control results for a wind-farm optimal control case where turbulent dissipation is penalized, i.e. using the cost functional defined by Eq. (3.2) and $\gamma \neq 0$. As observed in the previous section for the unpenalized case, optimal control leads to a deceleration of the boundary layer, and over the length of the optimal control wind-farm simulations (i.e. $t \in [0, 25T_A]$), convergence to a new statistical equilibrium could not be achieved. Moreover, even if the system is converged by continuing the procedure further in time, it is not expected that a problem formulation with $\gamma = 0$ would lead to good optimum solutions for such a new stationary equilibrium. To that end, the length of the optimal control time horizon T, which is limited by practical restrictions (cf. §4.1), is much too short compared to the slow dynamics of the boundary layer. Therefore, in the current section, turbulent dissipation is penalized with the aim of triggering different overall energy balances that possibly force the flow much faster into a new equilibrium, while also improving the ratio $\mathscr{P}/\mathscr{D}$. Two different penalties, $\gamma = 1/2$ and $\gamma = 2/3$, are used. From Eq. (3.2), it is seen that $\gamma = 1/2$ corresponds to giving an equal weight to decreasing dissipation and increasing power extraction, while $\gamma = 2/3$ gives a double weight to decreasing dissipation.

Below, some features of the adjoint solution and the optimal controls are first presented in §4.3.1. Subsequently, energy balances are discussed in §4.3.2, and mean profiles are presented in §4.3.3.

4.3.1 Adjoint solutions and optimal controls

In figure 4.15, snapshots of instantaneous adjoint fields are shown for $\gamma = 2/3$. As opposed to the adjoint fields for the unpenalized case (cf. figure 4.2), in the current case, the initial condition for the adjoint equations differs from zero and corresponds to $\boldsymbol{\xi}(\boldsymbol{x}, T) = 2/3\boldsymbol{u}(\boldsymbol{x}, T)$ instead. This is visible early in the adjoint simulation in figure 4.15(a). As with figure 4.2, the snapshots at $T - t = 14$s and $T - t = 70$s show that changes to the cost functional originate from a tube upstream of the rotors. On the other hand, for the snapshot at an

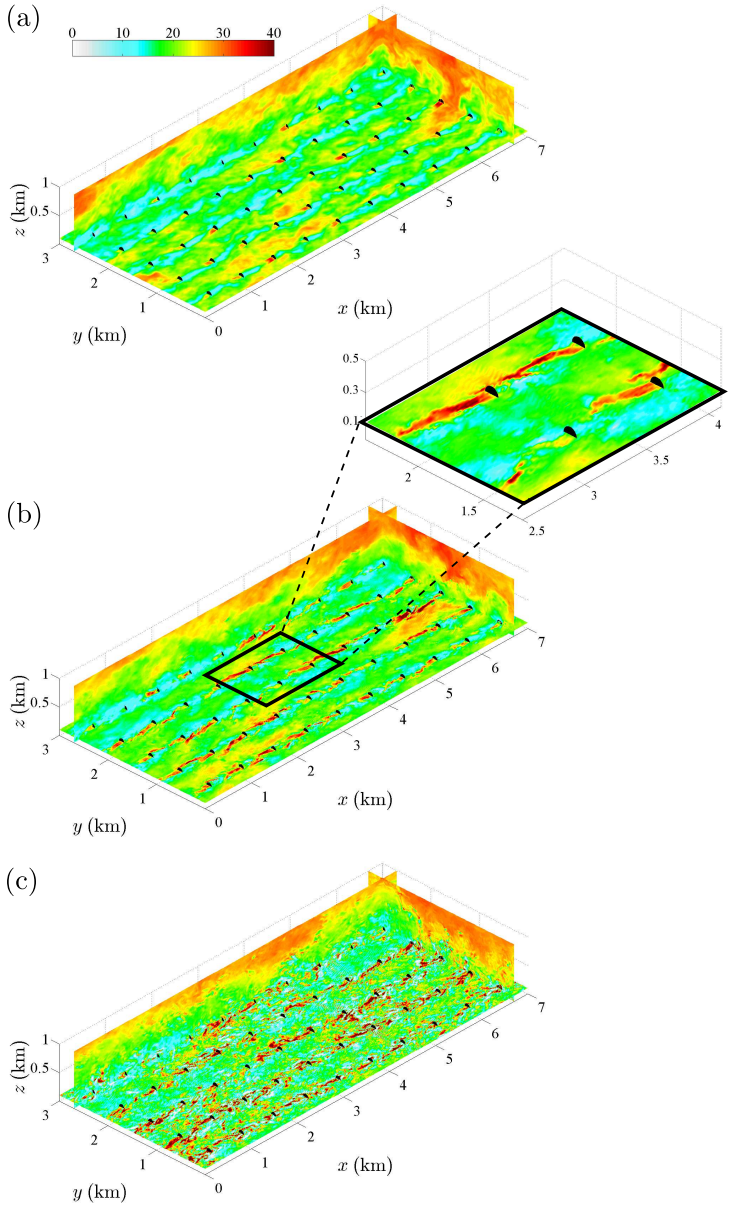

Figure 4.15: Contours of instantaneous streamwise adjoint field for $\gamma = 2/3$, obtained from the first gradient calculation in control window 1. Horizontal planes in the figures are taken at the hub height. (a) $T-t = 14$s, (b) $T-t = 70$s, (c) $T - t = 174$s

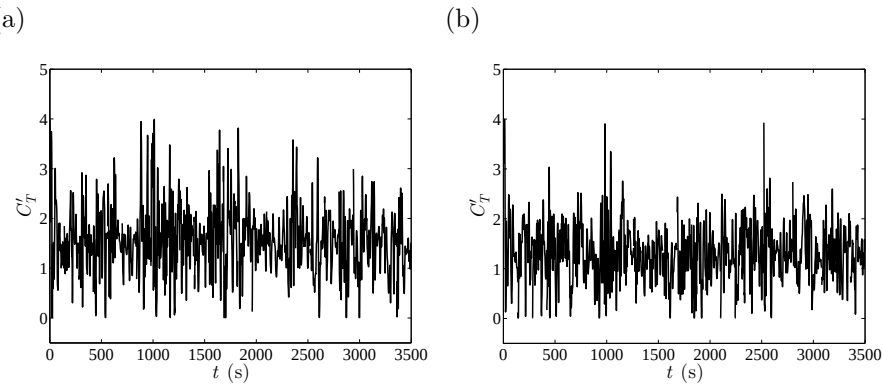

Figure 4.16: Time evolution of the thrust coefficient of one of the turbines in the farm. (a) $\gamma = 1/2$, (b) $\gamma = 2/3$.

earlier time ($T - t = 174$s), the tube hits the upstream turbines, showing that the power generation in a wind farm is influenced by the interactions between turbines.

Figure 4.16 shows the behavior of the thrust coefficient for one of the turbines in the controlled wind farm. Both the $\gamma = 1/2$ and $\gamma = 3/2$ cases show a strong response to the turbulent flow field. However, in comparison to figure 4.3, the changes are less extreme. It can also be seen from this figure that C'_T mostly stays within the lower and upper limits, i.e. 0 and 4, although occasionally it still hits the upper bound.

4.3.2 Discussion of energy balances

Figures 4.17(a) and 4.17(b) show the time series of the total instantaneous gains and losses in the boundary layer for $\gamma = 1/2$ and $\gamma = 2/3$, respectively. It is appreciated in both cases that the overall deceleration of the boundary layer remains limited, and that the boundary layer even accelerates slightly in the optimal control case with $\gamma = 2/3$ for $t > 1000$. Also, in comparison to figure 4.4, it is observed that the dissipation does not increase much and the driving power remains almost constant for both $\gamma = 1/2$ and $\gamma = 2/3$.

In order to assess the precise gains and losses for the different cases, the time-integrated gains and losses are assembled in tables 4.1 and 4.2. Here, $\gamma = 0$ represents the unpenalized case discussed in the previous section. Time averaging is performed from $[0, 20T_A]$, i.e. the time window for which the

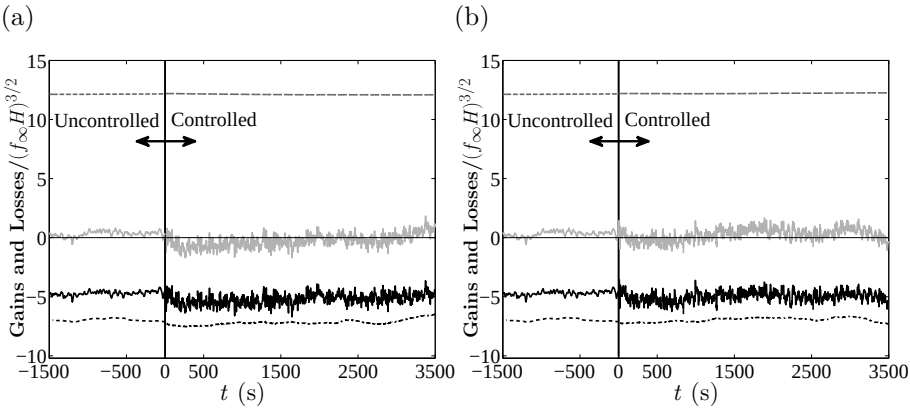

Figure 4.17: Time evolution of gains and losses. (a) $\gamma = 1/2$, (b) $\gamma = 2/3$. (- - -, grey dashed): driving power by pressure force; (——, grey): rate of change of kinetic energy; (——, black): farm power; (- · - · -, dot-dashed): dissipation.

inner layer of the $\gamma = 0$ case remains in equilibrium. The uncontrolled case is averaged over the same time window. First of all, in table 4.1, gains and losses are normalized with the total power extracted from the system by the wind-farm and the dissipation (i.e. $\mathscr{P} + \mathscr{D}$). Looking at the results in the table, it is observed that the respective contributions of $\mathscr{P}$ and $\mathscr{D}$ to the total energy extraction from the boundary layer differ only slightly for the different cases. For the $\gamma = 0$ case, which does not penalize dissipation, the ratio $\mathscr{P}/\mathscr{D} \approx 0.65$ deteriorates compared to the uncontrolled case for which $\mathscr{P}/\mathscr{D} \approx 0.68$. For the $\gamma = 1/2$ and $\gamma = 2/3$ cases, the ratios slightly improve, i.e. $\mathscr{P}/\mathscr{D} \approx 0.72$ for both cases. It should be remarked that for $\gamma = 2/3$, the ratio is slightly lower than for $\gamma = 1/2$ (cf. table), even though $\gamma = 2/3$ penalizes dissipation more. However, given the limited averaging time, this difference is probably not significant. Moreover, the cost functional (3.2) does not directly optimizing the ratio $\mathscr{P}/\mathscr{D}$.

In table 4.2, the relative gains (changes) compared to the uncontrolled reference case are listed. It is appreciated that all three cases increase the wind-farm power extraction compared to the uncontrolled reference. Also, the dissipation increases for the three cases, but much less for $\gamma = 1/2$ and $\gamma = 2/3$. Any increase in $\mathscr{P} + \mathscr{D}$ (compared to the reference) leads to an equal increase in the sum of the power input and energy balance – the latter is also listed in table 4.2. Only for the optimal control case with $\gamma = 2/3$, the total power extracted from the system remains close to that of the uncontrolled reference. The gain in wind-farm power extraction in this case is limited to 6%. Note

Table 4.1: Overview of gains and losses averaged over $[0, 20T_A]$ of different control cases normalized by total power extracted from the system (i.e. by $\mathscr{P} + \mathscr{D}$). As a result of normalization, both the sum of the left two columns and the sum of the right two columns add up to 100%.

	Power in	Balance	Power out	
	$f_\infty U_b H$	$-\mathrm{d}E/\mathrm{d}t$	$\mathscr{P}$	$\mathscr{D}$
No control ($C_T' = 1.33$)	101.1%	−1.1%	40.4%	59.6%
Control $\gamma = 0$	84.4%	15.6%	39.4%	60.6%
Control $\gamma = 1/2$	96.9%	3.1%	42.0%	58.0%
Control $\gamma = 2/3$	101.9%	−1.9%	41.8%	58.2%

Table 4.2: Overview of control gains, expressed in differences to the uncontrolled reference case, and averaged over $[0, 20T_A]$. Each difference is normalized by its respective uncontrolled property (e.g. $(\mathscr{P} - \mathscr{P}_{ref})/\mathscr{P}_{ref}$).

	Power in & Balance	Power out	
	$f_\infty U_b H - \mathrm{d}E/\mathrm{d}t$	$\mathscr{P}$	$\mathscr{D}$
Control $\gamma = 0$	+ 18.7%	+15.8%	+20.6%
Control $\gamma = 1/2$	+ 7.1%	+11.3%	+4.4%
Control $\gamma = 2/3$	+ 2.6%	+6.1%	+0.3%

that, if one were to presume a system that remained perfectly in equilibrium, a change of $\mathscr{P}/\mathscr{D}$ from 0.68 to 0.72 (cf. above) would then be equivalent to an increase in wind-farm power extraction of 5.8%.

Finally, it should be remarked that the order of magnitude of statistical errors in the discussion above is about 1% – this is appreciated from $\mathrm{d}E/\mathrm{d}t \neq 0$ for the uncontrolled case in table 4.1.

4.3.3 Averaged flow profiles

For both cases with penalization, the energy balances of Eq. 4.3 in the turbine disk region Ω_D are shown in figure 4.18. It is appreciated from the figures

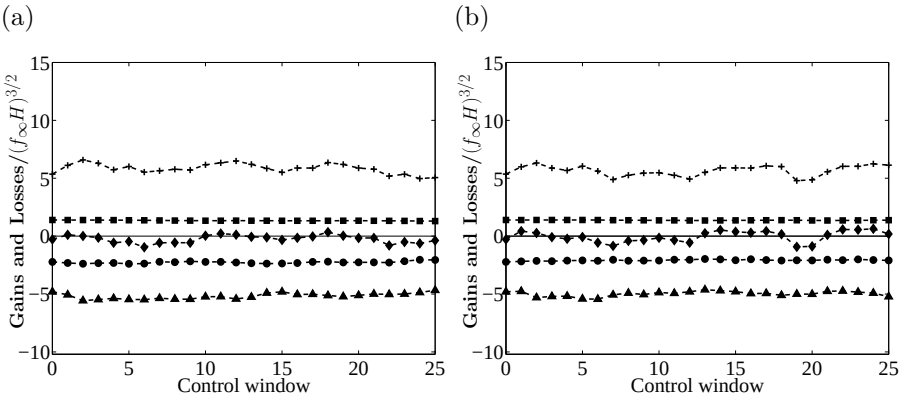

Figure 4.18: Gains and losses per unit wind-farm area for the disk region Ω_D, averaged over control windows. (a) $\gamma = 1/2$, (b) $\gamma = 2/3$. (⧫): rate of change of kinetic energy $\Delta E_{\Omega_D}/T_A$; (■): driving power $\mathscr{F}_{\Omega_D,T_A}$; (▲): wind-farm power extraction $\mathscr{P}_{\Omega,T_A}$; (●): dissipation $\mathscr{D}_{\Omega_D,T_A}$; (+): turbulent transport $T'(z + D/2) - T'(z - D/2)$.

that the turbulent transport at the top of the region is still the main source of energy, while the wind-farm power extraction is the dominant sink, followed by the dissipation. As with the case without penalization, it is observed that the inner region of the boundary layer reaches statistical equilibrium after a short transition period. To assess averaged flow profiles in the current section, the same averaging window $[5T_A, 20T_A]$, as proposed for the unpenalized case, is used.

Average streamwise velocity profiles are shown in figure 4.19. Only the uncontrolled case and the averages over $[5T_A, 20T_A]$ are shown for $\gamma = 1/2$ and $\gamma = 2/3$. Two logarithmic regions, above and below the turbines, are distinctly visible in the penalized cases also. It is observed that the wind at the turbine level decelerates a bit compared to the uncontrolled case, but this time, the outer layer slightly accelerates. This results from the fact that, overall, the driving power in these cases remains approximately constant (cf. figure 4.17); hence, with a constant driving force, the bulk velocity also remains constant. The velocity profile is higher for $\gamma = 2/3$ than for $\gamma = 1/2$, because the wind-farm power extraction and loss due to dissipation are lower in the former case.

Figure 4.20 shows the total, Reynolds and dispersive stresses. In contrast to the unpenalized case, the peaks of the total shear stresses in figure 4.20(a) (just above the wind farm) remain close to the uncontrolled case. For $\gamma = 1/2$, it is a little higher, and for $\gamma = 2/3$, it is a little lower than the uncontrolled case,

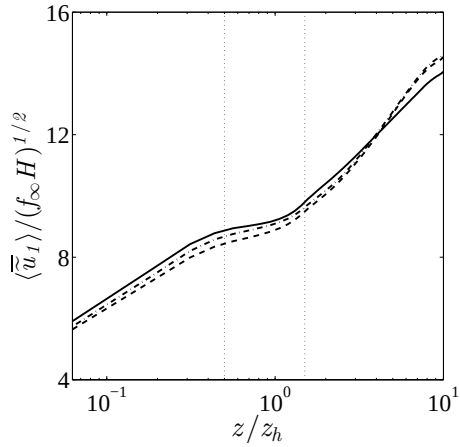

Figure 4.19: Streamwise mean velocities. (——, black): uncontrolled case; (- - -, dashed): $\gamma = 1/2$; (-·-·-, dot-dashed): $\gamma = 2/3$. The optimal control cases are averaged over the time window $[5T_A, 20T_A]$.

but this difference is statistically not significant in view of the limited temporal averaging time. As before, the dispersive stresses increase while the Reynolds stresses decrease. When looking at the normal stresses in figures 4.20(b)–(d) some further differences are observed compared to the optimal control case with $\gamma = 0$. First of all, as with $\gamma = 0$ (cf. figure 4.10), all dispersive stresses increase compared to the uncontrolled case (though not as much as with $\gamma = 0$). However, in contrast to $\gamma = 0$, the streamwise total stresses decrease compared to the uncontrolled case as a result of a significant decrease in the streamwise Reynolds stresses. Looking at the vertical transport in the penalized cases (figure 4.21), it is observed that the total transport remains largely unchanged, but is carried more by the dispersive stresses (i.e. by mean flow transport), and less by the turbulent stresses. For $\gamma = 2/3$, the flux decreases – as discussed above, the boundary layer accelerates slightly in this case.

As with the unpenalized case, the spatial distribution of the mean velocity profiles and Reynolds stresses are further analyzed by averaging these quantities in time and over the turbine subdomains. In figures 4.22(a) and 4.22(b), the mean streamwise velocity in a horizontal plane at the hub level is shown for $\gamma = 1/2$ and $\gamma = 2/3$ respectively. The wake velocity in both of the penalized cases is higher than in the unpenalized case (cf. figure 4.12(b)). When compared to the uncontrolled case (figure 4.12(a)), the case with $\gamma = 1/2$ has a lower wake velocity, while the wake of the case with $\gamma = 2/3$ is comparable to that of the uncontrolled case. In both of the penalized cases, the wake recovery is faster

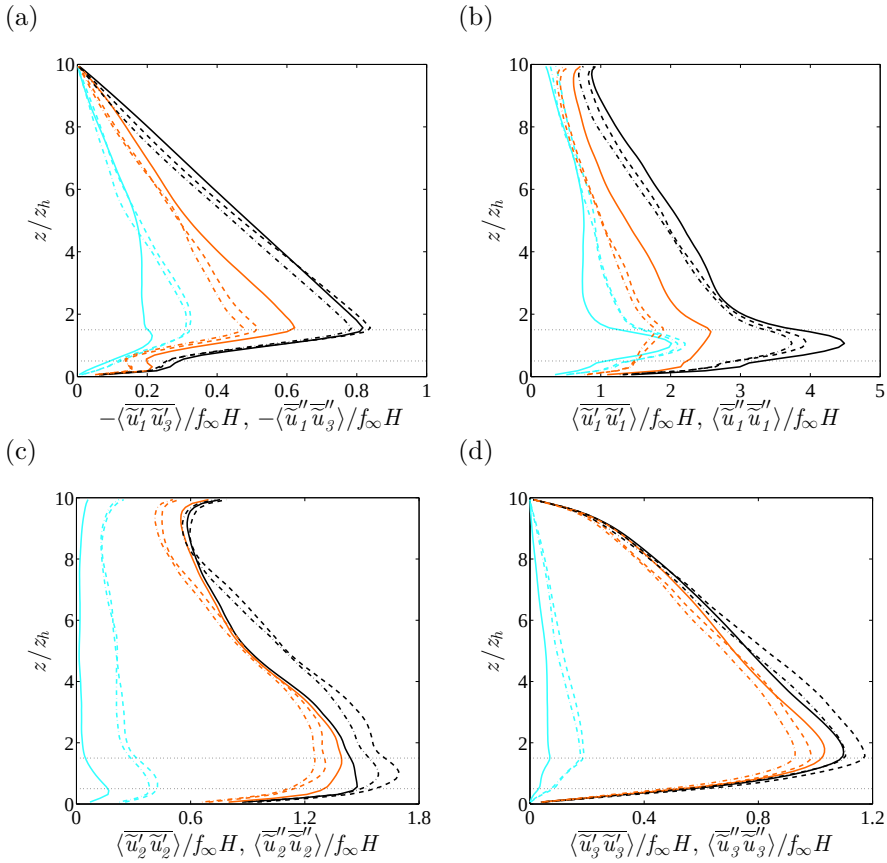

Figure 4.20: Vertical profiles of total, Reynolds, and dispersive stresses. (——, black; ——, orange; ——, cyan): respectively total stresses, Reynolds stresses and dispersive stresses for the uncontrolled case. (- - -, dashed; - - -, orange dashed; - - -, cyan dashed): respectively total stresses, Reynolds stresses, and dispersive stresses for the controlled case with $\gamma = 1/2$ averaged over $[5T_A, 20T_A]$. (-·-·-, dot-dashed; -·-·-, orange dot-dashed; -·-·-, cyan dot-dashed): same for case with $\gamma = 2/3$.

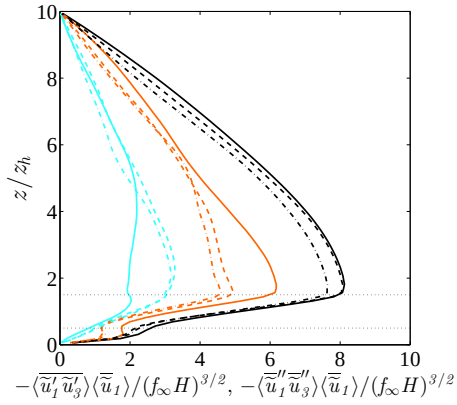

Figure 4.21: Vertical profiles of horizontally averaged mean-flow kinetic energy flux. (——, black; ——, orange; ——, cyan): respectively total kinetic energy flux, flux due to Reynolds stress, and flux due to dispersive stress for the uncontrolled case. (- - -, dashed; - - -, orange dashed; - - -, cyan dashed): same for the controlled case with $\gamma = 1/2$ averaged over $[5T_A, 20T_A]$. (- · - · -, dot-dashed; - · - · -, orange dot-dashed; - · - · -, cyan dot-dashed): same for case with $\gamma = 2/3$.

than in the uncontrolled case. A higher turbine inflow velocity in the penalized cases (compared to the uncontrolled case) is also obvious when figures 4.22(c,d) are compared with figure 4.12(c). In figures 4.22(e,f), the positive $-\widetilde{\overline{u}}_1''\widetilde{\overline{u}}_3''$ region around the rotor tip is similar to that in the uncontrolled case in figure 4.12(e) (slightly lower for $\gamma = 1/2$). However, for $\gamma = 2/3$, the strength of this positive $-\widetilde{\overline{u}}_1''\widetilde{\overline{u}}_3''$ is a bit higher in the wake region of the rotor.

Figures 4.23(a,b) show the Reynolds shear stresses in a horizontal plane through the rotor tip, and 4.23(c,d) show the same in a vertical plane through the rotor center. The Reynolds shear stress above the rotor is slightly higher for $\gamma = 1/2$ than in the uncontrolled case, and it is lower for $\gamma = 2/3$. In the region between the turbine rows, a significant decrease in the shear stress can be observed for both the cases. As a result, the horizontally averaged profiles in figure 4.20(a) are also lower for the penalized cases. As with $\gamma = 0$, Reynolds shear stress (figure 4.23(c, d)) does not increase in front of the turbine.

In figure 4.24, the normal Reynolds stresses are shown in a horizontal plane at the rotor tip (figures (a), (b)) and in the vertical plane through the rotor center (figures (c)–(h)). The streamwise component of the normal stress ($\overline{\widetilde{u}_1'\widetilde{u}_1'}$) is lower in the turbine wake region, as well as in the region between the turbine rows for both the cases. Similarly, $\overline{\widetilde{u}_2'\widetilde{u}_2'}$ is also lower for the penalized

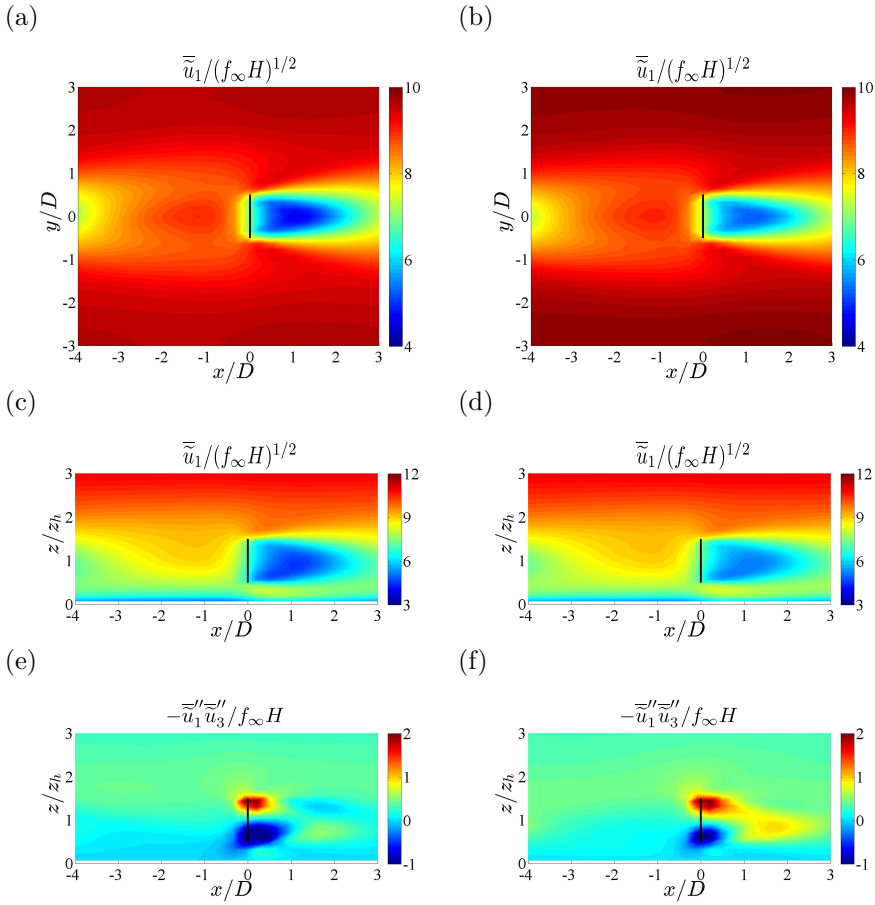

Figure 4.22: (a–d) Contours of mean streamwise velocity field averaged over control windows and turbine elements; (a,b) in a horizontal plane through the hub; (c,d) in a vertical plane through the turbine. (e,f): Contours of $\overline{\widetilde{u}}_1''\overline{\widetilde{u}}_3''$ in a vertical plane through the turbine. (left)(a,c,e): $\gamma = 1/2$ case; (right)(b,d,f): $\gamma = 2/3$ case. All averaged over time window $[5T_A, 20T_A]$.

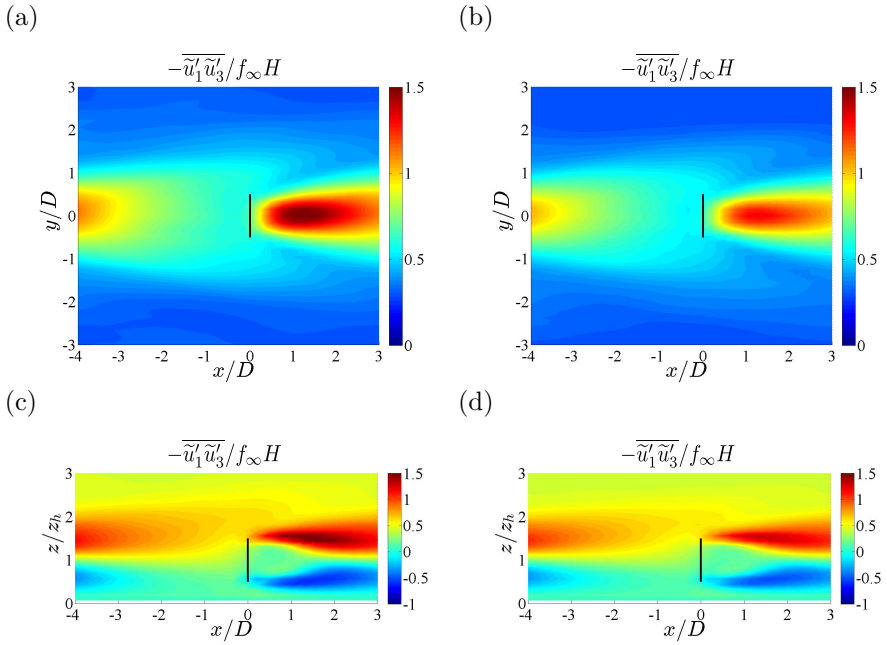

Figure 4.23: Contours of Reynolds shear stresses averaged over control windows and turbine elements. (a, c): $\gamma = 1/2$ case; (b, d): $\gamma = 2/3$ case. All averaged over time window $[5T_A, 20T_A]$. Figure (a) and (b) show a horizontal plane at the turbine-tip level; while (c) and (d) show xz–planes through the rotor center.

cases when compared to the uncontrolled case. However, contours of $\widetilde{\overline{u}}_3'\widetilde{\overline{u}}_3'$ in figures 4.24(g,h) are not much different from their counterpart in figure 4.12(g). Overall, the turbulent kinetic energy is lower for both the cases. When measured $1D$ upstream of the turbine and at the hub height level, $\widetilde{\overline{u}}_i'\widetilde{\overline{u}}_i'/2$ decreases by more than 18% and 23% for $\gamma = 1/2$ and $\gamma = 2/3$, respectively.

4.4 Summary

In the current chapter, the optimal control of an infinite farm with an aligned farm geometry was investigated. The receding-horizon approach and the non-linear conjugate-gradient method discussed in Chapter 3 were used for the optimization. The optimization was performed for 25 consecutive control windows with the number of conjugate-gradient iterations per control window

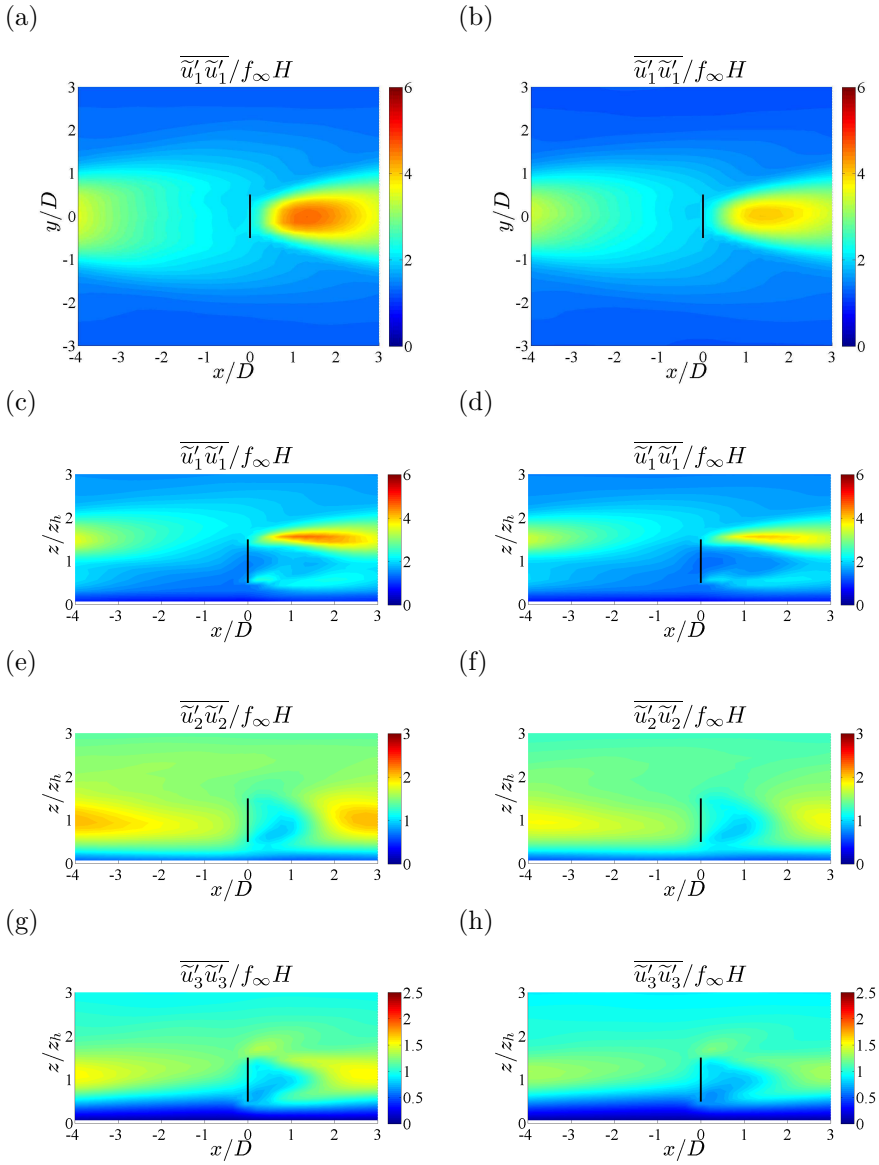

Figure 4.24: Contours of normal Reynolds stresses averaged over control windows and turbine elements. (a,c,e,g): $\gamma = 1/2$ case; (b,d,f,h):$\gamma = 2/3$ case. All are averaged over time window $[5T_A, 20T_A]$. Figures (a) and (b) show a horizontal plane at the turbine-tip level, while (c–h) show xz–planes through the rotor center.

limited to 5. In each control window, the turbine thrust coefficients were optimized over a time horizon of 280s, then used during the first half of that period before continuing with the next optimization window. This lead to one hour of accumulated wind-farm operation.

The first optimal control case of the infinite farm focused on direct maximization of the wind-farm energy extraction. It was found that the energy extraction increased up to 16% (for 1 hour), but overall, the boundary layer decelerated and dissipation levels increased. The increased energy extraction is directly related to an increase in vertical fluxes of kinetic energy. Analysis of dispersive and Reynolds stresses revealed that dispersive stresses (and fluxes) increase drastically, while Reynolds stresses decrease overall but increase locally in the wake region, inducing better wake recovery. Further analysis of the inner layer and turbine region of the boundary layer showed that boundary-layer deceleration was mainly occurring in the outer layer, while the inner layer remained more or less in equilibrium. For the current pressure-driven boundary layer, the driving power is not sufficient to keep the system in balance given the increase in power extraction.

Two more optimal control problems looked into maximizing the power extraction, but at the same time penalizing turbulent dissipation with the aim of triggering different overall energy balances with lower levels of vertical turbulent fluxes. It was found that, depending on the penalization level, total gains in energy extraction decreased and so did vertical fluxes of energy. For a pressure-driven boundary layer in equilibrium, estimated increases in energy extraction were in the order of 6%. This is related to a small shift in the ratio of wind-farm power extraction to total turbulent dissipation from 68% to 72%. Further analysis of the spatial distribution of mean velocity profiles and Reynolds stresses again revealed important differences between the controlled cases and the uncontrolled case. As with the unpenalized case, the turbine inflow improved with a slightly higher mean velocity and lower turbulence intensity. However, the wake deficit was much less pronounced as less energy was extracted.

Chapter 5

Optimal control of a finite farm

In the previous chapter, the optimal control of an infinite wind farm with periodic boundary conditions was investigated. The results showed promising gains in the energy extracted from a farm. Some important differences were also observed in the wind farm-BL interaction between the controlled and the uncontrolled cases. In reality however, turbines at the upstream edge of the farm experience undisturbed boundary layer inflow, even in a very large wind farm. Additionally, the presence of the farm is responsible for the development of an internal boundary layer over the farm. These effects cannot be simulated with periodic boundary conditions. Therefore, in the current chapter, the fringe region method is employed to include the non-periodicity in the streamwise direction, in order to investigate the application of the optimal coordinated control to a finite sized wind farm. In Section 5.1, the modified governing flow equations including the fringe forcing term are introduced. The adjoint for the fringe forcing term is also derived in this section. Section 5.2 provides the details about the case set-up. Characteristics of the controls and the optimized power output are discussed in Section 5.3, and time averaged flow profiles are presented in Section 5.4

5.1 Fringe region and extension of adjoints

The pseudospectral method used in the current dissertation imposes periodic boundary conditions in the horizontal directions. While the spectral method

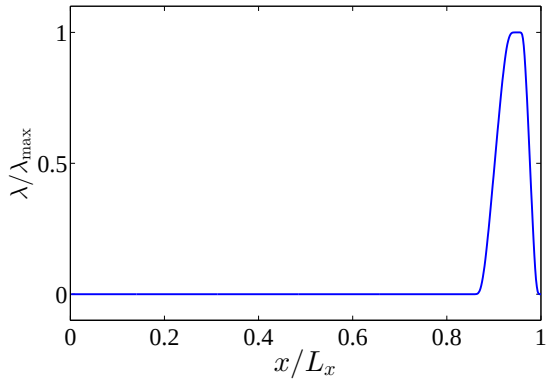

Figure 5.1: Illustration of the fringe function λ.

allows for more accurate calulation of the derivatives and also has a faster convergence, the developing boundary layer required for the finite-sized farm cannot be simulated in the periodic environment. Moreover, due to the streamwise periodicity, the wind-farm induced wakes leaving the domain will influence the flow upstream of the farm. Therefore, in order to damp the wind farm wake and impose a prescribed turbulent boundary layer profile upstream of the first turbine row, a fringe region is added to the domain. The governing flow equation 2.2 is modified to include the forcing term which is added to the momentum equation, i.e.

$$\frac{\partial \widetilde{\boldsymbol{u}}}{\partial t} + \widetilde{\boldsymbol{u}} \cdot \nabla \widetilde{\boldsymbol{u}} = -\frac{1}{\rho}\nabla \widetilde{p} + f_\infty \boldsymbol{e}_1 + \nabla \cdot \boldsymbol{\tau}_M + \boldsymbol{f} + \lambda(x)(\widetilde{\boldsymbol{u}}_{\text{pre}} - \widetilde{\boldsymbol{u}}) \tag{5.1}$$

where $\lambda(x)$ is a fringe function. As shown in figure 5.1, $\lambda(x)$ vanishes in most of the domain and has a non-zero value only in the fringe region. At the start of the fringe region, $\lambda(x)$ rises smoothly to the maximum value, and it decays smoothly to zero at the end of the region. Details about the definition of the fringe function and the associated parameters can be found in Canuto *et al.* [19]. $\widetilde{\boldsymbol{u}}_{\text{pre}}$ is the desired inflow velocity generated in a separate ABL simulation and is further discussed in Section 5.2 below.

The computational domain with the fringe region is schematically shown in figure 5.2. The boundary conditions, discretization scheme and other implementations remain the same as those discussed in §2.1. Therefore, they are not discussed again here.

The derivation of the adjoint for the fringe forcing term is presented next. Since the momentum equation – which is one of the state constraints in the current

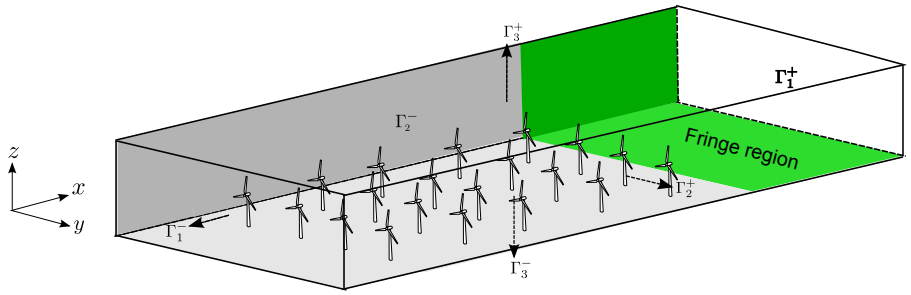

Figure 5.2: Computational domain with the fringe region.

optimization problem (cf. Eq. 3.5) – is modified, the Lagrangian (3.18) will change to

$$\begin{aligned}\mathscr{L}(\boldsymbol{\varphi},\boldsymbol{q},\boldsymbol{q}^*) &= \mathscr{J}(\boldsymbol{\varphi},\boldsymbol{q}) \\ &+ \int_0^T \int_\Omega \pi \nabla\cdot\widetilde{\boldsymbol{u}}\,\mathrm{d}\boldsymbol{x}\,\mathrm{d}t + \int_0^T \left[\tau\frac{\mathrm{d}\widehat{\boldsymbol{V}}}{\mathrm{d}t} - (\boldsymbol{V}-\widehat{\boldsymbol{V}})\right]\cdot\boldsymbol{\chi}\,\mathrm{d}t \\ &+ \int_0^T \int_\Omega \Big[\frac{\partial\widetilde{\boldsymbol{u}}}{\partial t} + \widetilde{\boldsymbol{u}}\cdot\nabla\widetilde{\boldsymbol{u}} + \frac{1}{\rho}\nabla\widetilde{p} - f_\infty\boldsymbol{e}_1 - \nabla\cdot\boldsymbol{\tau}_M \\ &\qquad - \boldsymbol{f} - \delta(\boldsymbol{x}-z_1\boldsymbol{e}_3)\boldsymbol{\tau}_{\boldsymbol{w}} - \boldsymbol{f}_{\mathrm{frin}}\Big]\cdot\boldsymbol{\xi}\,\mathrm{d}\boldsymbol{x}\,\mathrm{d}t, \end{aligned} \tag{5.2}$$

where $\boldsymbol{f}_{\mathrm{frin}} = \lambda(x)(\widetilde{\boldsymbol{u}}_{\mathrm{pre}} - \widetilde{\boldsymbol{u}})$. Following the derivations in §3.5, the adjoint for the fringe force, $\boldsymbol{f}^*_{\mathrm{frin}}$, can be identified as

$$\begin{aligned}(\boldsymbol{f}^*_{\mathrm{frin}}, \delta\widetilde{\boldsymbol{u}}) &= \int_0^T\int_\Omega [\lambda(x)(-\delta\widetilde{\boldsymbol{u}})]\cdot\boldsymbol{\xi}\,\mathrm{d}\boldsymbol{x}\,\mathrm{d}t \\ &= \int_0^T\int_\Omega -\lambda(x)\boldsymbol{\xi}\cdot\delta\widetilde{\boldsymbol{u}}\,\mathrm{d}\boldsymbol{x}\,\mathrm{d}t. \end{aligned} \tag{5.3}$$

Finally, adding this adjoint fringe force term to the adjoint momentum equation 3.41 yields

$$\begin{aligned}-\frac{\partial\boldsymbol{\xi}}{\partial t} - \widetilde{\boldsymbol{u}}\cdot\nabla\boldsymbol{\xi} - (\nabla\boldsymbol{\xi})^T\cdot\widetilde{\boldsymbol{u}} &= -\frac{1}{\rho}\nabla\pi + \nabla\cdot\boldsymbol{\tau}^*_M + \boldsymbol{f}^* \\ &\quad + \delta(\boldsymbol{x}-z_1\boldsymbol{e}_3)\boldsymbol{\tau}^*_{\boldsymbol{w}} - \lambda(x)\boldsymbol{\xi} \end{aligned} \tag{5.4}$$

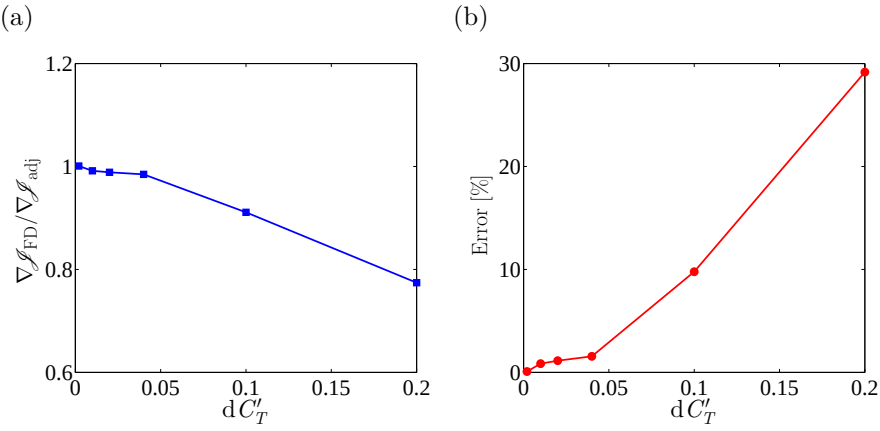

Figure 5.3: Comparison of the adjoint-based and finite-difference-based gradients. (a) Ratios of the finite-difference-based and adjoint-based gradients. (b) Errors in the adjoint-based gradient computation.

An interpretation of the fringe force in the adjoint equation can be made by comparing Eq.(5.4) to a system having non-periodicity with prescribed inflow as an inlet boundary condition. A simple derivation of the Lagrangian shows that for such a system, the inlet boundary condition for the adjoint equations becomes zero. The fringe forcing term, i.e. $-\lambda(x)\boldsymbol{\xi}$ would do the same by gradually damping the adjoint field $\boldsymbol{\xi}$ to zero within the fringe region. This can also be observed in the snapshots of the instantaneous adjoint fields shown in figure 5.5.

In figure 5.3, the adjoint-based gradient is compared with the gradients obtained from the finite difference method for $C_T' = 2.0$. As with §3.6, a case with a single turbine and a reduced domain size is considered for the purpose of verification. It can be appreciated from the figure that the adjoint-based gradient shows a good agreement with the finite-difference-based gradient for small perturbations ((i.e. $\mathrm{d}C_T' \leq 2\%$ of C_T')). As with the earlier verification, the error margin is well within 2% (cf. figure 5.3(b)), demonstrating that the adjoint for the fringe force is correctly implemented. It should be noted that for large $\mathrm{d}C_T'$, finite-difference approximation cannot accurately predict the gradient.

Table 5.1: Summary of the simulation set-up for the optimal control of a finite farm.

Domain size	$L_x \times L_y \times H = 10 \times 3.8 \times 1$ km^3
Fringe size	$L_{\text{frin}} \equiv 15\%$ of $L_x = 1.5$ km
Fringe region	Start: 8.5 km; End: 10 km
Driving pressure gradient	$f_\infty = 4 \times 10^{-4}$ m/s^2
Turbine dimensions	$D = 0.1H = 100$ m, $z_h = 0.1H = 100$ m
Turbine arrangement	10×5
Turbine spacing	$S_{\text{x}} = 7D$, and $S_{\text{y}} = 6D$
Surface roughness	$z_0 = 10^{-4}H = 0.1$m
Grid size	$N_x \times N_y \times N_z = 384 \times 256 \times 200$
Cell size	$\Delta_x \times \Delta_y \times \Delta_z = 26.0 \times 14.8 \times 5.0$ m^3
Time step	0.6 s

5.2 Case set up

The computational domain used in the earlier chapters is extended to accommodate the fringe region, while the turbine arrangement and spacings are kept the same. Details of the case set-up are summarized in Table 5.1. The domain size corresponds to $L_x \times L_y \times H = 10 \times 3.8 \times 1$ km^3. The fringe region accounts for 15 % of the streamwise length and is located at the downstream end of the domain, starting from $x = 8.5$ km. The distance between the last row of turbines and the start of the fringe region is set to 1.5 km (equivalent to $15D$). Although the periodic boundary condtion is used for the spanwise direction, the spacing between turbine columns at the two sides of the farm is increased to $14D$ (instead of the spanwise spacing $S_y = 6D$), so that the wake effect at the sides can be minimized and a more realistic wind farm can be mimicked. The computational grid corresponds to $N_x \times N_y \times N_z = 384 \times 256 \times 200$, and it is extended to $576 \times 384 \times 200$ for dealiasing.

The inflow velocity is generated in a seperate precursor simulation of the boundary layer, which has a domain size and grid resolution identical to those of the actual wind-farm simulation. It is driven by a constant pressure gradient and has periodic boundary conditions in the horizontal directions. As with the infinite farm simulations (cf . §2.3.1), a logarithmic velocity profile with

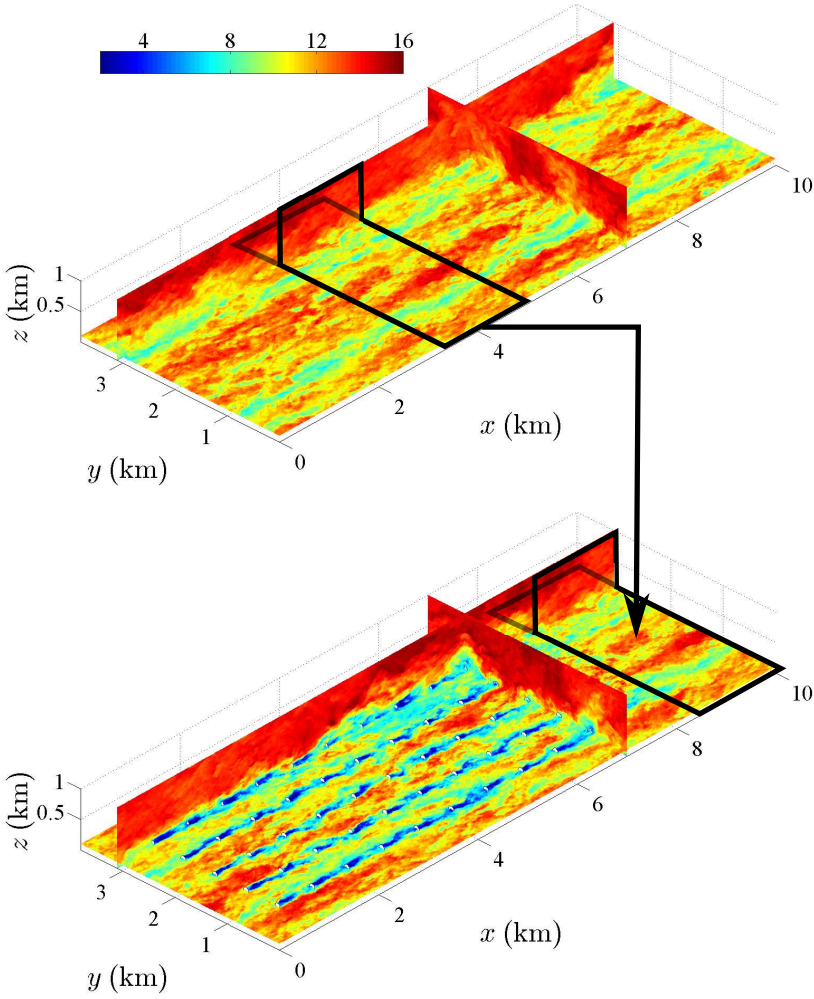

Figure 5.4: Snapshots representing instantaneous streamwise velocity fields from the precursor boundary layer simulation (top) and from the finite farm simulation (bottom). The horizontal planes in the figures are taken at the hub height.

superimposed random perturbations is used as an initial condition for the precursor simulation. After an initial statistical convergence during which the flow evolves into a fully developed turbulent boundary layer, the instantaneous velocity data in a region of a size equal to that of the fringe region, L_{frin}, is written to files in every time step. This precursor data is read from the database and fed into the fringe region during the forward simulations in the optimization. Note that the wind-farm simulation is initialized with the converged precursor field and uses a spin-up period of approximately two through-flow time periods. As an alternative to this approach, Stevens *et al.* [97] proposed a 'concurrent precursor method' in which the precursor BL simulation and the wind-farm simulation are performed simulataneously. The advantage of their method is that it avoids the requirement of a large disk space for storing inflow data. However, for the optimal control of a wind farm considered in the current dissertation, several forward function evaluations (LES simulations) are required for the line search and conjugate-gradient algorithm. If the concurrent approach is used, the same precursor simulation has to be performed multiple times for every optimization window, and hence, it may not be computationally efficient. Therefore, for this dissertation, the precursor field is generated before the optimization starts.

In figure 5.4, snapshots of the instantaneous velocity field for the precursor simulation (top) and the simulation with the wind farm (bottom) are shown. The precursor field is a fully developed turbulent boundary layer characterized by time-dependent turbulent structures. It is appreciated that the regions surrounded by lines in both snapshots show a strong resemblance to each other. In particular, the latter half of the fringe-region is so similar to its precursor counterpart that it is difficult to distinguish one from the other. This suggests that the fringe-region is able to damp the wind farm wake and correctly adjust the inflow to the undisturbed field obtained from the precursor simulation. Looking at the second snapshot, one can observe the typical meandering of turbine wakes in the horizontal plane, which was also the case with the infinite farm simulation(cf. figure 2.5).

The cost functional for the optimal control of the finite farm corresponds to the total energy extracted from the boundary layer over the optimization time horizon T, i.e. defined by Eq. (3.1). No penalization term is used in the cost functional, and thus it is similar to the first optimization case in the previous chapter (cf. §4.2). The optimization algorithm is started with $C'_{T,i} = 2.0$ (i.e. $\boldsymbol{\varphi}^{(0)} = 2.0$) for all the turbines in the farm. This value of $C'_T = 2.0$ corresponds to the optimal operating condition of a single turbine in an idealized condition and in the absence of any drag forces. The optimization is limited to four conjugate gradient iterations instead of the five iterations used in Chapter 4. This is necessary because the size of the grid for the finite farm is 3.5 times

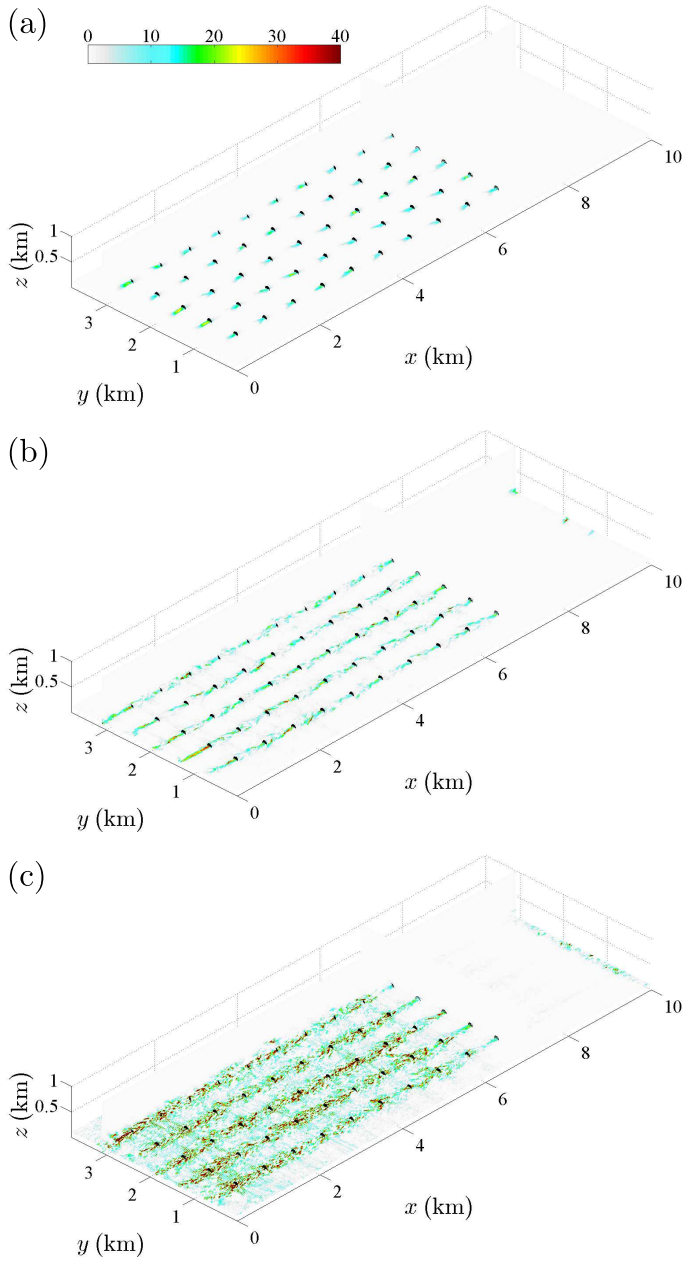

Figure 5.5: Contours of instantaneous streamwise adjoint field for the finite farm, obtained from the first gradient calculation in control window 1. Horizontal planes in the figures are taken at the hub height. (a) $T - t = 22$s, (b) $T - t = 70$s, (c) $T - t = 175$s

larger than that of the infinite farm case. Therefore, to limit the computational cost and also to slightly speed up the process, the optimization is stopped after just four CG iterations.

In figure 5.5, snapshots of instantaneous adjoint fields are shown for the finite farm. The fields belong to the first adjoint equations in the optimization sequence of the first optimal control time horizon (see figure 3.1): at this point, the equations are linearized around a flow state that is obtained for initially constant controls at all turbines with $C'_{T,i}(t) = 2.0$ $(i = 1 \cdots N_t)$. Since the initial condition for the adjoint equation corresponds to $\boldsymbol{\xi}(\boldsymbol{x}, T) = 0$, at $T - t = 22$ (figure 5.5(a)), the field is largely zero (see discussion in §4.2.1). As with the evolution of adjoints in the infinite farm cases, at $T - t = 22$s and $T - t = 70$s, it is observed that changes to the cost functional originate from tubes upstream of the rotors. However, in the snapshot at an earlier time $(T-t = 175$s) the tubes hit the upstream turbines and the adjoint field becomes fully turbulent inside the farm. This indicates that the power generation in a wind farm is influenced by the interactions between the turbines as well as by their interaction with the boundary layer. Finally, the role of the fringe region in the adjoint simulation is to suppress the upstream propagation of the field. This is clearly visible in figure 5.5(c). The adjoint field in the fringe region is almost zero, except for the very end of the domain where the fringe function $\lambda(x)$ is small. In this way, the interaction between the adjoint field developing upstream of the farm and the downstream turbines can be avoided, thereby imposing the non periodicity in the streamwise direction.

5.3 Controls and optimized power output

In figure 5.6, the time evolution of the optimal thrust coefficient for one of the turbines is shown. As with the unpenalized optimal control case of the infinite farm (cf. figure 4.3), the control changes strongly in response to the turbulent flow field. It can be seen that C'_T touches the lower and upper limits imposed by the box constraints, i.e. $0 \leq C'_{T,i}(t) \leq 4$, frequently. However, zooming in on C'_T reveals, as shown in the right figure, that the time scales with which the controls change is above 10 seconds.

Figure 5.7 shows the time series of the total wind-farm power extraction per unit farm area. It can be appreciated from the figure that the total farm power fluctuates significantly after the start of the optimal control. This was also observed in the optimization of the infinite farm. Compared to the uncontrolled case, a gain in energy extraction of 7.3% is achieved on average. The value is significantly lower in comparison to the gain of 16% in the case of

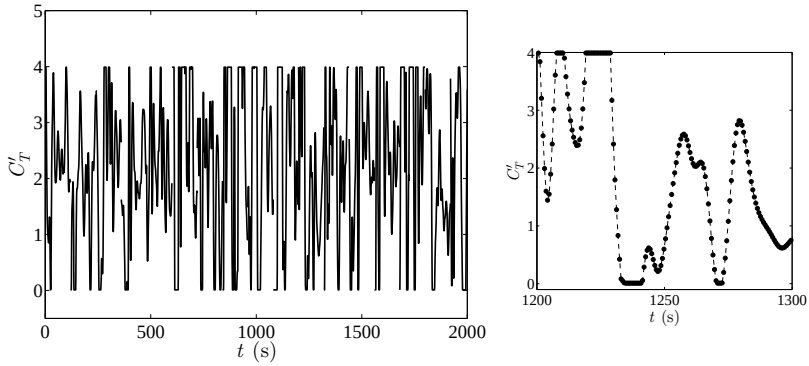

Figure 5.6: Time evolution of the thrust coefficient of one of the turbines in the farm.

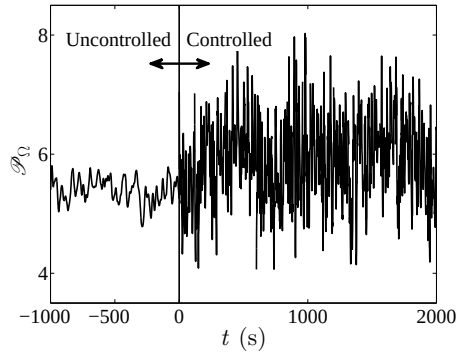

Figure 5.7: Time evolution of total farm power output.

the unpenalized infinite farm. One reason for this could be that a lesser number of conjugate gradient iterations is used for the finite farm case. Moreover, the turbines in the front row are already operating close to the optimal condition, and hence, optimal control cannot improve their performance too much. In the current case, the power extraction from the first row is about 16.5% of the total farm power. However, even the 7.3% increase in energy extraction achieved in the current dissertation can be quite beneficial, particularly for large wind farms with operational capacities ranging from a few hundred MW to a few GW. It should also be remarked that for some of the control windows, a power gain of 14% is achieved.

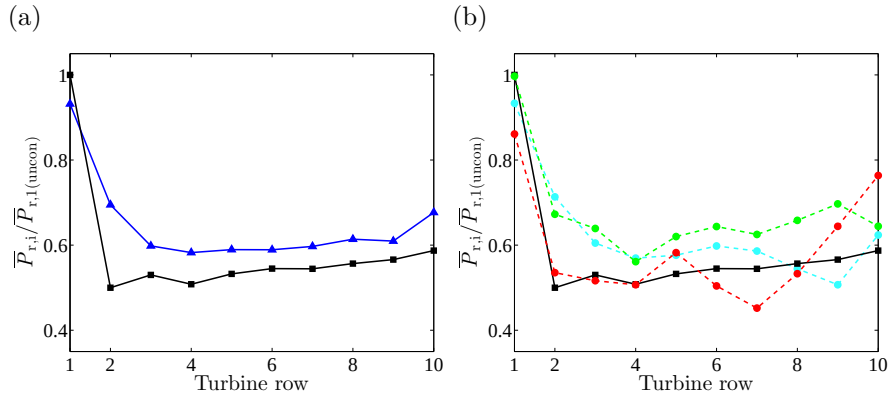

Figure 5.8: Comparison of the time averaged power output for the controlled and uncontrolled farm as a function of turbine row. In both figures, dark square(■) indicates the power output for the uncontrolled case. (a) Optimal control case averaged over the time interval $[0, 15T_A]$ (▲). (b) Power output for different control windows. Window 1 (●); Window 5 (●); Window 12 (●).

In figure 5.8, the time-averaged power output of different turbine rows are shown for both the optimal control and uncontrolled cases. The results presented in this figure are additionally averaged over all the turbines in each row and then normalized by the average power output of the first row obtained from the reference uncontrolled simulation. The time and row-averaged power is denoted by $\overline{P}_{\mathrm{r,i}}$, where the subscript 'r, i' stands for turbines in the i^{th} row. The uncontrolled power outputs show a very good agreement with field data [8, 7], as well as with other prior LES investigations [83, 97, 110] of wind farms with similar configurations and turbine spacings. A sharp drop in power production is observed between the first row and the second row, which is consistent with the results from the other studies. For the turbine rows further downstream, the power deficit remains more or less constant. However, as shown in figure 5.8(a), the optimal control case does not follow the same trend. First of all, the power output from the first row is lower compared to the uncontrolled case. Next, it is interesting to observe that, unlike in the uncontrolled case, the transition towards the constant power deficit in downstream rows is smooth. This is possibly due to the fact that the velocity deficit due to the first row is lower in the controlled case (since it extracts less energy from the flow), allowing for higher power production in the second row. It is also appreciated from the figure that the overall power production of the controlled farm is higher. Figure 5.8(b) presents the power output for several control windows. A strong variation in the extracted power can be observed from window to window. This is because the averaging time per

control window is very small (approximately 2 minutes); hence, fluctuations in the instantaneous power are not completely filtered out.

5.4 Averaged flow profiles

In order to further understand the relation between the flow field and the power production of the farm, the spatial distribution of the time-averaged mean velocity profiles and Reynolds stresses are analyzed in this section. The flow fields from the optimal control case are averaged over time window $[0, 15T_A]$, and the uncontrolled case is also averaged over the same time span. First of all, in figures 5.9(a,b), the mean streamwise velocity in a horizontal plane at the hub level is shown. The overall velocity distribution in the controlled and uncontrolled cases is more or less the same. However, a closer look into the results reveals that most of the turbines in the controlled case have shorter wakes than in the uncontrolled case. This clearly shows that the wake recovery is faster for the controlled case. Shorter wake length for the controlled case is also visible for several turbines in figures 5.9(c,d), where the streamwise velocity is shown in an xz–plane through one of the turbine columns. It can also be appreciated from figures (c,d) that both the uncontrolled and controlled cases are characterized by the internal boundary layer, developing from the first turbine row.

In figures 5.10(a,b), the streamwise components of the normal Reynolds stresses are shown in a horizontal plane at the turbine-tip level. The streamwise stress $\overline{\widetilde{u}_1'\widetilde{u}_1'}$ is lower for the controlled case in the turbine wake region as well as in the channels between the turbine columns. However, the vertical–streamwise plane through the turbine column shown in figures 5.10(c,d) presents a different picture. These two figures show that for most of the turbines, the normal stresses in the wake region are signifcantly higher for the controlled case. But when looking upstream of the turbines (about 1D upstream), it can be observed that $\overline{\widetilde{u}_1'\widetilde{u}_1'}$ decrease in the controlled case compared to the uncontrolled case. This was also observed in the optimal control of the infinite farm (cf. figure 4.14).

Figures 5.11(a,b) show the Reynolds shear stresses $(-\overline{\widetilde{u}_1'\widetilde{u}_3'})$ in a horizontal plane through the rotor-tip, and 5.11(c,d) show the same in a vertical plane through one of the turbine columns. The difference between the Reynolds shear stresses in the horizontal plane for the uncontrolled and controlled cases is not very significant. Although $-\overline{\widetilde{u}_1'\widetilde{u}_3'}$ is higher in the controlled case for the first turbine row (i.e. the upstream end of the farm) , the same is not true for the other turbines in the farm. For downstream turbines, the shear stresses for the

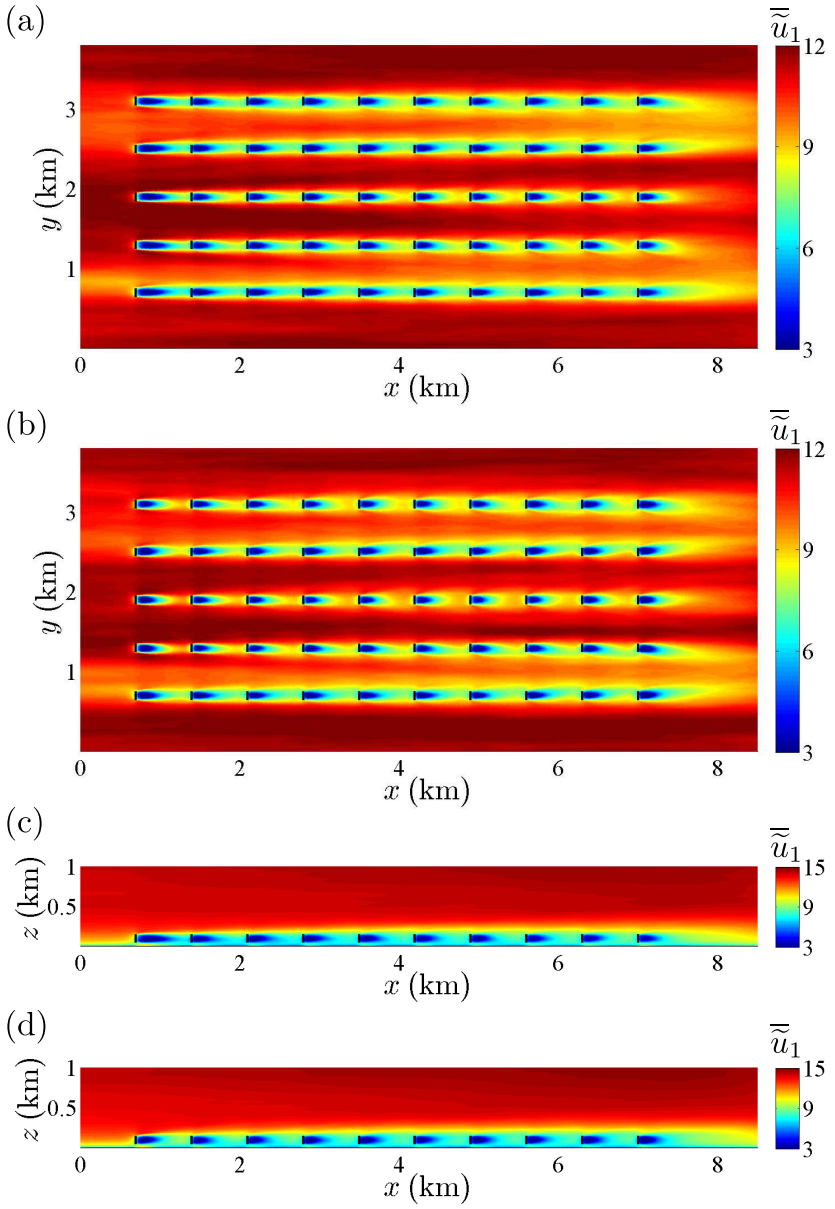

Figure 5.9: Contours of mean streamwise velocity field averaged over time window $[0, 15T_A]$. (a,b) in a horizontal plane at the hub level; (c,d) in a vertical plane through a turbine column. (a,c): uncontrolled case; (b,d): the optimal control case.

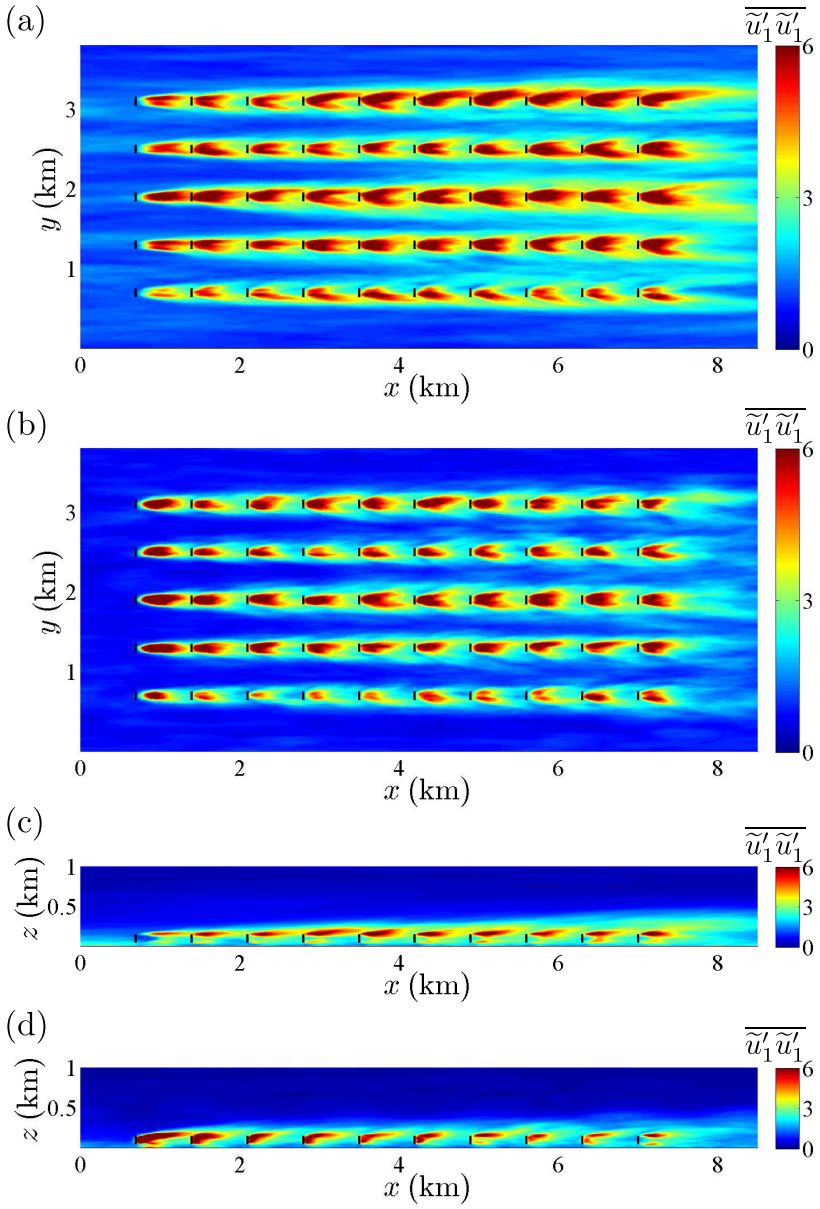

Figure 5.10: Contours of mean streamwise component of the normal Reynolds stresses averaged over time window $[0, 15T_A]$. (a,b) in a horizontal plane at the turbine-tip level; (c,d) in a vertical plane through a turbine column. (a,c): uncontrolled case; (b,d): the optimal control case.

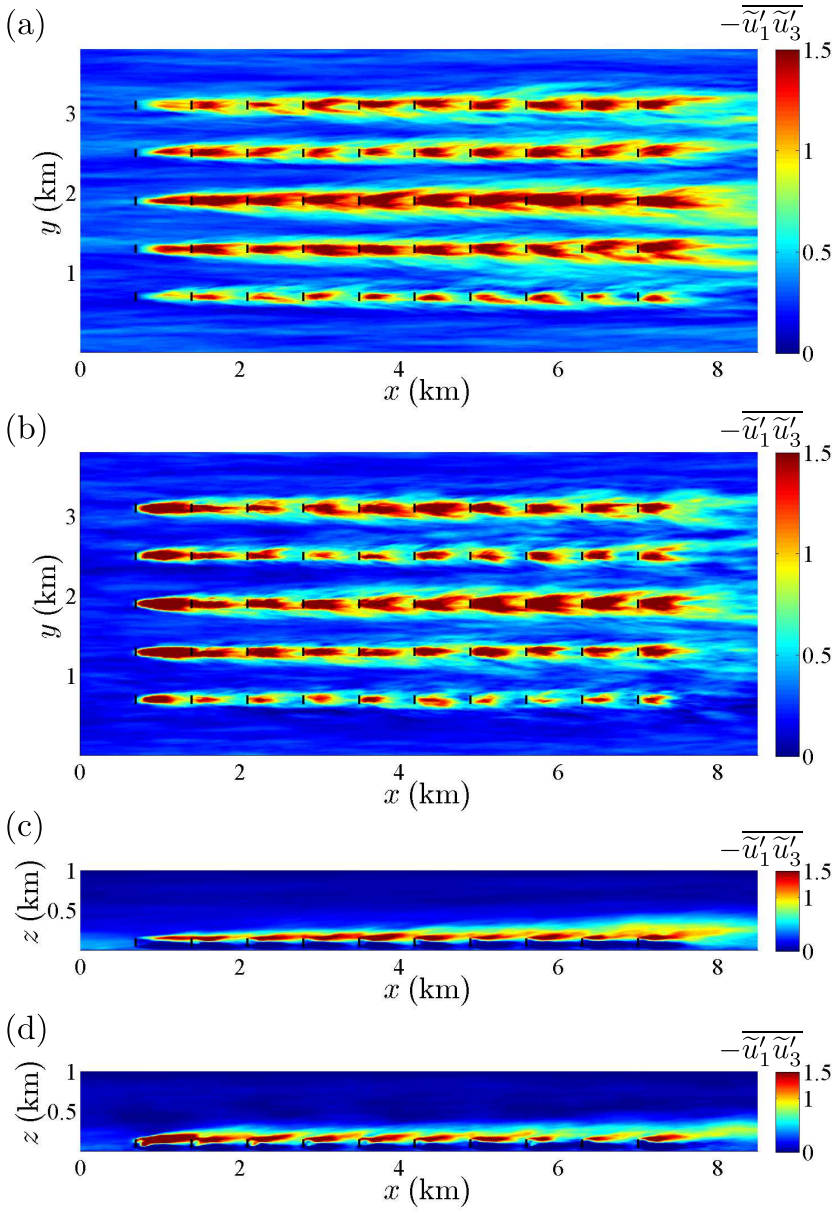

Figure 5.11: Contours of Reynolds shear stress averaged over time window $[0, 15T_A]$. (a,b) in a horizontal plane at the turbine-tip level; (c,d) in a vertical plane through a turbine column. (a,c): uncontrolled case; (b,d): the optimal control case.

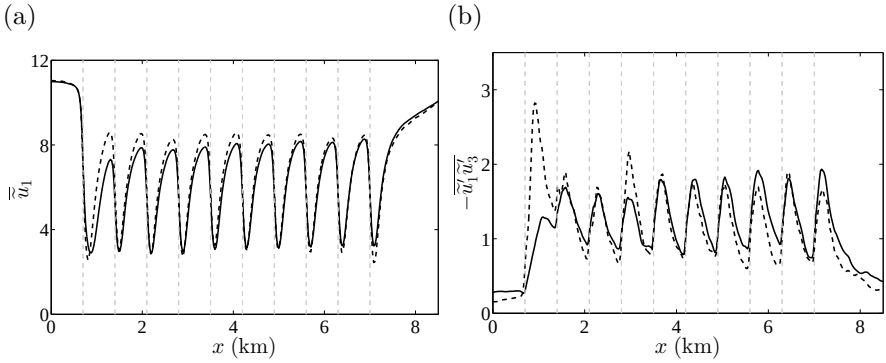

Figure 5.12: Time and row averaged profiles of (a) streamwise velocity through the rotor center and (b) Reynolds shear stress through the turbine tip. (——, black): uncontrolled case; (- - -, dashed): optimal control case averaged over the time interval $[0, 15T_A]$. Vertical dashed lines represent the streamwise location of the turbines.

uncontrolled and controlled cases are similar. This is further analyzed by taking time and row averages of the streamwise velocity and the Reynolds shear stress. Figure 5.12(a) shows the streamwise velocity in a streamwise line through the rotor center, and figure 5.12(b) shows the Reynolds shear stress in a streamwise line through the turbine-tip. As with the observation in figure 5.9, the inflow velocity of the turbines in the controlled case is slightly higher, whereas the wake velocity for the downstream turbines is more or less the same for both cases. In the controlled case, the Reynolds shear stress increases significantly above the turbine-wake region for the first row, and it is also higher for the fourth row. Additionally, the Reynolds shear stress is lower in front of most of the turbines in the controlled case. This may be the reason for the better wake recovery in the controlled case. However, this reasoning is very speculative, since the increase in the Reynolds shear stress in the first row (and the fourth row) may not be sufficient to influence the overall energy flux in the whole farm. Further analysis of the data will be necessary to understand the complete mechanism. The Reynolds shear stress is slightly lower for the controlled case in the channels between the turbine columns (cf. figure 5.11(a,b)).

5.5 Summary

In the current chapter, application of the optimal control to a finite-sized wind farm was explored. To this end, a fringe region was employed to impose non-

periodicity in the spectral code, and the adjoint for this fringe forcing term was derived and added to the original adjoint equations. The simulation domain was extended to $10 \times 3.8 \times 1$ km^3 to accommodate the fringe region which accounted for 15% of the streamwise length, while the wind-farm geometry and the number of turbines were kept the same as those of the earlier chapters. The energy extraction increased by 7.3% as a result of optimization. Although the value was significantly lower in comparison to the gain in the optimal control of the infinite farm, even the gain of 7.3% is promising and can be beneficial, especially for large wind farms. One possible reason for this lower gain could be the lesser number of conjugate gradient iterations per optimization window used in the finite-farm case. Another reason could be that the turbines in the front row – which contribute 16.5% of the whole farm power in the current case – are already operating close to the optimal condition, and hence, their performance cannot be improved much further by coordinated control.

Chapter 6

Conclusions and sugestions for future research

6.1 Conclusions

In the current dissertation, optimal control of wind-farm boundary layers in large-eddy simulations was investigated with the aim of increasing wind-farm energy extraction. Large-eddy simulations were performed in an in-house SP-Wind code which uses pseudospectral discretization in the horizontal directions and energy-conservative finite-difference discretization in the vertical directions. The first optimization studies were performed for an infinite wind farm with periodic boundary conditions in a pressure-driven boundary layer. Subsequently, the application of optimal coordinated control was investigated for a finite-sized wind farm with non-periodicity in the streamwise direction. Wind turbines were modeled using an actuator disk model (ADM). For the optimal control, individual turbines were considered to be flow actuators, whose energy extraction can be dynamically regulated in time so as to optimally influence the flow field in the boundary layer. Using the ADM made this consistent with dynamically controlling the turbine thrust coefficients in time and per wind turbine.

In order to define a reference case as well as a starting point for the dynamic optimal control, the first phase of this dissertation investigated the response of a wind-farm boundary layer to static changes in C_T'. To this end, thirteen different cases with $0.02 \leq C_T' \leq 3.5$ were considered, where the C_T' values were kept constant in time and the same for all turbines in a simulation. For

the purpose of comparison, the total power extraction of the farm in these simulations was normalized by three different references, based on the friction velocity $u_{\tau h}$, geostrophic wind G and the driving power of the PBL $f_\infty U_b H$. The optimal C'_T value for the geostrophic wind-based and driving power-based normalizations was approximately 1.33. This value is different from the C'_T value for the optimal operating condition of a lone-standing turbine, i.e. $C'_T = 2$. Further analysis of the energy balance demonstrated that even at the optimal point $C'_T = 1.33$, only 40% of the total power input was actually harvested by the wind farm, while 60% was dissipated by turbulence.

For the optimal control of wind-farm-boundary layer interaction, a receding-horizon approach was employed. In this approach, the optimization problem was divided into a number of control windows, also called time horizons, and the turbine thrust coefficients were optimized over each time horizon. The optimization problems were solved using a combination of the non-linear Polak-Ribière conjugate-gradient method [10] and the Brent line search algorithm [84, 65, 79]. A continuous adjoint-based approach was followed for the determination of the gradient of the cost functional required by the conjugate-gradient method. To this end, the adjoint equations for the standard Navier-Stokes equations were extended to include the adjoints for the Smagorinsky model and wall-stress model, and the adjoint of the actuator disk model. The implementation of the adjoint equations was first verified by comparing the adjoint-based gradients with those obtained from a finite difference method. It was found that both the gradients agreed very well, and the error margin for the adjoint-based gradient was well within 2%.

The wind-farm boundary layer considered for the optimal control of an infinite farm consisted of an aligned farm, with 10×5 turbines in a $7 \times 3 \times 1$ km^3 simulation domain and turbine spacings of $S_\mathrm{x} = 7D$ and $S_\mathrm{y} = 6D$, respectively in the streamwise and spanwise directions. In each control window, the turbine thrust coefficients were optimized over a time horizon of 280s, then used during the first half of that period, before continuing with the next optimization window. This led to a series of PDE-constrained optimization problems (one per control window) with approximately 20,000 degrees of freedom in the control space, and 1 billion in the space-time LES solution space. In order to limit computational costs, the number of conjugate-gradient iterations were limited to 5 per control window, and the optimization was performed for 25 consecutive optimal control problems, leading to 1 hour of accumulated wind-farm operation.

The first optimal control case of the infinite farm focused on direct maximization of wind-farm energy extraction. It was found that the energy extraction increased up to 16% (for 1 hour) or even 19% (for 12 minutes), but overall, the boundary-layer decelerated and dissipation levels increased. The increased

energy extraction is directly related to an increase in vertical fluxes of kinetic energy. A detailed decomposition of stresses into dispersive and Reynolds stresses revealed that dispersive stresses (and fluxes) increase drastically, while Reynolds stresses decrease overall but increase locally in the wake region, inducing better wake recovery. A further analysis of the inner layer and turbine region of the boundary layer showed that boundary-layer deceleration was mainly occurring in the outer layer, while the inner layer remained more or less in equilibrium. For the current pressure-driven boundary layer, the driving power is not sufficient to keep the system in balance given the increase in power extraction.

Two more optimal control problems looked into maximizing power extraction, but at the same time penalizing turbulent dissipation with the aim of triggering different overall energy balances with lower levels of vertical turbulent fluxes. It was found that, depending on the penalization level, total gains in energy extraction decrease and so do vertical fluxes of energy. For a pressure-driven boundary layer in equilibrium, estimated increases in energy extraction are in the order of 6%. This is related to a small shift in the ratio of wind-farm power extraction to total turbulent dissipation from 68% to 72%. Currently, these are estimates based on accumulated operation of 1 hour. Further research is warranted with longer averaging and with different types of penalization. For instance, boundary-layer deceleration may be directly penalized, and adaptive penalization may be considered to keep acceleration or deceleration within acceptable bands, etc.

In order to investigate the optimal control of a finite-sized wind farm, a fringe region was employed to impose non-periodicity to the domain. Furthermore, the adjoint for the fringe forcing term was derived and added to the original adjoint LES equations. The simulation domain was extended to $10\times3.8\times1$ km^3 to accommodate the fringe region which accounted for 15% of the streamwise length, while the wind-farm geometry and the number of turbines were kept the same as those of the infinite farm. It was found that energy extraction increases by 7.3% for the finite farm case. The value was significantly lower in comparison to the gain in the optimal control of the infinite farm. One possible reason for this could be the lesser number of conjugate gradient iterations per optimization window used in the finite-farm case. Another logical reason could be that the turbines in the front row are already operating close to the optimal condition, and hence, their performance cannot be improved much further by coordinated control. The contribution from the front row accounts for the 16.5% of the total farm power in the current case. Nevertheless, even the 7.3% gain achieved in this disseration is promising and can be beneficial, especially for large wind farms.

In summary, the current dissertation demonstrates the viability of the gradient-

and adjoint-based approach for the optimal control of wind farm energy extraction. The optimized power output shows the potential of what can be achieved from a wind farm when turbines are dynamically regulated in time. The results also yield some new insights into the mechanism responsible for the increased power output. One major effect of the optimization was that it was responsible for an increase in the kinetic energy flux towards the turbine region, which then translated into an increase in the power output. As stated earlier, due to the large computational resources demanded by such an optimal control framework, it is not suited for direct application in a real wind farm. However, the insight and understanding gained from this dissertation can be used for the development or modification of real-time controllers. Finally, techniques and algorithms developed in this dissertation provide important guidance for future optimization studies of wind farms with different objectives.

6.2 Suggestions for future research

The current dissertation presented optimal wind-farm boundary layer control, demonstrating considerable gains in energy extraction. Nevertheless, many challenges remain before this can be translated into real wind-farm applications. First of all, it will be interesting to investigate optimal control of wind farms in real atmospheric boundary layers, which include Coriolis forces, thermal stratification and capping inversion. Since the turbulence characteristics and the height of the boundary layers are different for convective, stable and neutral boundary layers (cf. discussion in §1.1), it is expected that the response of the optimal control for these three types of stratification will also be significantly different. Additionally, in a similar way to the observations in the uncontrolled simulations (see e.g. Ref. [1, 3]), energy entrainment from the flow above the boundary layer will play an equally important role in the optimal energy extraction. Furthermore, different wind-farm topologies are of interest, including possible terrain effect or effects of propagating waves in offshore farms (see e.g. Ref. [111, 112]). All such investigations will require extension of the adjoint equations employed in the current dissertation. For example, adjoints for the Coriolis forces and the transport equation for potential temperature as well as associated boundary conditions have to be derived and integrated to the current implementation to study wind farm optimization in the real ABL.

The turbine representation in the large-eddy simulation can also be refined, e.g. using an actuator line model with finer simulation resolutions instead of the actuator disk model used in the current dissertation. This allows for a better representation of turbulence effects on blade performance, and may further include dynamic stall models (see e.g. Ref. [61]) to describe blade

lift and drag coefficients as a function of time-varying local flow conditions. Next, details of the control description should be refined, using a formulation in terms of generator torque and blade pitch control that takes into account rotor and blade pitch inertia. The inclusion of turbine yaw settings, which can be used to change the direction of wakes [92], may also be relevant. Detailed representation of the wind turbines and control parameters will be important when considering the application of the optimal control to the reduction of loads experienced by turbines in a farm, or for simultaneous optimization of the farm power and loads in multi-objective optimization settings.

An extremely interesting research area could be the validation of the performance of the current optimization method in a wind-tunnel experiment. This will require a precise simulation of the wind tunnel environment and a very good representation of the turbines used in the experiment. On the experimental side, the biggest challenge will be designing a specialized controller which correctly mimics the control output from the optimal control simulation. To alleviate some of the complexities regarding the controller design, such a study should consider a farm with fewer turbines instead of the 50 turbines used in the current dissertation. An additional issue will be the difference in the evolution of the flow field in the experiment and the simulation. Regarding the implementation, the control data from the optimization can be used as an input in an open-loop actuation mechanism in the experiment. Obviously, such an investigation will pose various challenges on both the experimental and numerical sides. However, if successful, it will be an important accomplishment for the wind energy community.

The optimal control methodology can also be further developed, e.g. by using more efficient gradient-based approaches (see e.g. Badreddine *et al.* [5]), investing more computational resources in converging the optimums, and by including multiple starting points in the optimization algorithms to explore possible multiple local optimums. For the finite farm case, larger domain size can be considered and the optimization window can be extended to a longer time horizon; for example, several through-flow times. This may be important in capturing the effect of the dominant turbulent structures with longer length and time scales on the optimal solution. However, such a large scale optimization can be very demanding, both with respect to the computational cost and the disk storage requirement. An additional issue with the adjoint-simulation in the turbulent flow is that it becomes highly unstable for longer time horizons; this is a subject for further research [11].

The cost functionals considered in the current dissertation were simply the total energy extraction from the farm or with an additional penalization term based on the total dissipation. Although this is a logical choice, since the objective was to maximize the farm power output, it will be important to explore other

formulations, which may lead to a better optimal solution. For example, in this dissertation, it was found that the increased energy extraction in the optimal control case was directly related to an increase in vertical fluxes of kinetic energy. Therefore, the cost functional can be defined based on the kinetic energy flux so that the optimization will modify the controller to improve the entrainment towards the farm region. It will be interesting to compare optimization results for different objective functions. Additional modifications can be made with respect to the constraints on the controls. Instead of imposing box constraints as done in the current dissertation, they can be added as a penalty term in the cost functionals.

Finally, the current optimal control approach allows one to evaluate the potential of the dynamically regulated wind farm, but it is not practicable for use as a real-time controller. Development of real-time controllers that approximate the performance of the idealized optimal control is an interesting future challenge.

Appendix A

Blade element analysis of turbine-disk thrust coefficient

In the current appendix, the relation between the disk-based thrust coefficient C'_T and the turbine-blade characteristics are presented using blade element analysis (§A.1). In addition, this relationship is further used to estimate a reasonable order of magnitude for the upper bound on C'_T used in the optimal control (§A.2)

A.1 Blade element analysis

Given the disk-based velocity V_d, and the turbine rotation speed ω, the local velocity triangles around the turbine blades can be constructed – see figure A.1. This corresponds to the conventional velocity triangles in blade element-momentum theory (see e.g. Ref. [14]), but based here on disk velocity. Thus

$$\sin\phi = \frac{V_d}{W} \quad \text{and} \quad \cos\phi = \frac{\omega r(1+a_t)}{W}, \tag{A.1}$$

with W the relative velocity to the blade, and with a_t the tangential induction factor (further details follow). Moreover,

$$W = \left\{V_d^2 + [\omega r(1+a_t)]^2\right\}^{1/2} = V_d\left\{1 + [\lambda'\mu(1+a_t)]^2\right\}^{1/2}, \tag{A.2}$$

where $\lambda' = \omega R/V_d$ (the tip-speed ratio based on disk velocity), and $\mu = r/R$ (with R the turbine radius).

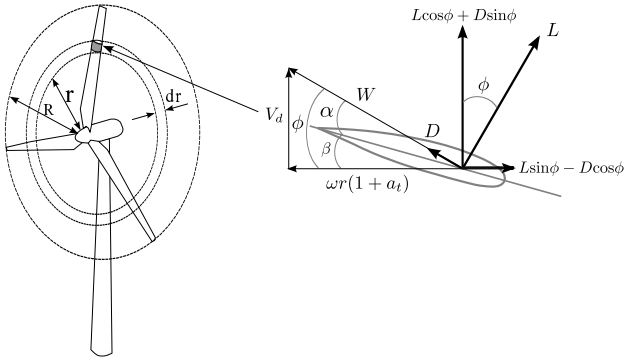

Figure A.1: Velocity and force components at a cross section of a blade element.

Given an annular ring with thickness dr (cf. figure A.1) the force exerted on the flow in this ring by N blades with chord c, corresponds to

$$\delta F = \frac{1}{2}\rho W^2 N c(c_L \cos\phi + c_D \sin\phi)\mathrm{d}r, \tag{A.3}$$

$$= \frac{1}{2}\rho V_d^2 N c(1 + [\lambda'\mu(1 + a_t)]^2)^{1/2}\,(c_L\lambda'\mu(1 + a_t) + c_D)R\delta\mu \tag{A.4}$$

where $c_L(r)$ and $c_D(r)$ are the lift and drag coefficients of the blade profiles.

By definition $C'_T \equiv 2F/(\rho V_d^2 A)$. Thus, δF can be integrated along the radius to obtain

$$C'_T = \int_0^1 \frac{Nc}{\pi R}(1 + [\lambda'\mu(1 + a_t)]^2)^{1/2}\,(c_L\lambda'\mu(1 + a_t) + c_D)\,\mathrm{d}\mu. \tag{A.5}$$

This expression only depends on the turbine blade geometry, the blade lift and drag coefficients, and the selected tip-speed ratio λ' at which the turbine is operated. A further unknown is the tangential induction factor a_t, but this is straightforward to express in terms of the same parameters, as shown next.

The torque exerted by the turbine on the flow in the same annular ring with thickness dr (cf. figure A.1) can be similarly expressed as

$$\delta T = \frac{1}{2}\rho V_d^2 N c(1 + [\lambda'\mu(1 + a_t)]^2)^{1/2}\,(c_L - c_D\lambda'\mu(1 + a_t))R^2\mu\mathrm{d}\mu. \tag{A.6}$$

This torque induces a change of angular momentum of the flow passing through the annular ring, leading to a difference in tangential velocity ΔV_θ before and after the turbine. Thus the change in angular momentum corresponds to $\delta M =$

Table A.1: Blade element evaluation of C'_T for a range of λ' and c values, using the NREL 5 MW turbine [56] as a baseline.

λ'	chord (c)	C'_T
10.5	original	1.6
12.15	original	1.8
12.15	+30%	2.5
12.15	+50%	2.8
13.9	+50%	3.2
13.9	+80%	3.75
13.9	+100%	4.2

$2\pi r \mathrm{d}r \rho V_d \Delta V_\theta r = 4\pi\rho V_d \omega a_t r^3 \mathrm{d}r$, where by convention $a_t \equiv \Delta V_\theta/(2\omega r)$. Since $\delta M = \delta T$, an implicit expression for $a_t(\mu)$ is given by

$$8\lambda'\mu^2 a_t = \frac{Nc}{\pi R}(1 + [\lambda'\mu(1+a_t)]^2)^{1/2}\,(c_L - c_D\lambda'\mu(1+a_t)). \tag{A.7}$$

This also depends only on blade geometry, aerodynamic coefficients, and tip-speed ratio.

Finally, since $C'_P \equiv 2T\omega/(\rho V_d^3 A)$, and integrating (A.6) over the radius,

$$C'_P = \int_0^1 \frac{Nc}{\pi R}(1 + [\lambda'\mu(1+a_t)]^2)^{1/2}\,(c_L - c_D\lambda'\mu(1+a_t))\lambda'\mu \mathrm{d}\mu. \tag{A.8}$$

The ratio $C'_P/C'_T < 1$. For the ideal case that $c_D = 0$, and that no swirl is added to the wake ($a_t = 0$), it is readily seen that $C'_T = C'_P$. For the idealized case of the Betz limit, $V_d = 2V_\infty/3$ [14], so that further $C'_T = C'_P = 2$.

A.2 Estimate of an upper value for C'_T

In the current section a reasonable upper value for C'_T that can be used as constraint in the optimal control algorithm is estimated. Given a turbine design, it is straightforward to decrease C'_T by pitching the blades. However, increasing C'_T beyond its original design value is not simply possible without losing a lot of efficiency (e.g. by stall). Nowadays, turbines are designed to have C'_T values

that are maximum around 2. Higher values do not make sense, as these are above the optimal Betz value. However, for the optimal control in the current work, we do not want to restrict C'_T *a priori* to a maximum of two. Here, the relation between C'_T and design choices such as the turbine blade chord, and the operational tip-speed ratio for a real turbineis is briefly investigated.

As a reference, the specifications (geometry, tabulated lift and drag coefficients, etc.) of the "NREL offshore 5 MW baseline wind turbine" [56] are considered. Using (A.5) and (A.7), C'_T is calculated for a range of tip-speed ratios λ', and chord lengths c, keeping all other parameters unchanged. Results are shown in Table A.1. Given those results, a maximum value for C'_T of 4 is chosen in the optimal control. This value is arbitrary, but is merely intended to give an order of magnitude of what could be technically feasible.

Appendix B

Geostrophic Wind

In the current appendix, a relation between $u_{\tau h}$ and the geostrophic wind speed G is derived for 'infinite' wind-farm ABLs, partly inspired by the work of Zilitinkevich [115]. The atmospheric boundary layer is driven by the geostrophic balance above the boundary layer, where, in the absence of any friction terms, the pressure gradient is balanced by Coriolis forces, i.e. [101, 99]

$$\frac{1}{\rho}\frac{\partial p_\infty}{\partial x_1} = f_c G \sin\alpha, \qquad \text{and} \quad \frac{1}{\rho}\frac{\partial p_\infty}{\partial x_2} = -f_c G \cos\alpha, \tag{B.1}$$

with f_c the Coriolis parameter, G the magnitude of the geostrophic wind and α the angle between the geostrophic wind and the wind in the surface layer (which is in the x_1 direction).

The Navier–Stokes momentum equations with Coriolis forces now correspond to

$$\frac{\partial \boldsymbol{u}}{\partial t} + \boldsymbol{u}\cdot\nabla\boldsymbol{u} = -\frac{1}{\rho}\nabla(p+p_\infty) + f_c\boldsymbol{u}\times\boldsymbol{e}_3 + \nu\nabla^2\boldsymbol{u} + \boldsymbol{f}, \tag{B.2}$$

where p represents the remaining part of the pressure (after removing p_∞), ν is the kinematic viscosity and f_c is the Coriolis parameter.

Multiplying (B.2) with $\boldsymbol{u}$, averaging over horizontal planes and integrating over the height of the ABL yields the total energy balance. For statistically stationary boundary layers, and using (B.1) and continuity, this leads to

$$\int_0^H f_c(-G\sin\alpha\,\langle u_1\rangle + G\cos\alpha\,\langle u_2\rangle)\,\mathrm{d}x_3$$

$$= \underbrace{\int_0^H \nu\langle\nabla\boldsymbol{u} : \nabla\boldsymbol{u}\rangle\,\mathrm{d}x_3}_{\mathscr{D}} - \underbrace{\int_0^H \langle\boldsymbol{f}\cdot\boldsymbol{u}\rangle\,\mathrm{d}x_3}_{-\mathscr{P}} \tag{B.3}$$

where $\langle\cdots\rangle$ is used to denote horizontal averages (statistically converged over 'infinite' horizontal planes). Furthermore, $\mathscr{D}$ is the total dissipation by turbulence per unit wind-farm area, and $\mathscr{P}$ is the average turbine power extraction per unit farm area.

The left-hand side of (B.3) can be further elaborated by horizontal averaging and integrating of the u_1 and u_2 momentum equations (B.2). For u_1, this leads to

$$-f_c G\sin\alpha\,H + \int_0^H f_c\langle u_2\rangle\,\mathrm{d}x_3 = \tau_w - \int_0^H \langle\boldsymbol{f}\cdot\boldsymbol{e}_1\rangle\,\mathrm{d}x_3, \tag{B.4}$$

$$= u_{\tau h}^2 \qquad \text{(using 2.17)} \tag{B.5}$$

For u_2

$$f_c G\cos\alpha\,H - \int_0^H f_c\langle u_1\rangle\,\mathrm{d}x_3 = 0. \tag{B.6}$$

(recall that x is aligned with the flow direction in the surface layer, so that the wall stress has no average component in the integrated y-momentum equation.)

Equation (B.5) and (B.6) are now used in (B.3) to eliminate $\langle u_1\rangle$ and $\langle u_2\rangle$, leading to

$$G\,\cos\alpha\,u_{\tau h}^2 = \mathscr{D} + \mathscr{P}. \tag{B.7}$$

Finally, the angle α can be further eliminated by using a similarity relation for the wind profile, i.e. following [101]

$$\frac{G\,\sin\alpha}{u_{\tau h}} = -A \tag{B.8}$$

where $A \approx 12$ is an empirical constant [32, 101]. Combining this with (B.7) yields

$$G = u_{\tau h}\sqrt{A^2 + \left(\frac{\mathscr{D}+\mathscr{P}}{u_{\tau h}^3}\right)^2} \tag{B.9}$$

Bibliography

[1] Abkar, M., and Porté-Agel, F. The effect of free-atmosphere stratification on boundary-layer flow and power output from very large wind farms. *Energies 6* (2013), 2338–2361.

[2] Ahmad, M. A., Azuma, S., and Sugie, T. A model-free approach for maximizing power production of wind farm using multi-resolution simultaneous perturbation stochastic approximation. *Energies 7* (2014), 5624–5646.

[3] Allaerts, D., and Meyers, J. Wind farm performance in conventionally neutral atmospheric boundary layers with varying inversion strengths. *J. Physics: Conference Series 524* (2014), 012114.

[4] Andersen, S. J., Sørensen, J. N., and Mikkelsen, R. Simulation of the inherent turbulence and wake interaction inside an infinitely long row of wind turbines. *Journal of Turbulence 14*, 4 (2013), 1–24.

[5] Badreddine, H., Vandewalle, S., and Meyers, J. Sequential quadratic programming (SQP) for optimal control in direct numerical simulation of turbulent flow. *Journal of Computational Physics 256* (2014), 1–16.

[6] Baidya-Roy, S., Pacala, S. W., and Walko, R. L. Can large scale wind farms affect local meteorology? *J. Geophys. Res. 109* (2004), D19101.

[7] Barthelmie, R., Pryor, S., Frandsen, S., Hansen, K., Schepers, J. G., Rados, K., Schlez, W., Neubert, A., Jensen, L. E., and Neckelmann, S. Quantifying the impact of wind turbine wakes on power output at offshore wind farms. *J. Atmos. Oceanic Technol. 27* (2010), 1302–1317.

[8] Barthelmie, R., Rathmann, O., Frandsen, S. T., Hansen, K., Politis, E., Prospathopoulos, J., Rados, K., Cabezón, D., Schlez, W., Phillips, J., Neubert, A., Schepers, J. G., and van der Pijl, S. P. Modelling and measurements of wakes in large wind farms. *J. Physics: Conference Series 75* (2007), 012049.

[9] Bastine, D., Witha, B., Wächter, M., and Peinke, J. POD analysis of a wind turbine wake in a turbulent atmospheric boundary layer. *J. Physics: Conference Series 524* (2014), 012153.

[10] Bewley, T. R., Moin, P., and Temam, R. DNS-based predictive control of turbulence: an optimal benchmark for feedback algorithms. *J. Fluid Mech. 447* (2001), 179–225.

[11] Blonigan, P. J., Gomez, S. A., and Wang, Q. Least squares shadowing for sensitivity analysis of turbulent fluid flows. In *Proceedings of 52nd Aerospace Sciences Meeting, AIAA SciTech* (2014), pp. 1–24.

[12] Borzi, A., and Schultz, V. *Computational optimization of systems governed by partial differential equations*. SIAM, Philadelphia, 2012.

[13] Bou-Zeid, E., Meneveau, C., and Parlange, M. B. A scale-dependent Lagrangian dynamic model for large eddy simulation of complex turbulent flows. *Physics of Fluids 17*, 025105 (2005).

[14] Burton, T., Sharpe, D., Jenkins, N., and Bossanyi, E. *Wind Energy Handbook*. John Wiley & Sons, 2001.

[15] Cal, R. B., Lebron, J. L., Castillo, L., Kang, H. S., and Meneveau, C. Experimental study of the horizontally averaged flow structure in a model wind-turbine array boundary layer. *J. Ren. and Sust. Energy 2* (2010), 013106.

[16] Calaf, M., Meneveau, C., and Meyers, J. Large eddy simulation study of fully developed wind-turbine array boundary layers. *Phys. Fluids 22* (2010), Art no 015110. DOI: 10.1063/1.3291077.

[17] Calaf, M., Parlange, M. B., and Meneveau, C. Large eddy simulation study of scalar transport in fully developed wind-turbine array boundary layers. *Physics of Fluids 23*, 126603 (2011).

[18] Canuto, C., Hussaini, M. Y., Quarteroni, A., and Zang, T. A. *Spectral Methods in Fluid Dynamics*. Springer, 1988.

[19] Canuto, C., Hussaini, M. Y., Quarteroni, A., and Zang, T. A. *Spectral Methods: Evolution to Complex Geometries and Application to Fluid Dynamics*. Springer, 2007.

[20] Chamorro, L. P., Arndt, R. E. A., and Sotiropoulos, F. Turbulent flow properties around a staggered wind farm. *Boundary-Layer Meteorology 141* (2011), 349–367.

[21] Chang, Y., and Collis, S. S. Active control of turbulent channel flows based on large eddy simulation. In *Proc. 1999 ASME/JSME Joint Fluids Engineering Conference* (1999), pp. FEDSM99–6929.

[22] Choi, H., Hinze, M., and Kunisch, K. Instantaneous control of backward-facing step flows. *Applied Numerical Mathematics 31* (1999), 133 – 158.

[23] Chowdhury, S., Zhang, J., Messac, A., and Castillo, L. Unrestricted wind farm layout optimization (UWFLO): Investigating key factors influencing the maximum power generation. *Renewable Energy 38* (2012), 16–30.

[24] Churchfield, M. J., Lee, S., Michalakes, J., and Moriarty., P. J. A numerical study of the effects of atmospheric and wake turbulence on wind turbine dynamics. *Journal of Turbulence 13*, 14 (2012), 1–32.

[25] Collis, S. S., Chang, Y., Kellogg, S., and Prabhu, R. D. Large eddy simulation and turbulence control. In *Proceedings of the 2000 AIAA Fluids Conference* (2000), pp. AIAA–2000–2564.

[26] Delport, S., Baelmans, M., and Meyers, J. Constrained optimization of turbulent mixing-layer evolution. *J. Turbul. 10*, 18 (2009), 1–26.

[27] Delport, S., Baelmans, M., and Meyers, J. Maximizing dissipation in a turbulent shear flow by optimal control of its initial state. *Phys. Fluids 25* (2011), 045105.

[28] EWEA. Wind energy facts. `http://www.ewea.org`.

[29] Fleming, P., Gebraad, P., Lee, S., Churchfield, M., Scholbrock, A., Michalakes, J., Johnson, K., and Moriarty, P. The sowfa super-controller: A high-fidelity tool for evaluating wind plant control approaches. *Proc. EWEA 2013, 4-7 February 2013, Vienna, Austria EWEA* (2013), 1–12.

[30] Fleming, P. A., Gebraad, P. M., Lee, S., van Wingerden, J.-W., Johnson, K., Churchfield, M., Michalakes, J., Spalart, P., and Moriarty, P. Evaluating techniques for redirecting turbine wakes using {SOWFA}. *Renewable Energy 70* (2014), 211–218.

[31] Fleming, P. A., Gebraad, P. M., Lee, S., van Wingerden, J.-W., Johnson, K., Churchfield, M., Michalakes, J., Spalart, P., and Moriarty, P. Simulation comparison of wake mitigation control strategies for a two-turbine case. *Wind Energy we.1810* (2014), 1–9.

[32] Frandsen, S. On the wind speed reduction in the center of large clusters of wind turbines. *J. Wind Eng Indust. Aerodyn. 39* (1992), 251–265.

[33] Frigo, M., and Johnson, S. G. The design and implementation of FFTW3. *Proceedings of the IEEE 93*, 2 (2005), 216–231. Special issue on "Program Generation, Optimization, and Platform Adaptation".

[34] Gebraad, P. M. O., Teeuwisse, F. W., van Wingerden, J. W., Fleming, P. A., Ruben, S. D., Marden, J. R., and Pao, L. Y. Wind plant power optimization through yaw control using a parametric model for wake effects-a cfd simulation study. *Wind Energy we. 1822* (2014), 1–20.

[35] Gebraad, P. M. O., and van Wingerden, J. W. Maximum power-point tracking control for wind farms. *Wind Energy 18* (2014), 429–447.

[36] Giles, M. B., and Pierce, N. A. An introduction to the adjoint approach to design. *Flow, Turbulence and Combustion 65* (2000), 393–415.

[37] Global Wind Report. Annual market update. Tech. rep., Global Wind Energy Council, 2013.

[38] Goit, J. P., and Meyers, J. Effect of Ekman layer on windfarm roughness and displacement height. In *Direct and large-eddy simulation IX* (2013), pp. 423–434.

[39] Goit, J. P., and Meyers, J. Optimal control of energy extraction in wind-farm boundary layers. *Journal of Fluid Mechanics 768* (2015), 5–50.

[40] Grady, S. A., Hussaini, M. Y., and Abdullah, M. M. Placement of wind turbines using genetic algorithms. *Renewable Energy 30* (2005), 259–270.

[41] Gunzburger, M. D. *Perspectives in Flow Control and Optimization*. SIAM, 2003.

[42] Hamilton, N., Kang, H. S., Meneveau, C., and Cal, R. B. Statistical analysis of kinetic energy entrainment in a model wind turbine array boundary layer. *J. Renewable Sustainable Energy 4* (2012), 063105.

[43] Hansen, A. D., Sørensen, P., Iov, F., and Blaabjerg, F. Centralised power control of wind farm with doubly fed induction generators. *Renewable Energy 31* (2006), 935–951.

[44] Hansen, K. S., Barthelmie, R. J., Jensen, L. E., and Sommer, A. The impact of turbulence intensity and atmospheric stability on power deficits due to wind trubine wakes at horns rev wind farm. *Wind Energy. 15* (2011), 183–196.

[45] Hansen, M. O. L. *Aerodynamics of Wind Turbines*, 2nd ed. Earthscan, 2008.

[46] Hinze, M., and Kunisch, K. Second order methods for optimal control of time-dependent fluid flow. *SIAM J. Control Optim. 40* (2001), 925–946.

[47] Horvat, T., Spudic, V., and Baotic, M. Quasi-stationary optimal control for wind farm with closely spaced turbines. In *MIPRO, 2012 Proceedings of the 35th International Convention* (2012), pp. 829–834.

[48] Ivanell, S., Sørensen, J. N., Mikkelsen, R., and Henningson, D. Analysis of numerically generated wake structures. *Wind Energy 12* (2009), 63–80.

[49] Jameson, A. Aerodynamic design via control theory. *J. Sci. Comput. 3* (1988), 233–260.

[50] Jensen, N. O. A note on wind generator interaction. Tech. Rep. Risø-M-2411, Risø National Laboratory, Roskilde, Denmark, 1983.

[51] Jiménez, A., Crespo, A., and Migoya, E. Application of a LES technique to characterize the wake defl ection of a wind turbine in yaw. *Wind Energy 13* (2010).

[52] Jimenez, A., Crespo, A., Migoya, E., and Garcia, J. Advances in large-eddy simulation of a wind turbine wake. *J. of Physics: Conference Series 75*, 012041 (2007).

[53] Johnson, K. E. Adaptive torque control of variable speed wind turbines. Tech. Rep. NREL/TP-500-36265, National Renewable Energy Laboratory, Cole Boulevard, Golden, Colorado, August 2004.

[54] Johnson, K. E., and Thomas, N. Wind farm control: addressing the aerodynamic interaction among wind turbines. In *American Control Conference, 2009. ACC '09.* (St. Louis, MO, June 2009), IEEE, pp. 2104–2109.

[55] Johnstone, R., and Coleman, G. N. The turbulent ekman boundary layer over an infinite wind-turbine array. *J. Wind Eng. Ind. Aerodyn. 100* (2012), 46–57.

[56] Jonkman, J., Butterfield, S., Musial, W., and Scott, G. Definition of a 5-mw reference wind turbine for offshore system development. Tech. Rep. NREL/TP-500-38060, National Renewable Energy Laboratory, Cole Boulevard, Golden, Colorado, February 2009.

[57] Kaminsky, F. C., Kirchhoff, R. H., and Sheu, L.-J. Optimal spacing of wind turbines in a wind energy power plant. *Solar Energy 39* (1987), 467–471.

[58] Kim, S., Alonso, J., and Jameson, A. A gradient accuracy study for the adjoint-based Navier-Stokes design method. *37th Aerospace Sciences Meeting and Exhibit, Reno, Nevada AIAA-99-0299* (1999), 1–23.

[59] Knudsen, T., Bak, T., and Svenstrup, M. Survey of wind farm control–power and fatigue optimization. *Wind Energy* (2014).

[60] Kusiak, A., and Song, Z. Design of wind farm layout for maximum wind energy capture. *Renewable Energy 35* (2010), 685–694.

[61] Larsen, J. W., Nielsen, S. R. K., and Krenk, S. Dynamic stall model for wind turbine airfoils. *Journal of Fluids and Structures 23* (2007), 959–982.

[62] Lebron, J., Castillo, L., and Meneveau, C. Experimental study of the kinetic energy budget in a wind turbine stream-tube. *Journal of Turbulence 13*, 43 (2012), 1–22.

[63] Lissaman, P. B. S. Energy effectiveness of arbitrary arrays of wind turbines. In *17th AIAA Aerospace Sciences Meeting* (New Orleans, Louisiana, January 1979), pp. AIAA 1979–114.

[64] Lu, H., and Porté-Agel, F. Large-eddy simulation of a very large wind farm in a stable atmospheric boundary layer. *Phys. Fluids 23* (2011), 065101.

[65] Luenberger, D. G. *Linear and Nonlinear Programming*, 2nd ed. Kluwer Academic Publishers, 2005.

[66] Marden, J. R., Ruben, S. D., and Pao, L. Y. A model-free approach to wind farm contro using game theoretic methods. In *IEEE Transactions on Control Systems Technology* (2013), vol. 21 (4), pp. 1207–1214.

[67] Markfort, C. D., Zhang, W., and Porté-Agel, F. Turbulent flow and scalar transport through and over aligned and staggered wind farms. *Journal of Turbulence 13*, 33 (2012), 1–36.

[68] Mason, P. J., and Thomson, T. J. Stochastic backscatter in large-eddy simulations of boundary layers. *Journal of Fluid Mechanics 242* (1992), 51–78.

[69] Meneveau, C. The top-down model of wind farm boundary layers and its applications. *Journal of Turbulence 13*, 7 (2012), 1–12.

[70] Meyers, J., and Meneveau, C. Large eddy simulations of large wind-turbine arrays in the atmospheric boundary layer. *48th AIAA Aerospace Sciences Meeting Including the New Horizons Forum and Aerospace Exposition, Orlando, Florida AIAA 2010-827* (2010), 1–10.

[71] Meyers, J., and Meneveau, C. Optimal turbine spacing in fully developed wind-farm boundary layers. *Wind Energy 15* (2012), 305–317.

[72] Meyers, J., and Meneveau, C. Flow visualization using momentum and energy transport tubes and applications to turbulent flow in wind farms. *Journal of Fluid Mechanics 715* (2013), 335–358.

[73] Meyers, J., and Sagaut, P. On the model coefficients for the standard and the variational multi-scale Smagorinsky model. *Journal of Fluid Mechanics 569* (2006), 287–319.

[74] Meyers, J., and Sagaut, P. Evaluation of smagorinsky variants in large-eddy simulations of wall-resolved plane channel flows. *Physics of Fluids 19*, 095105 (2007).

[75] Mikkelsen, R. *Actuator Disc Methods Applied to Wind Turbines*. PhD dissertation, Department of Mechanical Engineering, Technical University of Denmark, 2003.

[76] Moeng, C.-H. A large-eddy simulation model for the study of planetary boundary-layer turbulence. *J. Atmos. Sci. 41* (1984), 2052–2062.

[77] Newman, B. G. The spacing of wind turbines in large arrays. *Energy Conv. 16* (1976), 169–179.

[78] Newman, J., Lebron, J., Meneveau, C., and Castillo, L. Streamwise development of the wind turbine boundary layer over a model wind turbine array. *Physics of Fluids 25*, 085108 (2013).

[79] Nocedal, J., and Wright, S. J. *Numerical Optimization*, 2nd ed. Springer, 2006.

[80] Önder, A. *Active control of turbulent axisymmetric jets using zero-net-mass-flux actuation*. PhD dissertation, Department of Mechanical Engineering, KU Leuven, 2014.

[81] Pao, L. Y., and Johnson, K. E. A tutorial on the dynamics and control of wind turbines and wind farms. In *Proceedings of the 2009 American Control Conference* (Piscataway, NJ, USA, 2009), IEEE Press, pp. 2076–2089.

[82] Pironneau, O. On optimum design in fluid mechanics. *J. Fluid Mech. 64* (1974), 97–110.

[83] Porté-Agel, F., Wu, Y., and Chen, C. A numerical study of the effects ofwind direction on turbine wakes and power losses in a largewind farm. *Energies 6* (2013), 5297–5313.

[84] Press, W. H., Teukolsky, S. A., Vetterling, W. T., and Flannery, B. P. *Numerical Recipes in FORTRAN77: The art of scientific computing*. Cambridge University Press, 2nd edition, 1996.

[85] Rathmann, O., Frandsen, S., and Barthelmie, R. Wake modelling for intermediate and large wind farms. In *European Wind Energy Conference and Exhibition* (Milan, Italy, May 2007), p. BL3.199.

[86] Rawlings, J. B., and Mayne, D. Q. *Model Predictive Control: Theory and Design*. Nob Hill Publishing, 2008.

[87] Sanderse, B., van der Pijl, S. P., and Koren, B. Review of computational fluid dynamics for wind turbine wake aerodynamics. *Wind Energy 14* (2011), 799–819.

[88] Sarlak, H., Meneveau, C., and Sørensen, J. N. Role of subgrid-scale modeling in large eddy simulation of wind turbine wake interactions. *Renewable Energy 77* (2015), 386–399.

[89] Schumann, U. Subgrid scale model for finite difference simulations of turbulent flows in plane channels and annuli. *Journal of Computational Physics 18* (1975), 376–404.

[90] Smagorinsky, J. General circulation experiments with the primitive equations: I. The basic experiment. *Monthly Weather Review 91*, 3 (1963), 99–165.

[91] Soleimanzadeh, M., Wisniewski, R., and Johnson, K. A distributedoptimizationframeworkforwindfarms. *J. Wind Eng. Ind. Aerodyn. 123* (2013), 88–98.

[92] Soleimanzadeh, M., Wisniewski, R., and Kanev, S. An optimization framework for load and power distribution in wind farms. *J. Wind Eng. Ind. Aerodyn. 107-108* (2012), 256–262.

[93] Spruce, C. J. *Simulation and Control of Windfarms*. PhD dissertation, University of Oxford, Department of Engineering Science, 1993.

[94] Steinbuch, M., de Boer, W. W., Bosgra, O. H., Peters, S., and Ploeg, J. Optimal control of wind power plants. *J. Wind Eng Indust. Aerodyn. 27* (1988), 237–246.

[95] Stevens, R. J. Dependence of optimal wind-turbine spacing on windfarm length. *Wind Energy Submitted* (2015), 1–9.

[96] Stevens, R. J., Gayme, D. F., and Meneveau, C. Large eddy simulation studies of the effects of alignment and wind farm length. *J. Renewable Sustainable Energy 6* (2014), 023105.

[97] Stevens, R. J., Graham, J., and Meneveau, C. A concurrent precursor inflow method for large eddy simulations and applications to finite length wind farms. *Renewable Energy 68* (2014), 46–50.

[98] Stevens, R. J., and Meneveau, C. Temporal structure of aggregate power fluctuations in large-eddy simulations of extended wind-farms. *J. Renewable Sustainable Energy 6* (2014), 043102.

[99] Stull, R. B. *An Introduction to Boundary Layer Meteorology*. Kluwer, Dordrecht, 1988.

[100] Tchakoua, P., Wemkeue, R., Ouhrouche, M., Slaoui-Hasnaoui, F., Tameghe, T. A., and Ekemb, G. Wind turbine condition monitoring: State-of-the-art review, new trends, and future challenges. *Energies 7* (2014), 2595–2630.

[101] Tennekes, H., and Lumley, J. L. *A first Course in Turbulence*. The MIT Press, 1972.

[102] Tröltzsch, F. *Optimal Control of Partial Differential Equations: Theory, Methods, and Applications*. American Mathematical Soc., 2010.

[103] van Wingerden, J.-W. Reconfigurable floating wind turbines. VENI project #11930, 2011.

[104] VerHulst, C., and Meneveau, C. Large eddy simulation study of the kinetic energy entrainment by energetic turbulent flow structures in large wind farms. *Physics of Fluids 26* (2014), 025113.

[105] Verstappen, R. W. C. P., and Veldman, A. E. P. Symmetry-preserving discretization of turbulent flow. *Journal of Computational Physics 187* (2003), 343–368.

[106] Wang, C., and Prinn, R. G. Potential climatic impacts and reliability of very large-scale wind farms. *JAtmos. Chem. Phys. 10* (2010), 2053–2061.

[107] Wei, M., and Freund, J. B. A noise-controlled free shear flow. *Journal of Fluid Mechanics 546* (2006), 123–152.

[108] Wu, Y.-T., and Porté-Agel, F. Large-eddy simulation of wind-turbine wakes: evaluation of turbine parametrisations. *Boundary-Layer Meteorol. 138* (2011), 345–366.

[109] Wu, Y.-T., and Porté-Agel, F. Simulation of turbulent flow inside and above wind farms: Model validation and layout effects. *Boundary-Layer Meteorology 146*, 2 (2013), 181–205.

[110] Wu, Y.-T., and Porté-Agel, F. Modeling turbine wakes and power losses within a wind farm using les: An application to the Horns Rev offshore wind farm. *Renewable Energy 75* (2015), 945–955.

[111] Yang, D., Meneveau, C., and Shen, L. Effect of swells on offshore wind energy harvesting-a large-eddy simulation study. *Renewable Energy 70* (2014), 11–23.

[112] Yang, D., Meneveau, C., and Shen, L. Large-eddy simulation of off-shore wind farm. *Renewable Energy 26*, 025101 (2014).

[113] Yang, X., Kang, S., and Sotiropoulos, F. Computational study and modeling of turbine spacing effects in infinite aligned wind farms. *Physics of Fluids 24*, 115107 (2012).

[114] Yang, Z., Li, Y., and Seem, Y. Maximizing wind farm energy capture via nested-loop extremum seeking control. In *Proceedings of the ASME Dynamic Systems and Control Conference* (2013), Palo Alto, California, USA.

[115] Zilitinkevich, S. S. Velocity profiles, the resistance law and the dissipation rate of mean flow kinetic energy in a neutrally and stably stratified planetary boundary layer. *Boundary-Layer Meteorol. 46*, 4 (1989), 367–387.

[116] Zilitinkevich, S. S., and Esau, I. N. On integral measures of the neutral barotropic planetary boundary layer. *Boundary-Layer Meteorol. 104* (2002), 371–379.

Curriculum vitae

Jay Prakash Goit was born in Khirauna, Nepal in 1983. He got his Bachelor's degree in Mechanical and Aerospcace Engineering in 2009 from Tohoku University, Japan. His Bachelor's thesis was titled 'Design and performance test of a multi-fan gust wind tunnel'. He received his Master's degree in 2010 from the Department of Mechanical Systems and Design at Tohoku University. The title of his Master's dissertation was 'Prediction of transition point by estimating flow instability with nonlinear effect'. During his Master's degree, Jay also worked as an intern at Kubota Corporation, Japan in August 2009. The internship project involved the endurance test of a large rain water pump.

In October 2010, he started his PhD at the Division of Applied Mechanics and Energy Conversion (TME) of the Mechanical Engineering Department at KU Leuven. The PhD program was supervised by Prof.dr.ir. Johan Meyers. The research was partially supported by the European Research Council (FP7-Ideas, grant no. 306471) and the Flemish Science Foundation (FWO, grant no. G.0376.12).

List of publications

International peer reviewed journal articles

- Goit, J. P., Meyers, J. (2015). Optimal control of energy extraction in wind-farm boundary layers.*Journal of Fluid Mechanics*, 768, 5-50.

Papers at international scientific conferences and symposia

- Goit, J. P., Meyers, J. (2014). Analysis of turbulent flow properties and energy fluxes in optimally controlled wind-farm boundary layers. *Journal of Physics: Conference Series*, 524, 012178.
- Goit, J. P., Meyers, J. (2014). Optimal control of wind farm power extraction in large eddy simulations. *32nd ASME Wind Energy Symposium, AIAA SciTech*, DOI: 10.2514/6.2014-0709.
- Goit, J. P., Meyers, J. (2013). Effect of Ekman layer on windfarm roughness and displacement height. In *Proceedings of Direct and large-eddy simulation IX*, Dresden, Germany, 423-434.
- Sternberg-Kaletta, J., Goit, J. P., Gros, S., Meyers, J., Diehl, M. (2012). Robust and stable periodic flight of power generating kite systems in turbulent wind flow field. In *Proceedings of the 15th IFAC workshop on Control Applications of Optimization*, 15, 140-145.

Abstracts, presented at international scientific conferences and symposia

- Meyers, J., Goit, J. P. (2014). Simulation and optimal control of wind-farm boundary layers. *European Geosciences Union General Assembly 2014.* Vienna, Austria.
- Meyers, J., Goit, J. P., Munters, W. (2014). Optimal control of energy extraction in LES of large wind farms. *67th Annual meeting of the APS Division of Fluid Dynamics.* San Francisco, CA, USA.
- Meyers, J., Goit, J. P. (2013). Power Optimization of Wind Farms in Large Eddy Simulations. *66th Annual meeting of the APS Division of Fluid Dynamics.* Pittsburg, PA, USA.
- Goit, J., Robeers, H., Coddé, J., Meyers, J. (2011). Effect of the Ekman layer on the effective roughness length of large scale wind farms. *64th Annual meeting of the APS Division of Fluid Dynamics.* Baltimore, MD, USA.

FACULTY OF ENGINEERING SCIENCE
DEPARTMENT OF MECHANICAL ENGINEERING
DIVISION OF APPLIED MECHANICS AND ENERGY CONVERSION
TURBULENT FLOW SIMULATION & OPTIMIZATION
Celestijnenlaan 300 box 2420
B-3001 Heverlee
jay.goit@kuleuven.be
https://www.mech.kuleuven.be/en/tme/research/tfso